Thermoactive Foundations for Sustainable Buildings

John Scott McCartney
Moncef Krarti
Byung Chang Kwag
Abdelmalek Bouazza
Rao Martand Singh
Mohammed Faizal

Co-published by Momentum Press, LLC , 222 E. 46th Street, #203, New York, NY 10017, USA (www.momentumpress.net)

A catalog record is available from the Library of Congress.

Print ISBN: 978-0-7918-6105-9
ASME Order No. 861059
Electronic ISBN: 978-1-60650-886-2

Series Editors' Preface

Technologies for Sustainable Life (TSL) – Concise Monograph Series
ASME's Technologies for Sustainable Life (TSL) is a series of concise and timely monographs exploring the interface between engineering and the environmental sustainability agenda. The series adopts a broad base examining fundamental principles and paradigms before a contextual exploration of ecosystems and resources, sustainable manufacturing, energy technology, environmental pollution and finally aspects of environmental governance.

Each monograph is written by leading experts in their field and examines the relationship and contributions of engineering to the topic of study. As a series, TSL addresses a long-awaited niche in engineering publishing, providing in-depth discussions of environmental significance set within a technology, economic and policy context.

Guest Editor Preface

This monograph is part of ASME efforts to promote exchange of innovative ideas, leading edge concepts, new technologies, ongoing research and development related to the theme of sustainable buildings. Specifically, these efforts have been initiated by the ASME Research Committee on Integrated and Sustainable Building Equipment and Systems (ISBES). It is hoped that this monograph would document the current of state-of-art in thermo-active foundations suitable for efficiently and sustainably heat and cooling buildings. Indeed, Thermo-active foundations (TAFs), also referred to as thermal or energy piles, offer innovative and sustainable alternatives to ground-source heat pumps as well as other conventional heating, ventilating, and air conditioning (HVAC) systems to heat and cool commercial as well as residential buildings in several regions in the world. TAFs have a dual function since they are installed within elements that are already needed for statical, structural, and geotechnical purposes. Reported studies have shown that TAFs can save up to 55% of energy used to heat and cool both residential and commercial buildings compared to conventional HVAC systems. These systems have been reported to be more energy efficient than geothermal borehole ground-source heat pumps since concrete has higher thermal conductivity than most soil types. In addition, TAFs do not require any land availability which is one of the main challenges for conventional geothermal borehole heat pumps especially those using horizontal heat exchange loops.

The main objective of the current monograph is to present the current advances in designing and operating TAFs as well as the latest knowledge about their structural and thermal performance. Three peer-reviewed chapters written by research active experts in geothermal systems have been selected and included in the monograph to present three different aspects of TAFs including:

(i) The current understanding of soil-structure interaction effects that can occur due to their thermal expansion and contraction during heating and cooling cycles (Chapter 1).
(ii) The latest thermal models developed to assess the performance of TAFs as heating and cooling systems for both commercial and residential buildings (Chapter 2).

(iii) The results of monitoring analyses of full scale TAFs to evaluate both their structural and thermal performance over several years (Chapter 3).

Specifically, the first chapter starts with an overview of the current models to evaluate thermo-mechanical stress profiles in TAFs, along with the theoretical relationships between axial stress, axial strain, side shear stress, and axial displacement. Then, the first chapter presents relevant design criteria for the axial stress and displacement as well as thermo-mechanical load transfer analyses that can be used to predict the behavior of TAFs. Finally, the first chapter presents a comparative analysis of experimental results from two full-scale, instrumented TAFs in different soil layers. The results presented in this chapter indicate that TAFs can be designed to meet safety requirements in terms of structural criteria for both foundations and the soil strata where drilled shaft foundations are typically employed.

In the second chapter, an overview of thermal analysis of TAFs is presented including integration approaches of TAF models into detailed whole-building energy simulation tools. In particular, the analyses presented in the chapter evaluate the impact of several design and operating TAF parameters on both building heating and cooling energy end-uses. Specifically, the thermal interactions between TAFs and building thermal loads are discussed and quantified. Moreover, the energy efficiency and cost-effectiveness of TAF systems is compared against conventional air conditioning systems for both commercial and residential buildings. In particular, the results of the thermal analyses show that TAFs can be more cost-effective than ground source heat pumps (GSHPs) due to lower installation costs and comparable energy performance.

The third chapter presents experimental results obtained from two studies conducted on full scale TAFs installed in a university at Melbourne, Australia. The first study evaluates the thermal and thermo-mechanical behavior of a single TAF, installed in December 2010. The second study considers two TAF systems recently installed as part of a foundation system of a multi-story residential building. The measured results for both studies are summarized in this chapter with some discussion of the main findings and observations. In particular, the experimental data for the first study indicate showed that TAFs do not exhibit any losses in foundation pile shaft capacity after full heating and cooling

cycles. Moreover, initial measurements from the second study indicate that concrete was initially in tension due to the cement hydration process but reversed to compressive strains once it cooled down and its temperature was in equilibrium with the surrounding soil.

In summary, the monograph collects the latest multi-disciplinary advances in modeling, designing, and monitoring TAFs. Ultimately, it is hoped that this monograph would provide a comprehensive reference for both researchers and professionals interested in structural and thermal performance of TAFs and their applications in developing integrated and sustainable equipment and systems for the built environment.

Moncef Krarti, Ph.D., P.E., LEED-PE, ASME Fellow
Guest Editor

Table of Contents

Abstract

This monograph documents the current of state-of-art in Thermo-Active Foundations (TAFs) suitable for efficiently and sustainably heat and cooling buildings. TAFs, also referred to as thermal or energy piles, offer innovative and sustainable alternatives to ground-source heat pumps as well as other conventional heating, ventilating, and air conditioning (HVAC) systems to heat and cool commercial as well as residential buildings in several regions in the world. In summary, this monograph collects the latest multi-disciplinary advances in modeling, designing, and monitoring TAFs. Ultimately, it is hoped that this monograph will provide a comprehensive reference for both researchers and professionals interested in structural and thermal performance of TAFs and their applications in developing integrated and sustainable equipment and systems for the built environment.

1. Structural performance of thermo-active foundations

John S. McCartney, Ph.D., P.E., University of California San Diego

Abstract: This chapter focuses on the current understanding of soil-structure interaction effects on thermo-active foundations that occur due to their thermal expansion and contraction during heating and cooling, respectively. The first section of the chapter presents hypothetical representations of thermo-mechanical stress profiles in thermo-active foundations, along with the theoretical relationships between axial stress, axial strain, side shear stress, and axial displacement. The second section of the chapter presents relevant design criteria for the axial stress and displacement in thermo-active foundations. The third section of the chapter presents the details of thermo-mechanical load transfer analyses that can be used to predict the behavior of thermo-active foundations. Finally, the fourth section of the chapter presents a comparison of experimental results from two full-scale, instrumented thermo-active foundations in different soil layers. Despite the importance of considering the role of thermo-mechanical soil-structure interaction, the evidence presented in this chapter indicates that thermo-active foundations will provide a safe response in terms of both structural and architectural criteria in the soil strata where drilled shaft foundations are typically employed.

1.1 Introduction

Heating and cooling of buildings comprises nearly 50% of the total building energy usage in the United States (Energy Information Administration 2008). Ground-source heat exchange (GSHE) systems are an approach to reduce the energy demand of heating and cooling systems compared to conventional air-source heat pump systems. The most common GSHE system involves the use of a closed loop heat exchanger to transfer heat between the subsurface soil or rock and an overlying structure, taking advantage of the relatively constant natural ground temperature below the depth of seasonal variation (Brandl 2006). The subsurface below a depth of 3–4 m generally has a relatively constant temperature approximately equal to the mean annual air temperature

at a given location, which contributes to making the efficiency of a GSHE system higher than that of an air-source heat exchange system (Kavanaugh et al. 1997).

Although conventional ground-source heat exchange (GSHE) systems have been used for many years, the additional cost of drilling deep boreholes for the sole purpose of exchanging heat with the ground has rendered this technology cost-prohibitive in some situations (Hughes 2008). Thermo-active foundations, which involve the incorporation of closed-loop geothermal heat exchangers into drilled shaft foundations, are an alternative to reduce installation costs by taking advantage of construction activities that are already planned (Brandl 2006; Adam and Markiewicz 2009; McCartney 2011; Olgun and McCartney 2014). Similar to conventional GSHE systems, a heat exchange design is required for thermo-active foundations to understand the amount of heat that can be exchanged with the subsurface for a given foundation geometry and spacing (Abdelaziz et al. 2011; Loveridge and Powrie 2012, 2104; Loveridge et al. 2015). Different from conventional GSHE systems, geotechnical design is also required to consider the complex interaction between temperature changes and induced stresses and strains in the foundation. Specifically, expansion or contraction of the foundation during heating or cooling may lead to changes in side shear resistance (and ultimate foundation capacity) or mechanical distress in the concrete, depending on the characteristics of the subsurface. This chapter presents the basic concepts needed to understand, design for, and predict soil-structure interaction phenomena in thermo-active foundations, along with examples of instrumentation data from full-scale thermo-active foundations that demonstrate the range of observed soil-structure interaction behavior.

1.2 Thermo-elastic soil-structure interaction

As a deep foundation is loaded mechanically (i.e., during application of the building dead and live loads), the axial stress is expected to be highest at the foundation head and decrease with depth as side shear resistance is mobilized at the soil-foundation interface. The axial stress will decrease to zero if the mobilized side shear resistance is sufficient to support the building load; if not, it will decrease to a non-zero value at the foundation tip. The axial stress at the foundation tip must be less than the end bearing resistance of the material underlying the toe of the

foundation. Methods to estimate the ultimate side shear resistance and end bearing resistance of foundations is well described in most foundation textbooks (e.g., Coduto 2000). Because the axial stresses within the foundation depend on the mobilization of side shear stresses and end bearing stresses in the surrounding soil, the approach to estimate the distribution in axial stress and strain within the foundation is an example of soil-structure interaction (Coyle and Reese 1966). Regardless of the mobilized resistances in the soil, the axial strains in the reinforced concrete during mechanical loading correspond directly to axial stresses in the concrete through Hooke's law:

$$\sigma_M = \varepsilon_m E \tag{1}$$

where σ_m is the mechanical axial strain, ε_m is the mechanical axial strain, and E is the Young's modulus of the reinforced concrete. For the concrete mix design typically used in drilled shaft foundations (high slump), E is approximately equal to 30 GPa.

More complex soil-structure interaction phenomena occur in thermo-active foundations as axial strains due to the phenomenon of thermo-elastic expansion, where thermal strains ε_T occur during a change in temperature proportional to a coefficient of thermal expansion. Different from a free element of reinforced concrete above the ground surface, the thermal expansion and contraction of a thermo-active foundation in the ground will likely be less than is theoretically possible due to soil-structure interaction. The upper limit on the thermal axial strain ε_T in a thermo-active foundation is referred to as the free expansion (i.e., unrestrained) thermal axial strain $\varepsilon_{T,\text{free}}$, defined as follows:

$$\varepsilon_{T,\text{free}} = \alpha_c \Delta T \tag{2}$$

where α_c is the coefficient of linear thermal expansion of the reinforced concrete foundation and ΔT is the change in temperature. Following geotechnical engineering conventions, the thermal axial strain is defined as positive in compression. Accordingly, α_c is defined as negative because structural elements expand during heating (i.e., positive ΔT).

The coefficient of thermal expansion of Portland cement concrete ranges from –8 to –12 με/°C, and varies with differences in concrete mix design (water-cement ratio, fine to coarse aggregate ratio) and the mineralogy of the aggregates (limestone, quartz, etc.) (PCCP 2011). The

coefficient of thermal expansion of steel used as reinforcement in drilled shafts is approximately –12 με/°C. Although the thermal strains in concrete and steel are relatively similar, indicating that compatible strains will likely occur during heating, the composite coefficient of thermal expansion of thermo-active foundations has been observed to be greater than the values of the constituents. Bourne-Webb et al. (2009), Stewart and McCartney (2013), and Goode et al. (2014) quantified the thermal strain in reinforced concrete thermo-active foundations, and found that the coefficient of thermal expansion α_T of reinforced concrete containing plastic heat exchangers may range from –8 to –16 με/°C. McCartney and Murphy (2015) and Murphy et al. (2015) found that a coefficient of thermal expansion of –13 με/°C provided a good fit for the interpretation of thermal axial strains measured in thermo-active foundations. The wider range of thermal expansion values in thermo-active foundations than in Portland cement concrete may be partially due to the inclusion of the plastic heat exchange pipes, which have a much larger coefficient of thermal expansion of approximately –120 με/°C.

The value of ΔT to use in Equation 1 may be challenging to define. During geothermal heat pump operation, thermo-active foundations typically have a relatively constant temperature with depth, although proximity to the ground surface, ground water table, or soil or rock layers with high thermal conductivity can affect the temperature distribution (Wang et al. 2014; Murphy and McCartney 2015; Murphy et al. 2015). Accordingly, the value of $\varepsilon_{T,\text{free}}$ calculated with Equation 1 should be assessed as a function of depth when evaluating the behavior of thermo-active foundations instead of using an average value of ΔT. Examples of the temperature distributions in real thermo-active foundations will be presented later in the chapter.

As a thermo-active foundation is heated or cooled, the reinforced concrete will tend to expand or contract axially about a point referred to as the "null point" (Knellwolf et al. 2011). The null point is the point of zero axial displacement during heating or cooling, and its location depends on the stiffness of the end boundaries imposed by the overlying superstructure and the material beneath the toe, as well as the distribution of mobilized side shear resistance (Bourne-Webb et al. 2009; Amatya et al. 2012). It is also possible that the foundation may expand radially during heating (Laloui et al. 2006; Wang et al. 2014), which may result in a net increase in ultimate side shear resistance (McCartney and

Rosenberg 2011; Ouyang et al. 2011). This depends on the stiffness of the surrounding soil compared to the soil (Olgun et al. 2014b) as well as the differential changes in temperature of the foundation and soil during the transient heating and cooling processes.

For the case that a thermo-active foundation is restrained from moving such that the actual thermal axial strain ε_T at a given depth is less than the value of $\varepsilon_{T,\text{free}}$ calculated by Equation 1, the thermal axial stresses σ_T at a given depth can be calculated as follows:

$$\sigma_T = E(\varepsilon_T - \alpha_c \Delta T) \tag{3}$$

where E is the Young's modulus of reinforced concrete. In thermo-active foundations, soil-structure interaction will restrict the movement of the foundation during heating. The side shear resistance, end bearing, and building restraint will influence the distribution in thermally induced stresses and strains (Mimouni and Laloui 2013).

If the distribution in thermal axial stress is calculated in a thermo-active foundation, the mobilized side shear stress can be calculated at different heights in the soil layer, as follows:

$$f_{s,\text{mob},j} = \frac{(\sigma_{T,j} - \sigma_{T,j-1})D}{4\Delta l} \tag{4}$$

where D is the shaft diameter and Δl is the distance between the calculated values of thermal axial stress. The sign convention for the mobilized side shear stress implies that positive side shear stresses are upward (in the same direction as those mobilized during mechanical loading), while negative side shear stresses are downward (in the opposite direction as those mobilized during mechanical loading).

If the thermal axial strain is measured in a thermo-active foundation, they can be used to estimate the relative thermal axial displacements in the foundation. Estimation of the thermal axial displacements is most relevant in the case of end-bearing foundations, whose toe is not expected to settle significantly during mechanical loading or heating/cooling. The relative thermal axial displacements to the bottom of the foundations could be calculated by integrating the thermal axial strain profiles, as follows:

$$\delta_{T,i} = \delta_{T,i-1} + \frac{1}{2}(\varepsilon_{T,i-1} + \varepsilon_{T,i})\Delta l \tag{5}$$

where $\delta_{T,i}$ is the thermal axial displacement at the midpoint between gages, $\varepsilon_{T,i}$ is the thermal axial strain at the location of gage *i*. Because the displacements at the heat and toe are typically not know, the displacements are relative to the movement of the head and toe.

A set of schematics showing the relationships between the thermal axial stress, relative displacement, thermal axial stress, and mobilized side shear stress in an end-bearing thermo-active foundation are shown in Figure 1-1. In this case the null point is positioned at the toe of the foundation due to the rigid bottom boundary. In most real thermo-active foundations with end-bearing conditions, the null point is slightly above to base due to difficulties in cleaning out the excavation before concrete placement (Murphy et al. 2015).

Additional simplified schematics of thermo-mechanical soil-structure interaction relationships are shown in Bourne-Webb et al. (2009) for floating foundations that have negligible end-bearing. In floating foundations, the null point is assumed to be located at or above the middle of the foundation. It is rare to find a truly floating thermo-active foundation in the field, so a foundation that has a lower end bearing resistance than side shear resistance is typically referred to as a semi-floating foundation. The restraints and the head and toe of the building will also have important effects on the soil-structure interaction in semi-floating thermo-active foundations, as shown schematically for different examples in Figure 1-2 (after Amatya et al. 2012). The head resistance

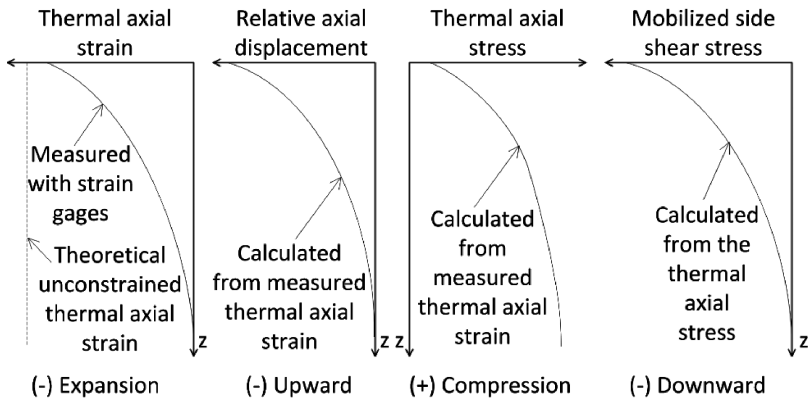

Figure 1-1 Conceptual relationships between axial strain, relative axial displacement, axial stress, and mobilized side shear stress in an end-bearing thermo-active foundation.

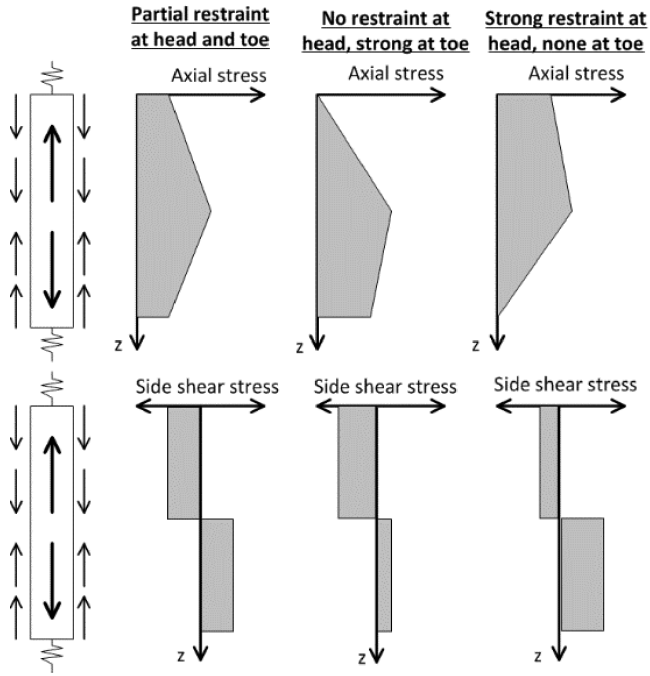

Figure 1-2 Conceptual profiles of thermo-mechanical axial stress and mobilized side shear resistance in thermo-active foundations with different head and toe restraint conditions.

is an important parameter in thermo-active foundations (Burlon et al. 2013), and depends on the structural characteristics of the overlying building (i.e., the stiffness of a grade beam or mat foundation connected to the head of the foundation). The schematics in Figure 1-2 also show how the null point may move upward or downward depending on the restraints provided at the head or toe of the foundation. The lower half of Figure 1-2 shows the mobilized side shear resistance for each scenario, which is assumed to have a constant magnitude with depth and a direction opposite to that of the thermal axial strain. During heating or cooling of a thermo-active foundation, it is possible that the side shear resistance may undergo either further loading or unloading depending. Specifically, during mechanical loading, a positive (upward) mobilized side shear stress is typically induced at the soil-foundation interface. During heating, a point that is above the null point will move upward, leading to a decrease in the mobilized side shear stress. A point below

the null point will move further downward, leading to an increase in the mobilized side shear stress.

Soil-structure interaction mechanisms of thermo-active foundations have been studied in simplified soil profiles in centrifuge-scale tests (McCartney and Rosenberg 2011; Stewart and McCartney 2013; Goode et al. 2014) and in laboratory-scale tests (Wang et al. 2012; Kramer and Basu 2014). These studies permit careful control of the soil layer and a good understanding of the restraints on the head and toe of the thermo-active foundation. However, evaluation of full-scale foundations imposes a set of real boundary conditions and soil strata. Several full-scale thermo-active foundations have been evaluated to study the thermo-mechanical stresses and strains during mechanical loading, heating, and cooling (Laloui et al. 2006; Bourne-Webb et al. 2009; Amatya et al. 2012; McCartney and Murphy 2012; Akrouch et al. 2014; Sutman et al. 2014; Wang et al. 2014; Murphy and McCartney 2015; Murphy et al. 2015). Although typical profiles of thermal axial stress, strain and displacement will be shown later in this chapter, it is important to mention the maximum values of thermal axial stress and displacement observed in these field studies when considering the different design criteria that should be set for the structural response of thermo-active foundations. The thermal axial stress observed in these studies during typical changes in temperature associated with heat pump operation (1 to 35 °C) ranged from –1 to 13.2 MPa and the thermal axial displacement of the foundation head ranged from –6.1 mm upward to +4.0 downward. These values should be superimposed atop the axial stresses and displacements corresponding to application of building dead and live loads before evaluating the performance of the thermo-active foundation with respect to design criteria.

1.3 Design criteria

Historically, the design of thermo-active foundations from a thermo-mechanical perspective relied on empirical and conservative approaches to account for additional axial stresses induced during heating and cooling. An improved quantitative approach to consider the stress, strains, and displacement in thermo-active foundations is the use of thermo-mechanical load-transfer analyses (Knellwolf et al. 2011). The software program Thermo-Pile® is available to perform this type of analysis as

part of a design (Peron et al. 2012). Limits on the stresses and displacements are described in the design standard for thermo-active foundations developed by the GSHP Association (2012).

As mentioned the thermal axial stress will be superimposed atop the mechanical axial stresses in the thermo-active foundation. The first design criteria is that the total thermo-mechanical axial stresses must be less than the compressive and tensile strength of the reinforced concrete. The compressive strength of concrete is typically 20–40 MPa, while the tensile strength is lower, approximately 2–5 MPa. The strength values for the concrete used in drilled shafts is at the lower range of this spectrum as it is designed to have a low slump to flow around the reinforcing cage in the excavated hole. This implies a lower amount of coarse aggregates, which leads to a lower strength. In regards to limits on the compressive stress, the highest thermo-mechanical stress in an experimental thermo-active foundation observed was within 60% of the compressive strength, and no negative effects were observed. In regards to limits on the tensile stress, it is possible for tensile thermo-mechanical stresses to occur at the toe of a lightly-loaded thermo-active foundation (Bourne-Webb et al. 2009). In this case, it is recommended that a full-length reinforcing cage be used in the design, as the inclusion of reinforcing steel increases the tensile strength of concrete significantly above the tensile thermo-mechanical stresses observed in the literature.

A more significant risk of integrating thermo-active foundations into a building is the possibility for differential movements as asymmetric thermal expansion or contraction could lead to the generation of bending moments and differential movement. Should heat exchange loops fail or clog in a given foundation, the foundation will cease to change in temperature. Significant differential expansion or contraction could occur should the heat exchange loops in a particular foundation fail next to a fully-functional foundation (Laloui et al. 2006). Boënnec (2009) indicates that the current design practice in Europe is to assume that 10% of the heat exchange tubes can be expected to fail during the lifetime of a foundation, although this has not been fully justified. Differential displacements may also occur near the outer boundary of the building, where foundation temperatures those inside of a group of foundations. These effects can be considered by limiting the range of temperature fluctuations, and possibly by changing reinforcement patterns in different foundations.

Displacement limits for thermo-active foundations can be defined by evaluating the angular distortions between columns and using criteria such as those defined by Skempton and MacDonald (1956) and Bjerrum (1963) (Table 1-1). The angular distortion in these studies is defined as the differential settlement between two foundations divided by the horizontal spacing between the two foundations. In all studies reported to date, the relatively small axial displacements of the thermo-active foundation (less than 6.1 mm) have led to angular distortions less than 1/5000. These values are not expected to cause architectural damage for most buildings.

There is some risk that a thermo-active foundation could have an effect on a sensitive soil layer. Accordingly, even though the observed values of stresses and displacement in thermo-active foundations mentioned in the previous section satisfy most structural design criteria, it is possible that new challenges will as thermo-active foundations are applied in a wider set of soil conditions. Specifically, most of the applications of thermo-active foundations in the field have been in relatively stiff soil or rock layers with end-bearing or semi-floating conditions.

In addition to the structural concerns on limiting the stress and displacement in thermo-active foundations, practical issues such as matching the number, depth, and spacing of ground loops with the required number, depth, and spacing of deep foundations must also be considered in the design of thermo-active foundation systems. If more ground

Table 1-1 Criteria for tolerable angular distortions (Bjerrum 1963).

Structure type	Tolerable angular distortion
Circular steel tank with fixed top	1/125
Circular steel tank with floating top	1/500 to 1/333
Tracks for overhead cranes	1/333
Steel frame warehouses	1/167 to 1/125
Structures with flexible finishes	1/500 to 1/333
Tall structures	1/500
Heavy multistory structures on a rigid mat foundation	1/667
Structures with brittle architectural finishes	1/1000 to 1/500

loops than deep foundations are required, then a backup conventional heating/cooling system or an auxiliary set of conventional GSHP heat exchangers outside of the building footprint would be needed. McCartney et al. (2010a) found that the thermal and structural requirements of a typical building can be attained with the same number of foundations, assuming AASHTO LRFD foundation resistance factors are used in foundation structural design.

1.4 Thermo-mechanical load transfer analysis

1.4.1 Assumptions and basic aspects of the model

An axial load transfer (T-z) analysis can be used to predict the axial deformation of a thermo-active foundation subject to mechanical and thermal loading. The traditional load transfer (T-z) analysis method developed by Coyle and Reese (1966) is capable of predicting the settlement and axial stress distributions in deep foundations subject to mechanical loading. Load transfer analyses can also be used to predict the load-settlement curve of a foundation. This approach has been extended to consider the thermo-elastic deformation of the foundation in several studies (Knellwolf et al. 2011; Ouyang et al. 2012; Plaseied 2012). These methods involve discretizing the foundation into several elements, then ensuring that each element has compatible strains and is in equilibrium with the surrounding soil layers. These axial load transfer analyses are based on the following assumptions:

- The properties of the foundation such as the Young's modulus (E) and coefficient of thermal expansion (α_T) remain constant along the foundation.
- Downward and upward movements are taken as positive and negative respectively. Compressional stresses are taken to be positive. Expansion strains are assumed to be negative.
- Foundation expands and contracts about a point referred to as the null point when it is heated or cooled (Bourne-Webb et al. 2009). The location of the null point depends on the upper and lower axial boundary conditions and side shear distribution.
- Depending on the particular details of the soil profile, the ultimate side shear resistance can be assumed to be constant with depth in a soil layer or it can be assumed to increase linearly with depth in a soil profile.

A typical foundation element being loaded mechanically is shown in Figure 1-3. The following notations are used in the T-z analysis:

- Q is used to represent axial force acting on an element within the foundation, or at the foundation head or base.
- The letter ρ stands for the relative displacement between the foundation and soil.
- K_f, K_s, and K_{base} are the stiffness values of the foundation spring, side shear spring and base spring spring, respectively.
- The indices "b", "t" and "s" represent the bottom, top and side of an element.
- The indices M and T represent mechanical and thermal loading, respectively.
- The index "*i*" represents the element number within the foundation.
- The variable "*l*" represents the length of each element along the foundation.

The behavior of each foundation element can be represented by a spring with stiffness of K_i. The spring stiffness K_i is defined by the following equation:

$$K_i = \frac{A_i E_i}{L_i} \tag{6}$$

where A_i is the cross section area of element *i*, E_i is the Young's modulus of the reinforced concrete in element *i*, and L_i is element length.

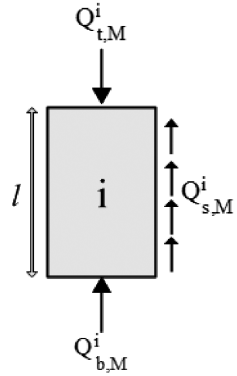

Figure 1-3 Typical element *i* with variables for mechanical loading.

A discretized thermo-active foundation is shown in Figure 1-4. Each element along the length of the foundation is connected to the soil with a spring that has a stiffness K_s that is represented with a nonlinear stress-displacement curve. Further, the element at the toe of the foundation is resting atop a spring with stiffness K_b that represents the end-bearing resistance of the underlying strata. In the analysis of Coyle and Reese (1966), a mechanical load is applied to the head of the foundation, and the stresses and displacements along the length of the foundation are calculated. The schematic in Figure 1-4 is slightly different from this case, as it shows the position of the null point at some location between the head and toe of the foundation, and also includes a spring at the head of the foundation having stiffness K_h that represents the stiffness of the overlying structure.

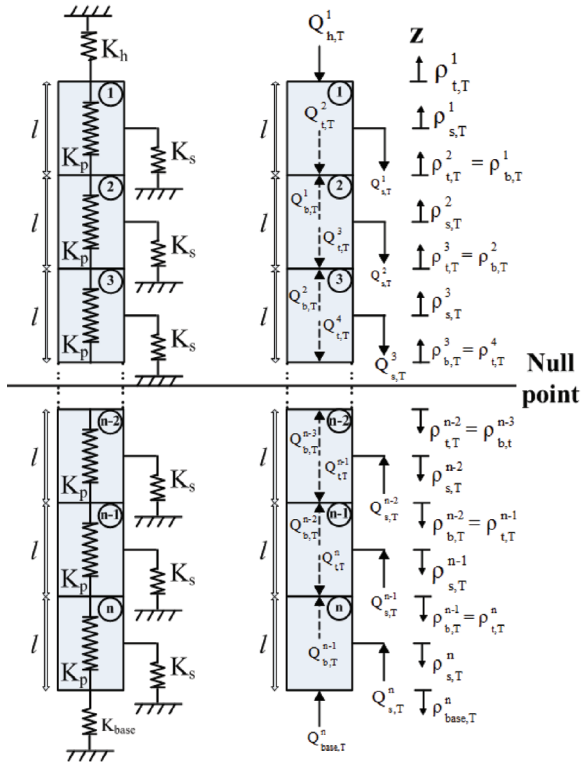

Figure 1-4 Thermo-mechanical soil-structure interaction model for heating: (a) Spring configuration; (b) Force and displacement variables.

1.4.2 Load-transfer curves

The displacement of the end of the foundation into the underlying soil is also represented using a nonlinear spring stiffness function referred to as a Q-z curve. Similarly, the mobilization of side shear resistance with displacement is typically described using a nonlinear spring stiffness function referred to as a T-z curve. The ordinate of the Q-z curve is the dimensionless end bearing, which is the ratio of the actual end bearing to the ultimate end bearing, while the abscissa is the relative displacement of the foundation toe. The ordinate of the T-z curve is the dimensionless side shear, equal to the ratio of the actual shearing stress to the shearing stress at failure (ultimate side shear resistance), while the abscissa is the relative displacement between the shaft element and surrounding soil. Under mechanical loading, the ultimate side shear resistance depends on the subsurface stratigraphy. Examples include a side shear resistance that is constant with depth in a uniform clay layer or a linearly increasing resistance with depth in a uniform sand layer.

As mentioned, upward side shear stresses will be mobilized in the lower half of the foundation during heating while downward side shear stresses will be mobilized in the upper half of the foundation. This will lead to different side shear stress-strain paths in the upper and lower halves of the foundation. When these mobilized side shear stresses due to thermal expansion are superimposed on the side shear stresses due to mechanical loading, the upper half of the foundation will follow an unloading path in the side shear stress-strain curve, while the lower half of the foundation will continue along the loading path in the side shear stress-strain curve. This phenomenon is shown schematically in Figure 1-5. If the mobilized side shear stresses due to mechanical loading are close to the ultimate side shear resistance of the soil-foundation interface, then the downward movement of the lower half of the foundation may fully mobilize the side shear resistance.

The Q-z and T-z curves are represented in this chapter using hyperbolic equations for simplicity. The side shear resistance (Q_s) and the base reaction (Q_{base}) at any relative displacement can be obtained using following equations:

$$Q_{\text{base}} = Q_{b,\max} \times \frac{\rho_{\text{base}}}{a_b + b_b \rho_{\text{base}}} \tag{7}$$

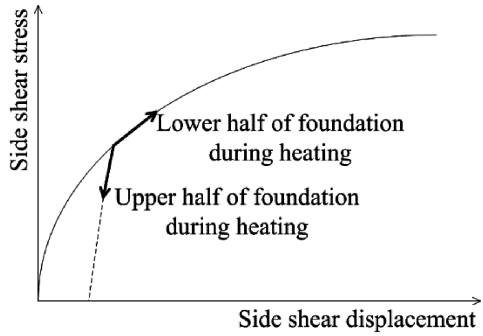

Figure 1-5 Representation of the mobilized side shear stress curve expected during heating of a semi-floating thermo-active foundation.

$$Q_s = Q_{s,\max} \times \frac{\rho_s}{a_s + b_s \rho_s} \tag{8}$$

where a_b, b_b, a_s and b_s can be selected based on the best fit to the experimental data. McCartney and Rosenberg (2011) used parameters for the Q-z and T-z curves of $a_b = 0.02$, $a_s = 0.0035$ and $b_b = b_s = 0.9$ in a simplified thermo-mechanical load transfer analysis involving thermo-active foundations in Bonny silt. These parameters were adopted for use in this chapter as the baseline conditions. Equation (8) represents the loading path of the T-z curve used to define the side shear resistance within the foundation for either mechanical analysis or thermo-mechanical analysis below the null point. The unloading path of the T-z curve used for thermo-mechanical analysis for the portion of the foundation above the null point can be defined as follows:

$$Q_s = Q_{s,\max} \times \left[\frac{\rho_s}{a_s} + \frac{Q_{s,i}}{Q_{s,\max}} - \left(\frac{1}{\frac{Q_{s,\max}}{Q_{s,i}} - b_s} \right) \right] \tag{9}$$

where $Q_{s,i}$ represents the initial side shear resistance after the mechanical loading is applied.

The baseline Q-z and T-z curves for a semi-floating thermo-active foundation used in the example analyses presented later in this chapter are shown in Figure 1-6. Although the shear strength data of Uchaipichat

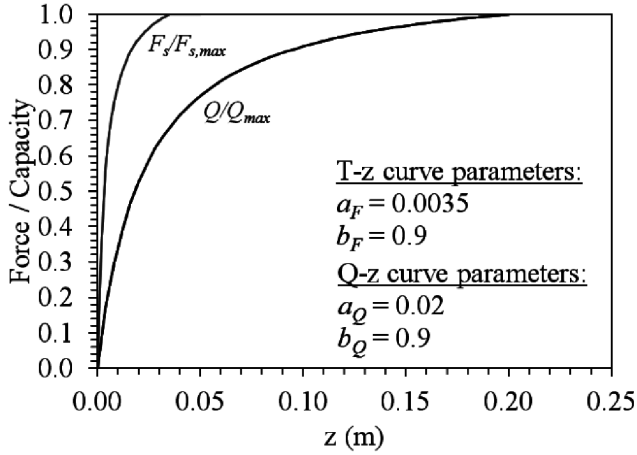

Figure 1-6 Comparison between the mobilized end bearing (Q-z) and side shear stress (T-z) curves used in the example analyses.

and Khalili (2009) indicates that the shear stress-strain curves of soil are affected by temperature, it is assumed that the Q-z and T-z curves do not depend on temperature. Development of temperature effects on the Q-z and T-z curves requires direct shear tests on the foundation-soil interface (Qian et al. 2014) or modified borehole shear tests (Murphy and McCartney 2015). The curves shown in Figure 1-6 are the same curves used by McCartney and Rosenberg (2011) in their load transfer analysis involving thermo-active foundations in Bonny silt.

1.4.3 Mechanical load transfer analysis

The value of the displacement at the bottom of the foundation z_{base} is used to initiate the mechanical load-transfer analysis. The value of Q_{base} can be defined as a function of the base displacement (ρ_{base}) using the Q-z curve. Then, the axial forces acting at the top and bottom of the elements along with their displacements at the top, bottom and middle can be calculated respectively. For a foundation discretized into n elements, the axial force acting at the bottom of element n can be defined using the Q-z curve. Specifically, the value of Q_{base} can be defined from the base displacement, which is used as an input to start the analysis. In this study, a base displacement corresponding which leads to a surface load representative of a building load was used to start the analysis.

The mechanical T-z analysis starts from element *n* (the element at the tip). Specifically, the reaction force Q_{base} can be calculated using an imposed value of ρ_{base}, as follows:

$$Q_{base} = f(\rho_{base}) \tag{10}$$

The average axial force in the element can be calculated by averaging the axial force at the top Q_t (initially zero) and bottom $Q = Q_{base}$ for element *n*. Q_{base} is the axial force acting at the bottom of element *n*, as follows:

$$Q_{ave} = \left(\frac{Q_{b,M} + Q_{t,M}}{2} \right) \tag{11}$$

Next, the elastic compression of element *n* (Δ) can be calculated by multiplying the average force Q_{ave} by the stiffness of the *K* of the element, as follows:

$$\Delta = Q_{ave} \times K \tag{12}$$

Next, the displacement at the side of the element $\rho_{s,M}$ is defined by adding the settlement at the bottom of the element plus one half the elastic compression of the element, as follows:

$$\rho_{s,M} = \rho_b + \frac{1}{2}\Delta_M \tag{13}$$

Next, the side force on the element $Q_{s,M}$ is then defined using the T-z curve and the displacement at the side $r_{s,M}$ calculated using Equation (6), as follows:

$$Q_{s,M} = f(\rho_{s,M}) \tag{14}$$

Finally, a new force at the top of the element $Q_{t,M,new}$ is defined by adding the force at the base of the element and the force on the side of the element to establish equilibrium, as follows:

$$Q_{t,M,new} = Q_{b,M} + Q_{s,M} \tag{15}$$

If the difference between the new and old forces on the top of the element is not less than a user-defined tolerance (a value of 10^{-6} m was

used in this study) then the new axial at the top of the foundation is used to calculate a new average axial stress and the process is repeated iteratively until convergence. The starting force for the top of the element for the each successive iteration is set equal to that of the previous iteration. If the difference is less than 10^{-6} m then the processes is repeated for the next element until the top of the foundation is reached.

The force on the bottom of a subsequent element $Q_{b,M}^{i-1}$ is equal to the new force on the top of the next element $Q_{t,M}^{i}$ and the settlement on the bottom of subsequent element $\rho_{b,M}^{i-1}$ is equal to the settlement of the next element $\rho_{b,M}^{i}$ plus the elastic compression of the foundation element (Δ_{M}^{i}), as follows:

$$Q_{b,M}^{i-1} = Q_{t,M}^{i} \tag{16}$$

$$\rho_{b,M}^{i-1} = \rho_{b,M}^{i} + \Delta_{M}^{i} \tag{17}$$

where the value of $\rho_{b,M}$ is equal to the value of $\rho_{t,M}$ defined for the lower element. The final load on the top of the foundation $Q_{t,M}$ will cause a corresponding head displacement $\rho_{t,M}$.

1.4.4 Thermo-mechanical T-z analyses

The load transfer (T-z) analysis method can also be used to predict the axial settlement and stress distribution in thermo-active foundations subject to thermal loading (i.e., without mechanical loading). In this regard, a spring should be added to the top of the foundation as shown in Figure 1-4, which represents the foundation head-structure stiffness (Knellwolf et al. 2011). This heat restraint stiffness is difficult to define, but it can be estimated by calibrating the load-transfer analyses with measurements of thermal axial strain after a building has been constructed. Recently, researchers have developed numerical models to account for thermal loads in the foundation in addition to mechanical loads from the overlying structure (Burlon et al. 2013; Mimouni and Laloui 2013). Numerical models have the capability of incorporating boundary conditions and temperature variations to gain a thorough understanding of the anticipated foundation displacements and stresses that will be generated during mechanical and thermal loading. Numerical modeling of specific site conditions can be used to construct design charts to anticipate the head load and displacement for an estimated foundation head stiffness and temperature change. However, at the

moment the only approach to obtain the head stiffness is to measure the thermal axial strain distributions using embedded instrumentation.

The null point location is an important variable to define in this process needed to define the thermal response of the thermo-active foundation during heating/cooling. As mentioned, the null point is the location in the foundation where there is no thermal expansion or contraction, assuming that the temperature change occurs uniformly throughout the foundation. In order for the displacement at the null point (denoted as NP) to be zero, the sum of the mobilized shear resistance and the structure reaction for the upper section of the null point should be equal to the sum of the mobilized shear resistance and the base reaction in the lower one (Knellwolf et al. 2011). The null point location can be defined by locating the node at which the thermal forces are in equilibrium, using the following equation:

$$\sum_{i=1}^{NP} Q_{s,T}^{i} + Q_{h,T} = \sum_{i=NP+1}^{n} Q_{s,T}^{i} + Q_{\text{base},T} \tag{18}$$

where:

$$Q_{h,T} = f(\rho_h, K_h) \tag{19}$$

$$Q_{\text{base},T} = f(\rho_{\text{base}}, K_{\text{base}}) \tag{20}$$

$$Q_{s,T}^{i} = f\left(\rho_s^i, K_s\right) \tag{21}$$

In these equations, $Q_{\text{base},T}$ represents the base response to the thermal expansion and contraction is defined using Q-z curve. $Q_{h,T}$ signifies the structure response and is linearly proportional to the relative displacement of the head of the foundation. $Q_{s,T}^{i}$ is the mobilized side shear resistance of the foundation and can be determined according to the T-z curve. K_s is the stiffness of the subsurface surrounding the thermo-active foundation. K_h represents the foundation head-structure stiffness, which depends on several factors including the rigidity of the supported structure, the type of contact between the foundation and the mat or raft, and the position and the number of thermo-active foundations (Knellwolf et al. 2011). K_{base} is the base material stiffness and depends on the initial slope of the Q-z curve. Alternatively, for the case of linear elastic material at the base of foundation, K_{base} is constant. The values of r_h and r_{base}

represent the relative displacements at the head and the base of the foundation. ρ_s^i is the relative displacement at the side of the element i. The null point location for hypothetical foundations with different boundary conditions will be discussed later. During heating or cooling, the foundation will expand or contract about the null point. The compressional/tensile forces acting on each element restrict the movements. These induced forces initiate from the base reaction, the structure reaction and the mobilized friction forces of the adjacent elements in the foundation.

To compute the first set of mobilized shear resistance and the base reaction, the foundation is assumed to be totally free to move (Knellwolf et al. 2011). Therefore the first set of displacements can be derived using following expression which l is the length of the element and i represents the element number along the foundation (i = 1 to n).

$$\Delta_T^i = l\alpha\Delta T \tag{22}$$

These displacements are restricted by the surrounding soil which applies additional forces tending to compress/expand the element during heating/cooling process. The null point can be located in any element along the foundation where the null point criterion is satisfied. The first element below the null point (noted as NP+1) has no displacement at its top and it expands/contracts only from the bottom during heating/cooling.

$$\rho_{t,T}^{NP+1} = 0 \tag{23}$$

The thermal settlement at the side and the bottom of this element can be defined using the following two equations:

$$\rho_{s,T}^{NP+1} = \pm\frac{\Delta_T^{NP+1}}{2} \tag{24}$$

$$\rho_{b,T}^{NP+1} = \pm\Delta_T^{NP+1} \tag{25}$$

In these equations, the upper sign is used when a foundation is heated, and the lower sign is used when a foundation is cooled. The relative displacements for the rest of the elements below the null point (i = NP+2 to n) can be calculated using the following equations:

$$\rho_{t,T}^{i} = \rho_{b,T}^{i-1} \tag{26}$$

$$\rho_{s,T}^{i} = \rho_{t,T}^{i} \pm \frac{\Delta_T^i}{2} \tag{27}$$

$$\rho_{b,T}^{i} = \rho_{t,T}^{i} \pm \Delta_T^i \tag{28}$$

When the base of the foundation is reached, the first set of base reaction forces along with the compressional/tensile stress acting on each element during heating/cooling can be calculated as follows (e.g., for $i = NP+1$ to n):

$$Q_{\text{base},T} = f(\rho_{b,T,n}) \tag{29}$$

$$Q_{b,T}^{n} = Q_{\text{base},T} \tag{30}$$

$$Q_{b,T}^{i} = Q_{t,T}^{i+1} \tag{31}$$

$$\sigma_i = \frac{Q_{ave}}{A} = \frac{(Q_{t,T}^{i} + Q_{b,T}^{i})}{2A} \tag{32}$$

After the forces acting on each element are defined, the next step is to define the actual displacement of each element as follows:

$$\Delta_{T\text{actual}}^{i} = \Delta_T^i - \frac{\sigma_i \cdot l}{E} \tag{33}$$

The actual displacement in each element will be lower than that present when the foundation is free to move from the bottom. This actual displacement should be replaced with the initial displacements (free boundary) in order to get a new actual displacement from Equation (33). This process should be repeated until the values of actual displacements reasonably converge (the difference between the new and old actual displacement is less than 10^{-6} m). For the elements above the null point (noted as NP-1, NP-2, etc.), a similar approach can be used.

A thermo-mechanical analysis involves applying thermal loading to a foundation that is under an initial mechanical load. To calculate the thermo-mechanical response of the thermo-active foundation, the first step is to calculate the distribution in axial and interface displacements and forces along the foundation for a given initial mechanical loading. Then the foundation response due to thermal loading (heating/cooling) will be applied subsequently to define the overall response of a foundation subject

to thermo-mechanical loading. Calculations of the thermal displacements are stresses in the thermo-mechanical analysis should be started from the null point. Opposite to the thermal algorithm, this algorithm starts from non-zero relative displacement about the null point. Similar to thermal algorithm, the initial displacements are considered to be the same as free boundary condition ($\Delta_T^i = l\alpha\Delta T$). The following equations are used for the first element below the null point (the upper and the lower sign in following equations is used for a foundation which is heated or cooled respectively):

$$\rho_{t,M,T}^{NP+1} = \rho_{t,M}^{NP+1} \tag{34}$$

$$\rho_{s,M,T}^{NP+1} = \rho_{s,M}^{NP+1} \pm \frac{\Delta_T^{NP+1}}{2} \tag{35}$$

$$\rho_{b,M,T}^{NP+1} = \rho_{b,M}^{NP+1} \pm \frac{\Delta_T^{NP+1}}{2} \tag{36}$$

The relative displacements for the rest of elements below the null point ($i = NP+2$ to n), can be defined using the following equations:

$$\rho_{t,M,T}^{i} = \rho_{b,M,T,i-1} \tag{37}$$

$$\rho_{s,M,T}^{i} = \rho_{t,M,T}^{i} \pm \frac{\Delta_T^i}{2} \tag{38}$$

$$\rho_{b,M,T}^{i} = \rho_{t,M,T}^{i} \pm \Delta_T^i \tag{39}$$

When the base of the foundation is reached, the first set of base reaction force and also the compressive/tensile forces acting on each element during heating/cooling can be calculated. Before calculating these stresses the process should continue to define the relative displacements for the elements above the null points. To calculate the actual displacement of each element, the compressive/tensile forces acting on each element can be defined using the following equations:

$$Q_{\text{base},M,T} = f(\rho_{b,T,n}) \tag{40}$$

$$Q_{t\cdot M,T}^{i} = Q_{\text{base},T} + \sum_{j=n}^{i} Q_{s\cdot M,T}^{j} \tag{41}$$

$$Q^{i}_{b\cdot M,T} = Q^{i+1}_{t\cdot M,T} \tag{42}$$

$$\sigma_i = \frac{Q_{ave}}{A} = \frac{(Q^{i+1}_{t\cdot M,T} + Q^{i}_{b\cdot M,T})}{2A} \tag{43}$$

$$\Delta_{M,T\text{actual}} = \Delta_{T,i} - \frac{\sigma_i \cdot l}{E} \tag{44}$$

The axial force calculations should start from the base, up to the element of interest ($j = n$ to i, where i is the element number). The mobilized side shear forces due to thermal expansion ($Q^{j}_{s\cdot M,T}$) for the elements above the null point of the foundation will follow an unloading path in the T-z curve, while that for the elements below the null point will continue along the loading path. To determine for the elements above the null point the unloading path of the T-z curve should be used. The value of $Q^{j}_{s\cdot M,T}$ for the elements below the null point can be defined using the loading path of the T-z curve. The actual displacement should be replaced with the initial displacements (free boundary) in order to get a new actual displacement and this process should be repeated until the values of actual displacements converge (when the difference between the new and old actual displacements is less than 10^{-6} m).

1.4.5 Model evaluation: impact of temperature changes

A hypothetical prototype foundation with a length of L = 10 m and a diameter of D = 1 m was used to evaluate soil-structure interaction mechanisms for different scenarios. The coefficient of thermal expansion of the shaft is assumed to be $\alpha_T = -10\,\mu\varepsilon/°C$. The unit weight and the Young's modulus of the foundation are assumed to be $\gamma_f = 24\ kN/m^3$ and $E_f = 20$ GPa respectively. A soil having a drained friction angle (ϕ_s) of 30° (for an ultimate side shear resistance that increases with depth), unit weight (γ_s) of 18 kN/m^3 and an undrained shear strength of c_u = 54 kPa (for estimation of the ultimate end bearing using Skempton's bearing capacity equation) are assumed for the soil surrounding the foundation. The same T-z curves from Figure 1-6 are used in all of the analyses, but the Q-z curves are changed to represent different end restraint boundary conditions. The effect of side shear resistance using the model proposed by McCartney and Rosenberg (2012) was also incorporated into the analysis.

An evaluation of the impact of temperature changes on different soil-structure interaction variables in a floating foundation is shown in Figure 1-7. The results in Figure 1-7(a) indicate that the thermal axial strain is negative during heating, indicating expansion. The thermal axial strain increases proportionally to the change in temperature. The thermal axial strain is almost constant in the upper 2/3 of the foundation,

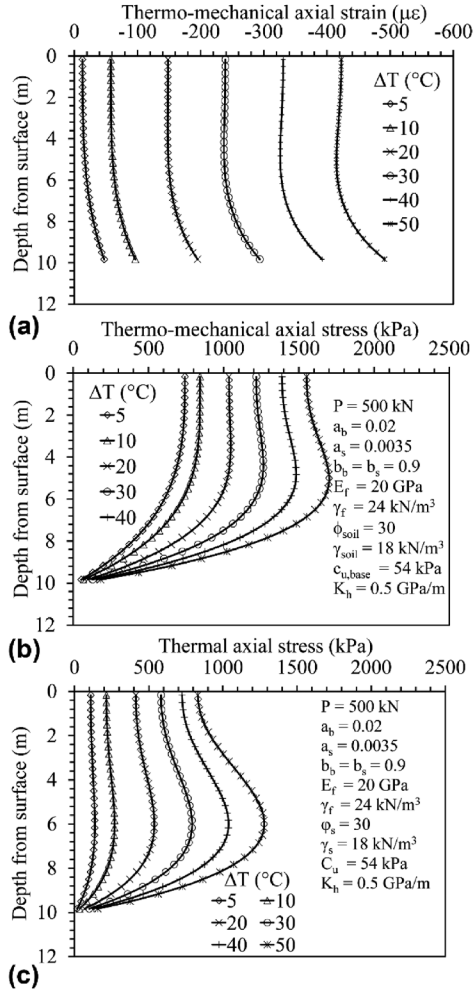

Figure 1-7 Impact of temperature change on soil-structure interaction in a floating thermo-active foundation: (a) Thermo-mechanical axial strain; (b) Thermo-mechanical axial stress; (c) Thermal axial stress.

then increases near the toe, indicating greater downward expansion. This is likely due to the relatively soft value of K_b calculated from the Q-z curve compared to the value of K_b used in the analysis. The change in the shape of the curves with temperature is due to the linear increase in ultimate side shear with depth, and due to the effects of radial expansion. It is also partially related to the fact that different elements along the length of the foundation will start from different initial points on the T-z curve due to initial mechanical loading.

The values of thermo-mechanical stress in Figure 1-7(b) indicate that the maximum stress occurs near the top of the foundation and decreases with the depth. The thermal axial stress shown in Figure 1-7(c) shows that heating causes the greatest increase in stress in the middle of the foundation. The results in this figure indicate that the compressive stress and strain are inversely related. The peak value of thermal stress coincides with the location of the null point. The null point corresponds to the point where the foundation does not move and thus has the highest restraint due to soil-structure interaction. The point of highest restraint should correspond with the highest thermal axial stress. For the soil and foundation parameters, the maximum predicted thermo-mechanical axial stress is significantly lower than the compressive strength of reinforced concrete, even when an extreme heating situation was considered ($\Delta T = 50$ °C).

1.4.6 Model evaluation: impact of boundary conditions

The plots in Figure 1-8 show a comparison between the mechanical axial stress, the thermal axial stress, and thermo-mechanical axial stress in thermo-active foundations with three types of boundary conditions undergoing an increase in temperature of 20 °C. All three foundations have the same soil properties except for those corresponding to the end restraint (the Q-z curve), and the building load and foundation head-structure stiffness used in the analysis were P = 500 kN and K_b = 0.5 GPa/m, respectively. The results in Figure 1-8(a) are for a floating shaft. The mechanical axial stress is observed to decrease nonlinearly with depth, and heating causing an increase in axial stress primarily in the middle portion of the foundation. An increase in compressive axial stress of about 40% is observed due to the change in temperature. The results in Figure 1-8(b) are for a semi-floating foundation. Although similar to the floating shaft, a greater axial stress is observed at the toe of the foundation after both mechanical and thermal loading. The results in Figure 1-8(c) are for an

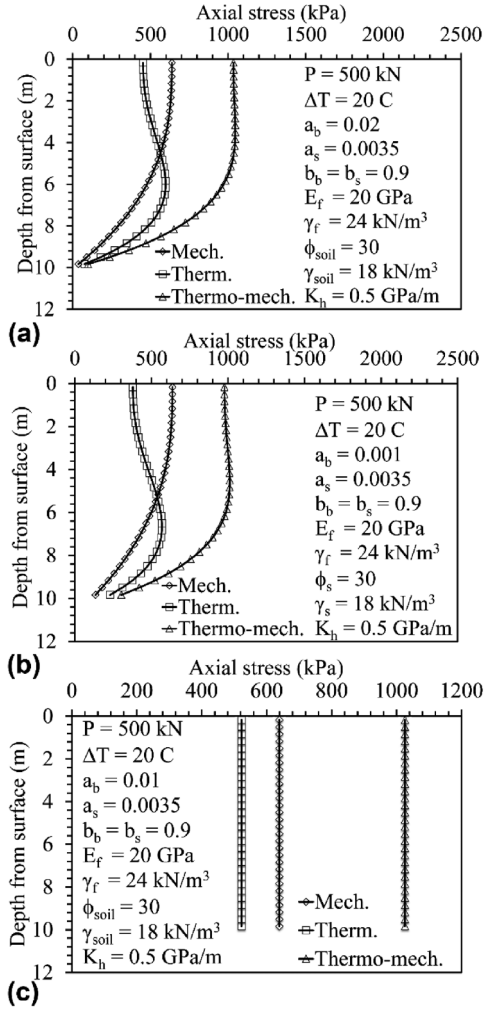

Figure 1-8 Comparison between different end restraint conditions: (a) Floating thermo-active foundations; (b) Semi-floating thermo-active foundation; (c) End-bearing thermo-active foundation.

end-bearing foundation. Because the end spring was set to such a high stiffness value, essentially all of the mechanical and thermal loads were resisted by the toe of the foundation. The side shear resistance had relatively little effect on the thermal axial stress, which corresponds to the average of the springs and the head and toe of the foundation.

1.4.7 Model evaluation: head restraint effects

Another parameter than can have a significant effect on the thermo-active foundation's response is the head-structure stiffness. This parameter can potentially govern the design of a thermo-active foundation, as it controls the magnitude of thermal axial stress during heating (Burlon et al. 2013; Mimouni and Laloui 2014). The thermal axial strain and stress in a floating foundation with the same parameters as those evaluated in the previous section are shown in Figures 1-9(a) and (b), respectively. As the value of K_h is changed over four orders of magnitude, the thermal axial

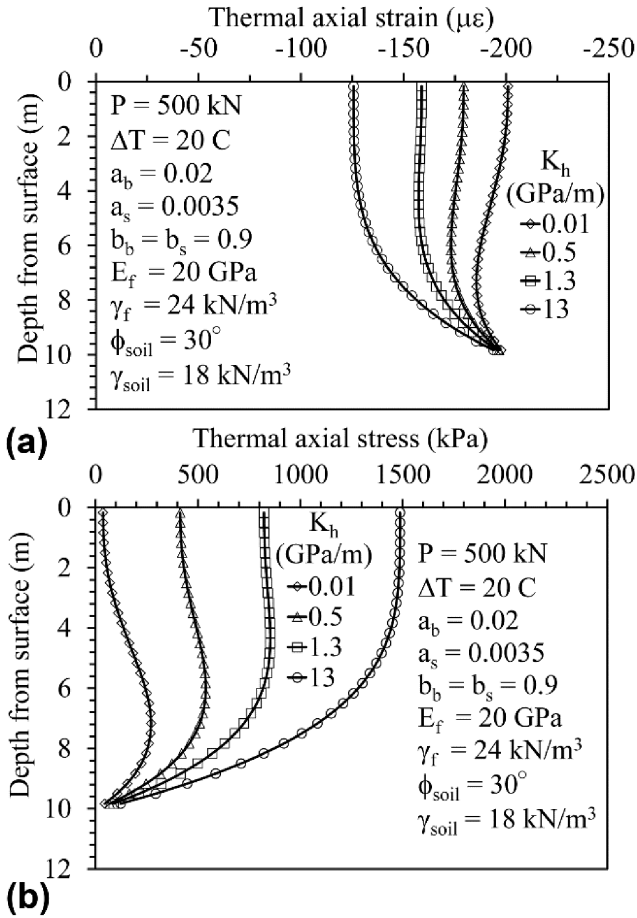

Figure 1-9 Impact of head-structure stiffness on soil-structure interaction in a floating thermo-active foundation: (a) Thermal axial strain; (b) Thermal axial stress.

stress at the head of the foundation increases from approximately 50 to 1500 kPa. This can have a significant impact when superimposed atop the mechanical axial stresses, which are usually greatest at the head of the foundation. The null point, which corresponds to the maximum axial stress and minimum axial strain, also moves upward as the magnitude of K_h increases.

1.4.8 Results from thermo-active foundations

The mechanisms of thermo-mechanical effects on thermo-active foundations can be evaluated using data from two early case histories, as well as from several new case histories in different soil deposits. The two early case histories were presented by Bourne-Webb et al. (2009), who performed a series of thermal and mechanical loading tests on a full-scale foundation in England, and Laloui and Nuth (2006), who performed a series of thermal and mechanical loading tests on a full-scale foundation in Switzerland. Additional analyses of the foundation introduced by Bourne-Webb et al. (2009) were reported by Amatya et al. (2009) and Ouyang et al. (2012), while additional analyses of the foundation introduced by Laloui and Nuth were reported by Laloui et al. (2006) and Laloui (2011). The foundation tested by Bourne-Webb et al. (2009) was a 0.56 m diameter drilled shaft with a depth of 22.5 m, containing three polyethylene heat exchange loops. The lower 18.5 m of the foundation is in London clay with the rest of the foundation in cohesionless and fill material. The foundation tested by Laloui and Nuth (2006) was a 25.8 m-long drilled shaft having a diameter of 0.88 m. The upper 12 m of the foundation was in alluvial soils, while the lower part of the foundation was in glacial moraine material.

Bourne-Webb et al. (2009) loaded their foundation to 1200 kN, cooled it to −6 °C, and then heated it to 40 °C. Laloui and Nuth (2006) loaded their foundation to 2140 kN, increased the temperature by 21 °C above the natural ground temperature, then cooled it to 3 °C above the natural ground temperature. The strain distributions in the foundations tested by Bourne-Webb et al. (2009) were measured using fiber optic cables, while Laloui and Nuth (2006) used vibrating wire strain gages. The initial strain value at the bottom of the foundation measured by Bourne-Webb et al. (2009) indicates that there was a slight mobilization of end bearing during mechanical

loading, but that the foundation represented an end-bearing foundation. A small tensile stress was noted in the bottom of the foundation tested by Bourne-Webb et al. (2009). Overall, the observations from the field after loading then heating or cooling are consistent with the schematic strain distributions in Figure 1-2. Both studies converted their measured strain values to stress. Bourne-Webb et al. (2009) observed minimum and maximum thermal axial stresses of −0.8 to 1.9 MPa, respectively, while Laloui and Nuth (2006) observed a maximum thermal axial stress of 2.1 MPa.

For a foundation that was not loaded axially, Laloui et al. (2006) observed a heave of −4 mm for the foundation head during an increase in temperature of 21 °C over the period of 1 day. The foundation did not return to its original elevation upon cooling, but maintained an upward displacement of approximately −1 mm. Bourne-Webb et al. (2009) observed a downward settlement of 4 mm during cooling and an upward heave of −2 mm during heating. The amount of movement and stresses in the foundation depends on the end-restraint of the foundation by the lower bearing stratum and the building load (Bourne-Webb et al. 2009). Although the movements are minor, Laloui et al. (2006) indicated that the increase in temperature may have led to a plastic response in the surrounding soil. The soil was observed to partially recover deformations after cycles of heating and cooling, causing permanent foundation movement (Laloui et al. 2006).

To consider the implications of thermal-induced movements in the foundation, engineers in Switzerland double the design factor of safety for ultimate capacity for thermo-active foundations from that used for conventional foundation design (Boënnec 2009). Bourne-Webb et al. (2009) reported that a design safety factor of 3.5 for ultimate capacity was used in the design of the thermo-active foundation system for the building constructed atop the thermo-active foundation at Lambeth College in the UK. The justification for such conservatism in safety factors is being investigated, as it may effectively require twice as many foundations to support the same building load.

Two additional case histories in Colorado have been performed that expand the database of soil-structure interaction information to dry sandstone and claystone. The first case history includes two thermo-active foundations with depths of 14.8 m (Foundation A) and 13.4 m (Foundation B) and diameters of 0.91 m under the 8-story Denver

Housing Authority (DHA) Senior Living Facility (McCartney and Murphy 2012; Murphy and McCartney 2015). The details of the subsurface layers under the DHA building are summarized in Table 1-2. The second case history involves a set of 8 thermo-active foundations with depths of 15.24 and diameters of 0.6 m were constructed under a new 1-story building at the US Air Force Academy (USAFA). The details of the subsurface layers beneath the USAFA building are summarized in Table 1-3 (Murphy et al. 2015).

Table 1-2 Summary of stratigraphy encountered during subsurface exploration at the DHA site.

Depth to bottom of stratum (m)	Material encountered	SPT N-value (blows/ 300 mm)	Gravimetric water content (%)	Dry unit weight (kN/m^3)
3.0	Urban fill, 20% fines	7–8	10–13	14.4–16.5
7.6	Sandy gravel	19 to 28	1 to 8	18.1 to 19.2
14.8+	Claystone	50/200 mm	N/A	N/A

Table 1-3 Summary of stratigraphy encountered during subsurface exploration at the USAFA site.

Depth to bottom of stratum (m)	Material encountered	SPT N-value (blows/ 300 mm)	Gravimetric water content (%)	Dry unit weight (kN/m^3)
1.0	Sandy fill with silt and gravel	70	5	18.4
2.0	Dense sands, silt, and gravel	85	7	19.2
12.0+	Silty sandstone	50/25.4 mm	N/A	N/A

The thermal axial strains were measured in the different foundations at both sites using vibrating wire strain gages. More details of the instrumentation characteristics and layout are described in the papers listed above. The foundations at DHA have been heated and cooled in cycles over more than 2 years of heat pump operation, while the foundations at USAFA have been characterized in a monotonic heating and cooling test. Comparison of the results from both sites provides insight into the effect of soil-structure interaction mechanisms. This study focuses on the behavior of Foundation B from the DHA site and Foundations 3 and 4 from the USAFA site. The two foundations at the USAFA site have the same heat exchanger configuration, but Foundation 3 has less head restraint than foundation 4 as it is under the corner of the building. Accordingly, the overlying grade beam does not provide as stiff of an upward reaction (a smaller value of K_b).

During heating and cooling, the foundations at DHA experienced nonlinear changes in thermal axial strain with temperature, following a hysteretic path. On the other hand, the foundations at USAFA experienced linear changes in thermal axial strain with changes in temperature with very little hysteresis. This may have been due to the difference in soils at both sites. An interesting variable to evaluate soil-structure interaction is the mobilized coefficient of thermal expansion. This is the slope of the relationship between ε_T and ΔT (e.g., α). The results shown in Figure 1-10 show the mobilized values of α for the three foundations.

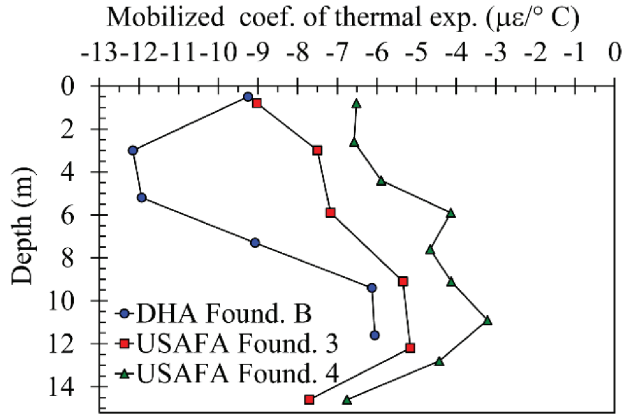

Figure 1-10 Profiles of the mobilized coefficient of thermal expansion in full-scale thermo-active foundations.

For each foundation, the mobilized coefficient of thermal expansion was less than that of free expansion (α_c = −12 με/°C for the foundations at USAFA and α_c = −13 με/°C for the foundations at DHA), indicating that side shear resistance and the end restraint boundary conditions prevented the foundation from expanding as much as it possibly could in free-expansion conditions. The lowest mobilized values of α occurred near the toe of the foundations, indicating that they all behave as expected for end-bearing foundations. USAFA Foundation 3 exhibited slightly greater mobilized coefficients of thermal expansion likely due to the lower amount of restraint provided by the corner of the building. A higher mobilized value of a was observed near the toe of USAFA Foundations 3 and 4, perhaps because of inadequate clean-out of cuttings from the base of the excavated holes.

An instance in time was identified for each of the three foundations where the average change in temperature (ΔT_{ave}) was approximately 12 °C, so that the different soil-structure interaction variables could be compared. The foundation temperatures for this instance in time are shown in Figure 1-11. Although the ground temperature at DHA was slightly higher than that at USAFA, the temperatures in the foundations were relatively constant. It is possible that the lower temperature measured in USAFA Foundation 3 could have been due to a further

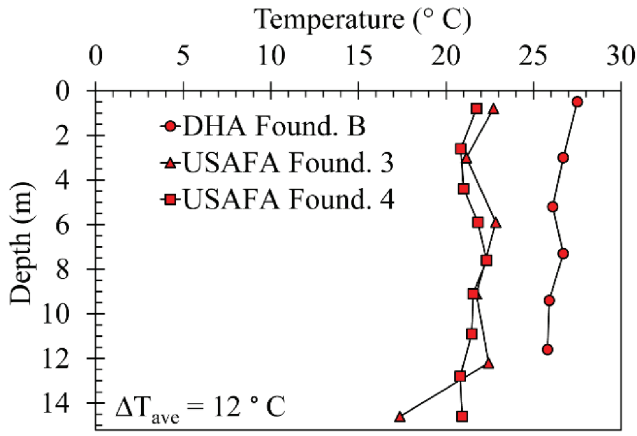

Figure 1-11 Profiles of temperature in full-scale thermoactive foundations for the same average change in foundation temperature during heating.

distance from temperature sensor to the bend in the U-tube at the base of the foundation. Nonetheless, the assumption that the temperature is constant in the foundation is useful when assessing the axial strain, displacement and stress distributions.

Profiles of thermal axial strain in the three foundations are shown in Figure 1-12 for the same instance in time as the temperature profiles in Figure 1-11. The shapes of the thermal axial strain profiles approximately follow a mirror image of the mobilized coefficients of thermal expansion shown in Figure 1-10. The greatest strains were observed near the head of the foundations. A lower thermal axial strain was measured throughout USAFA Foundation 3 than in USAFA Foundation 4 due to the lower head restraint.

Profiles of thermo-mechanical axial stress are shown in Figure 1-13 for the three foundations. The profiles for the two USAFA foundations follow a nonlinear trend with depth, similar to the predicted curves for semi-floating foundations in Figure 1-8. The greatest stress was observed at the head of the foundations due to the impact of the overlying structure. The foundation at DHA shows a more erratic profile with depth. This was partially due to the high thermal axial strains that were observed in the sandy gravel layers near the ground surface, but also due to the inconsistent mechanical strain profile measured by the strain gages during construction of the building. The mechanical axial strains did

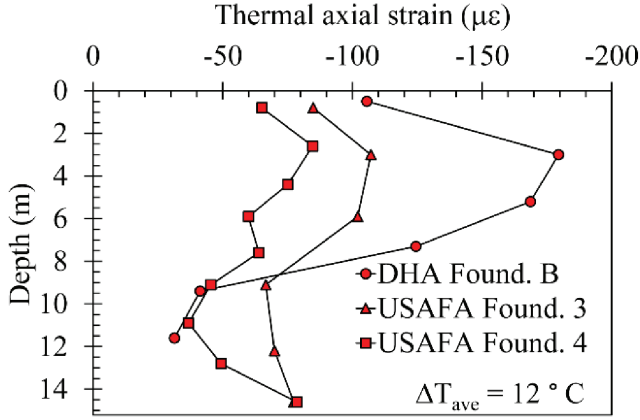

Figure 1-12 Profiles of thermal axial strain in full-scale thermo-active foundations for the same average change in foundation temperature during heating.

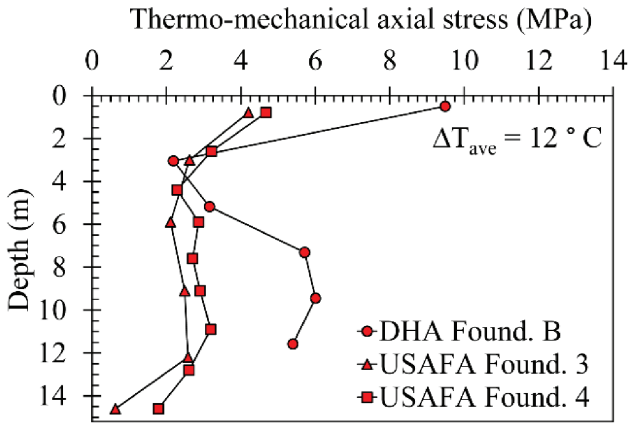

Figure 1-13 Profiles of thermal axial stress in full-scale thermo-active foundations for the same average change in foundation temperature during heating.

not follow a monotonically decreasing trend with depth. This may be due to the effects of mechanical downdrag of the fill layers on the foundation, which occurred over time. Nonetheless, similar to the observations from Bourne-Webb et al. (2009) and Laloui and Nuth (2006), the maximum values of the thermo-mechanical axial stress during heating were less than the compressive strength of reinforced concrete. The three foundations were heated to higher temperatures than that corresponding to the stresses this figure, but the same conclusion holds.

Profiles of relative displacement in the three thermo-active foundations are shown in Figure 1-14. These profiles are plotted with a toe displacement of zero, and are thus relative to the actual movement of the toe, which is unknown. For an end-bearing foundation, it is expected that the null point should be close to the toe. If this were the case, then the maximum upward movement of the head of –1.3 mm during a change in temperature of 12 °C. On the other hand, if loose cuttings are present at the toe, it is possible that the null point would move upward and lower head displacements would occur. If the toe does not move, the maximum upward displacements will lead to an angular distortion δ/L_s (where δ is the difference in displacements of two adjacent thermo-active foundations and L_s is the horizontal spacing between the foundations) of less than 1/5000. This value is lower than the

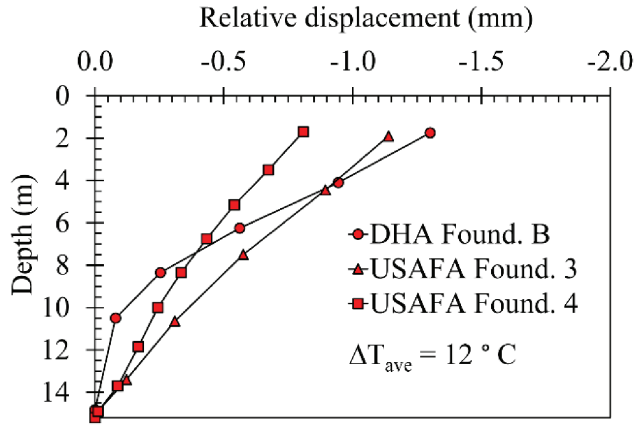

Figure 1-14 Profiles of displacement in full-scale thermo-active foundations for the same average change in foundation temperature during heating.

limit expected to cause architectural damage in the building (Skempton and MacDonald 1956; Bjerrum 1963). The displacement profiles for the USAFA foundations are relatively linear with depth, possibly due to the fact that the subsurface is relatively uniform, dry sandstone. Lower displacements are observed for USAFA Foundation 4 than for USAFA Foundation 3 due to the greater head restraint on USAFA Foundation 4. The displacement profiles for the DHA profile are more nonlinear, possibly due to the high strains observed in the sandy gravel layer.

The ranges in values for the three foundations are consistent with those observed from the other full-scale foundations reported in the literature. The change in thermal axial stress with the change in temperature for the three foundations are shown along with published data from the literature in Figure 1-15. The depth corresponding to the greatest increase of thermal stress within each foundation was used to define the maximum rates of axial stress during heating. The depths shown correspond to the null point of each foundation and show the greatest thermal axial stress rate. Slopes of σ_t = 210ΔT to 260ΔT were determined from the results in this study, which are slightly higher than values from Laloui et al. (2006) and Bourne-Webb et al. (2009), but are consistent with those calculated from the results of McCartney and Murphy (2012). This may be due to the greater coefficient of thermal

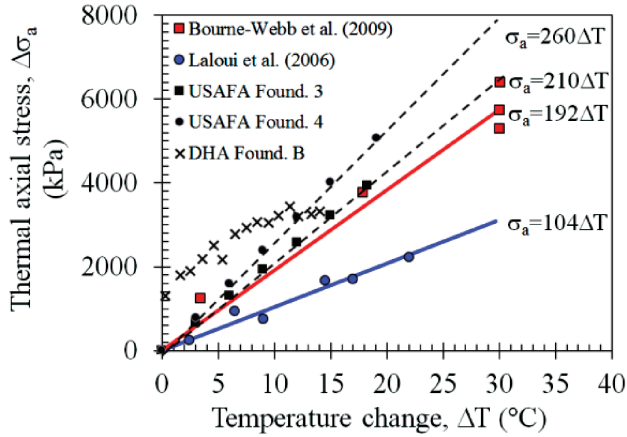

Figure 1-15 Change in thermal axial stress with temperature for different full-scale thermo-active foundations.

expansion of the reinforced concrete for the energy piles evaluated in this study equal to −12 με/°C, which is slightly higher than the value of −9.5 με/°C used in the studies of Laloui et al. (2006) and Bourne-Webb et al. (2009). An interesting observation is that the change in stress with temperature for the DHA foundation is more nonlinear than the other foundations, and is offset from zero due to the hysteresis in the relationship between ε_T and ΔT mentioned earlier. If the offset were neglected, then the slope of this line is in the same range as the other foundations. The nonlinearity and the hysteresis for the DHA foundation may be due to the soil stratigraphy at the sites, but it could also be due to the fact that several cycles of heating and cooling have been applied to the foundation while the others had only been heated and cooled monotonically.

A summary of the results from the different foundation studies is presented in Table 1-4. This table includes the geometry details along with the temperature ranges investigated and the observed values of thermal axial stress ranges and thermal axial deformations. Evaluation of the results presented in this table indicate that despite thermo-mechanical soil-structure interaction, all of the systems have safe behavior from both structural and performance criteria.

Although the results presented in this chapter indicate that energy piles provide a sustainable solution, there are still additional phenomena

Table 1-4 Summary of results from energy pile studies in the literature.

Case	Laloui et al. (2006)	Bourne-Webb et al. (2009)	USAFA Murphy et al. (2015)	Murphy and McCartney (2015)	Olgun et al. (2012)
Diameter (m)	0.88	0.56	0.61	0.61	0.25
Length (m)	25.8	23	15.2	15.2	30.5
Applied load (kN)	0, 1300	1200	400	883	950
Range of ΔT (°C)	+21, +13	−19 to +29	+22	+19	+30
Depth of $\sigma_{t,max}$ (m)	21.0	17.0	11.6	12	12.7
Range of σ_t (kPa)	2100	−800 to 1900	5200	4500	780
$(\Delta\sigma_t/\Delta T)_{max}$ (kPa/°C)	104	192	252	48	408
Head displacement (-up) (mm)	−4.2, n.m.	4.0 to −2.0	−1.75	−1.4	−1.3 to 0.6

that need to be studied in more detail regarding soil-structure interaction in energy piles. In model-scale tests performed in the centrifuge, McCartney et al. (2010b) observed that cooling a thermo-active foundation back to ambient conditions after heating led to positive effects in the side-shear resistance due to consolidation of the soil surrounding the foundation. Further, due to the radial expansion of the foundation, the ultimate side shear which can be mobilized may increase if there is differential radial expansion between the foundation and surrounding soil leading to an increase in radial confining stress (McCartney and Rosenberg 2012). The role of the pile head restraint needs to be further examined experimentally and theoretically (Burlon et al. 2013; Goode and McCartney 2014, 2015). In addition, the soil surrounding the thermo-active foundation is exposed to temperature changes which can induce excess pore pressures, volume changes and degradation of

the strength of the soil at the pile interface. Pore water migration away from the thermo-active foundation can reduce the thermal conductivity and also cause desaturation of the soil at the pile interface (Wang et al. 2015). These issues may have been additional causes of the nonlinear behavior noted in the DHA foundation. Finally, the impact of heat exchange on the lateral loading behavior of energy piles is an important issue to consider.

When making the decision to convert conventional building foundations into energy piles, it is not economical to add additional energy piles to meet the thermal demand of a building. McCartney et al. (2010b) provided a simple analysis that investigated the number of piles required to support a building with the number that would be required to provide the thermal energy demand of the building. Except in very problematic soil profiles, the number of energy piles required for structural support of the building is likely smaller than that required. This implies that the energy piles must be augmented by a backup system, which could either consist of a set of vertical or horizontal heat exchangers, or a boiler or air-source heat pump system to provide additional thermal energy.

1.5 Final comments

This chapter presented the general concepts of soil-structure interaction in thermo-active foundations, relevant design criteria, the details of a load-transfer analysis that can be used to predict the complex interaction between soils and foundations during mechanical and thermal loading, and the results from relevant case histories. The analyses of some representative cases (floating, semi-floating and end bearing foundations) indicates the importance of understanding the restraints at the head and toe of the foundation. The T-z model analysis provided an estimate of axial compressive stress induced by the different thermal loadings in the foundation that is consistent with the trends observed in full-scale studies. Overall, the results of the load-transfer model shows promise as an approach to provide an estimate for the thermal analysis of a thermo-active foundation.

Although the available information supports the feasibility of thermo-active foundations in terms of their structural response, there are still several issues that need to be further investigated regarding their long-term sustainability in developing comprehensive design guidance. The

effect of cyclic temperature-induced changes in thermo-active foundation performance is one area of interest. Thermo-active foundation are exposed to daily and seasonal temperature changes which result in expansion and contraction of the foundation, which may induce cyclic degradation of mobilized shear stresses at the soil-foundation interface which can affect the stress transfer between the soil and the foundation.

1.6 Acknowledgments

Support from NSF grant CMMI 0928324 and DoD ESTCP grant EW-201153 are gratefully acknowledged. The contents of this paper reflect the views of the authors and do not necessarily reflect the views of the sponsor.

1.7 References

Abdelaziz, S.L., Olgun, C.G., and Martin, J.R., II (2011). "Design and operation considerations of geothermal energy foundations." *GeoFrontiers 2011 (GSP 211)*. J. Han and D.E. Alzamora, eds. ASCE, Reston VA. 450–459.

Adam, D. and Markiewicz, R. (2009). "Energy from earth-coupled structures, foundations, tunnels and sewers." *Géotechnique*. 59(3), 229–236.

Akrouch, G., Sanchez, M., and Briaud, J.-L. (2014). "Thermo-mechanical behavior of energy piles in high plasticity clays." *Acta Geotechnica*. 9(3), 399–412.

Amatya, B.L., Soga, K., Bourne-Webb, P.J., Amis, T., and Laloui, L. (2012). "Thermo-mechanical behaviour of energy piles." *Géotechnique*. 62(6), 503–519.

Bjerrum, L. (1963). "Allowable settlement of structures." *Proc., European Conf. on Soil Mech. and Found. Engr.,* Wiesbaden, Germany, Vol. 3, 135–137.

Boënnec, O. (2009). "Piling on the Energy." *Geodrilling International*.

Bourne-Webb, P.J., Amatya, B., Soga, K., Amis, T., Davidson, C., and Payne, P. (2009). "Energy pile test at Lambeth College, London: Geotechnical and thermodynamic aspects of pile response to heat cycles." *Géotechnique*. 59(3), 237–248.

Brandl, H. (2006). "Energy foundations and other thermo-active ground structures." *Géotechnique*. 56(2), 81–122.

Brettmann, T. and Amis, T. (2011). "Thermal conductivity evaluation of a pile group using geothermal energy piles." *Proc., GeoCongress 2012 (GSP 225)*, R. D. Hryciw, A. Athanasopoulos-Zekkos, and N. Yesiller, eds., ASCE, Reston, VA. 4436–4445.

Burlon, S., Habert, J., Szymkievicz, F., Suryatriyastuti, M., and Mroueh, H. (2013). "Towards a design approach of bearing capacity of thermo-active piles." *European Geothermal Congress*, Pisa. 1–6. (CD-ROM).

Coduto, D. (2000). Foundation Design: Principles and Practices. 2nd Edition. *Prentice Hall*. Upper Saddle River. New Jersey.

Coyle, H.M. and Reese, L.C. (1966). "Load transfer for axially loaded piles in clay." *Proc. American Society of Civil Engineers*, New York, NY. 92(SM2), 1–26.

Energy Information Administration (EIA). (2008). *Annual Energy Review*. Report No. DOE/EIA-0384(2008).

Ennigkeit, A. and Katzenbach, R. (2001). "The double use of piles as foundation and heat exchanging elements." *Proc. 15th International Conference on Soil Mechanics and Geotechnical Engineering*. Istanbul, Turkey. 893–896.

Goode, J.C., III, Zhang, M., and McCartney, J.S. (2014). "Centrifuge modeling of energy foundations in sand." *Physical Modeling in Geotechnics: Proc. 8th International Conference on Physical Modelling in Geotechnics*. Perth, Australia. Jan. 14–17. C. Gaudin and D. White, eds. Taylor and Francis. London. 729–736.

Goode, J.C., III and McCartney, J.S. (2014). "Evaluation of head restraint effects on energy foundations." *Proc. GeoCongress 2014 (GSP 234)*, M. Abu-Farsakh and L. Hoyos, eds. ASCE. pp. 2685–2694.

Goode, J.C., III and McCartney, J.S. (2015). "Centrifuge modeling of boundary restraint effects in energy foundations." *Journal of Geotechnical and Geoenvironmental Engineering*. 04015034-1-04015034-13.

GSHP Association. (2012). Thermal Pile Design, Installation and Materials Standards. Issue 1.0 Milton Keynes, UK.

Hughes, P.J. (2008). Geothermal (Ground-Source) Heat Pumps: Market Status, Barriers to Adoption, and Actions to Overcome Barriers. Oak Ridge Nat. Lab. Report ORNL-2008/232.

Kavanaugh, S., Rafferty, K., and Geshwiler, M. (1997). Ground-Source Heat Pumps—Design of Geothermal Systems for Commercial and Industrial Buildings. *ASHRAE*. 167 pg.

Knellwolf, C., Peron, H., and Laloui, L. (2011). "Geotechnical analysis of heat exchanger piles." *Journal of Geotechnical and Geoenvironmental Engineering. ASCE*. 137(12), 890–902.

Kramer, A.C. and Basu, P. (2014). "Performance of a model geothermal pile in sand." *Proc. 8th International Conference on Physical Modelling in Geotechnics*, Perth, Jan. 14–17. 771–777.

Laloui, L. (2011). "In-situ testing of heat exchanger pile." GeoFrontiers 2011 (GSP 211). J. Han and D.E. Alzamora, eds. *ASCE*, Reston VA. 410–419.

Laloui, L., Nuth, M., and Vulliet, L. (2006). "Experimental and numerical investigations of the behaviour of a heat exchanger pile." *International Journal for Numerical and Analytical Methods in Geomechanics*. 30, 763–781.

Laloui, N. and Nuth, M. (2006). "Numerical modeling of some features of heat exchanger pile." *Foundation Analysis and Design: Innovative Methods (GSP 153). ASCE*. Reston, VA. 189–195.

Loveridge, F. and Powrie, W. (2012). "Pile heat exchangers: Thermal behaviour and interactions." *Proc. ICE – Geotechnical Engineering.* 166(GE2), 178–196.

Loveridge, F., Olgun, C.G., Brettmann, T., and Powrie, W. (2015). "The thermal behaviour of three different auger pressure grouted piles used as heat exchangers." *Geological and Geotechnical Engineering*. 32(3), 1–17.

Loveridge F. and Powrie W. (2014). "2D thermal resistance of pile heat exchangers." *Geothermics*. 50, 122–135.

McCartney, J.S. (2011). "Engineering performance of energy foundations." *PanAm CGS Geotechnical Conference*. Toronto. Oct. 2–6. 1–14.

McCartney, J.S. and Murphy, K.D. (2012). "Strain distributions in full-scale energy foundations." *DFI Journal*. 6(2), 28–36.

McCartney, J.S., Rosenberg, J.E., and Sultanova, A. (2010a). "Engineering performance of thermo-active foundation systems." GeoTrends: The Progress of Geological and Geotechnical Engineering in Colorado at the Cusp of a New Decade (GPP 6). C.M. Goss, J.B. Kerrigan, J. Malamo, M.O. McCarron, M.O. and R.L. Wiltshire, eds. 27–42.

McCartney, J.S., LaHaise, D., LaHaise, T., and Rosenberg, J.E. (2010b). "Application of geoexchange experience to geothermal foundations." Art of Foundation Engineering Practice (GSP 198). M. Hussein, W. Camp, and J. Anderson, eds. *ASCE*. pp. 411–422.

McCartney, J.S. and Rosenberg, J.E. (2011). "Impact of heat exchange on side shear in thermo-active foundations." GeoFrontiers 2011 (GSP 211). J. Han and D.E. Alzamora, eds. *ASCE*, Reston VA. 488–498.

Mimouni T. and Laloui L. (2013). "Towards a secure basis for the design of geothermal piles." *Acta Geotechnica*. 9(3), 355–366. doi: 10.1007/s11440-013-0245-4.

Murphy, K.D. (2013). Evaluation of Thermal and Thermo-mechanical Behavior of Full-scale Energy Foundations. MS Thesis. University of Colorado Boulder. 136 pg.

McCartney, J.S. and Murphy, K.D. (2012). "Strain distributions in full-scale energy foundations." *DFI Journal*. 6(2), 28–36.

Murphy, K.D., McCartney, J.S., and Henry, K.S. (2015). "Thermo-mechanical response tests on energy foundations with different heat exchanger configurations." *Acta Geotechnica*. 10(2), 179–195.

Murphy, K.D. and McCartney, J.S. (2014). "Thermal borehole shear device." *ASTM Geotechnical Journal*. 37(6), 1040–1055.

Murphy, K.D. and McCartney, J.S. (2015). "Seasonal response of energy foundations during building operation." *Geotechnical and Geological Engineering*. 33(2), 343–356.

Olgun, C.G., Martin, J.R. Abdelaziz, S.L., Iovino, P.L., Catalbas, F., Elks, C., Fox, C., and Gouvin, P. (2012). "Field testing of energy piles at Virginia Tech." *37th Annual Conference on Deep Foundations*, October 17–19, 2012, Houston, TX. 1–8. (CD-ROM).

Olgun, C.G. and McCartney, J.S. (2014). "Outcomes from the International Workshop on Thermoactive Geotechnical Systems for Near-Surface Geothermal Energy: From research to practice." *The Journal of the Deep Foundations Institute*. 8(2), 58–72.

Olgun, C.G., Ozudogru, T.Y., Abdelaziz, S.L., and Senol, A. (2014a). "Long-term performance of heat exchanger pile groups." *Acta Geotechnica, Special Issue on Thermally Active Geotechnical Systems for Near Surface Geothermal Energy*, doi: 10.1007/s11440-014-0334-z.

Olgun, C.G., Ozudogru, T.Y., and Arson, C.F. (2014b). "Thermo-mechanical radial expansion of heat exchanger piles and possible effects on contact pressures at pile–soil interface." *Géotechnique Letters*. 4(July–September), 170–178.

Ouyang Y., Soga K. and Leung Y.F. (2011). "Numerical back-analysis of energy pile test at Lambeth College, London." GeoFrontiers 2011 (GSP 211). J. Han and D.E. Alzamora, eds. *ASCE*, Reston VA. 440–449.

Ozudogru, T., Brettmann, T., Olgun, G., Martin, J., and Senol, A. (2012). "Thermal conductivity testing of energy piles: Field testing and numerical modeling." *ASCE GeoCongress 2012*, Oakland, CA. March 25–29th. 4436–4445.

Peron, H., Knellwolf, C., and Laloui, L. (2011). "A method for the geotechnical design of heat exchanger piles." GeoFrontiers 2011 (GSP 211). J. Han and D.E. Alzamora, eds. *ASCE*, Reston VA. 470–479.

Plaseied, N. (2012). Load Transfer Analysis of Energy Foundations. MS Thesis. University of Colorado Boulder. 92 pg.

Portland Cement Concrete Pavements (PCCP) Research Team. (2011). Thermal Coefficient of Portland Cement Concrete. FHWA. Washington, DC.

Reese, L.C. and O'Neill, M. (1988). Drilled Shafts. Pub. FHWA-HI-88-042. USDOT.

Skempton, A.W. and MacDonald, D.H. (1956), "Allowable settlement of buildings." *Proc. Institute of Civil Engineers*. London, Part 3, Vol. 5, 727–768.

Stewart, M.A. and McCartney, J.S. (2013). "Centrifuge modeling of energy foundations under cyclic heating and cooling." *ASCE Journal of Geotechnical and Geoenvironmental Engineering*. 1–11. doi: 10.1061/(ASCE)GT.1943-5606.0001061.

Sutman, M., Brettmann, T., and Olgun, C.G., 2014. Thermo-mechanical behavior of energy piles: Full-scale field test verification. *DFI 39th Annual Conference on Deep Foundations*, Atlanta, GA. October 21–24, 2014. 1–11. (CD-ROM).

Uchaipichat, A. and Khalili, N. (2009). "Experimental investigation of thermo-hydro-mechanical behaviour of an unsaturated silt." *Géotechnique*. 59(4), 339–353.

Wang, B., Bouazza, A., and Haberfield, C. (2011). "Preliminary observations from laboratory scale model geothermal pile subjected to thermal-mechanical loading." GeoFrontiers 2011 (GSP 211). J. Han and D.E. Alzamora, eds. *ASCE*, Reston VA. 430–439.

Wang, B., Bouazza, A., Singh, R., Haberfield, C., Barry-Macaulay, D., and Baycan, S. (2014). "Post-temperature effects on shaft capacity of a full-scale geothermal energy pile." *J. Geotech. Geoenviron. Eng.*, 10.1061/(ASCE)GT.1943-5606.0001266, 04014125.

Wang, W., Regueiro, R., and McCartney, J.S. (2015). "Coupled axisymmetric thermo-poro-elasto-plastic finite element analysis of energy foundation centrifuge experiments in partially saturated silt." *Geotechnical and Geological Engineering*. 33(2), 373–388.

2. Thermal analysis of thermoactive foundations

Moncef Krarti, Ph.D., P.E. LEED® AP and
Byung Chang Kwag, M.S., University of Colorado Boulder

Abstract: Thermo-active foundation (TAF) systems offer innovative and sustainable alternatives to ground-source heat pumps and other conventional HVAC systems to heat and cool commercial as well as residential buildings. TAFs have a dual function since they are installed within elements that are already needed for statical, structural, and geotechnical purposes. TAF systems have been reported to be more energy efficient than geothermal borehole ground-source heat pumps (GSHPs) since concrete has higher thermal conductivity than most soil types. In addition, TAFs do not require any land availability which is one of the main challenges for conventional geothermal borehole heat pumps especially those using horizontal heat exchange loops.

In this chapter, an overview of thermal analysis of TAFs is presented including integration of TAF models into detailed whole-building simulation tools. Specifically, the impact of design TAF parameters on both building heating and cooling energy end-uses is evaluated. Moreover, the energy efficiency of TAF systems is compared against conventional air conditioning systems for both commercial and residential buildings.

2.1 Introduction

Renewable energy sources can be utilized not only to generate electricity but also to meet heating and cooling needs for buildings. In particular, through the use of heat exchangers embedded in the ground, heat can to be extracted from or rejected into the soil medium to maintain thermal comfort within buildings without a significant reliance on any other external energy sources and mechanical systems such as boilers and chillers.

Ground source heat pumps or GSHPs are examples of geothermal systems that take advantage of mild and uniform deep ground temperatures to heat and cool both residential and commercial buildings. However, high installation costs can make GSHPs using vertical boreholes less cost-effective compared to other conventional air conditioning

systems. Therefore, alternative systems and methods have been suggested to reduce the implementation costs of GSHP systems. Thermoactive foundation (TAF) systems have been shown to represent a viable solution to reduce the excavation costs related to drilling work associated with deep boreholes of vertical GSHPs. TAF systems, also commonly referred to as energy or thermal piles, integrate ground loop heat exchanger pipes within building concrete foundations to partially or fully heat and cool buildings. Thus, TAF systems utilize building foundation elements (i.e., piles) as vertical boreholes in order to reduce the excavation costs associated with digging work needed for GSHPs. Indeed, a recent research by Lee et al. (2013) showed that a TAF system integrated with a PHC (pre-stressed high-strength concrete) pile can reduce the installation cost of the system by over 40%. Therefore, the installation costs associated with TAF systems can be significantly reduced compared to those of GSHPs with vertical boreholes.

The basic operating principles of GSHPs and TAFs are depicted in Figure 2-1. When compared to GSHPs, TAFs save the excavation costs of boreholes by integrating the heat exchangers within the concrete of the building foundation piles. Table 2-1 compares the basic features of both GSHPs and TAFs. However and unlike the case of GSHPs, no clear design guidelines are available to properly size TAF systems to account for a wide range of parameters such as pile depth, soil type, number of piles, and water table depth.

Indeed, limited analyses and research studies have been reported for assessing the thermal performance and best design specifications of TAF systems especially for US climates and building applications (Laloui, 2006; Hamada et al., 2007; Sekine et al., 2007; Jalaluddin et al., 2010; Wood et al., 2010; Loveridge et al., 2013). Indeed, the vast majority of existing TAF systems has been installed and evaluated in Europe and Japan. In particular, Brandl (2006) overviewed TAF systems and provided a discussion of reported thermal and mechanical performance for select case studies in Europe. Brandl noted that concrete which has good thermal properties can enhance heat transfer between the ground medium and heat exchanger pipes, and that low-permeability soil and low hydraulic gradient of groundwater can improve TAF thermal performance. Recently, McCartney et al. (2010), McCartney and Rosenberg (2011), and Stewart and McCartney (2013) performed a controlled laboratory experimental analysis using a centrifuge set-up

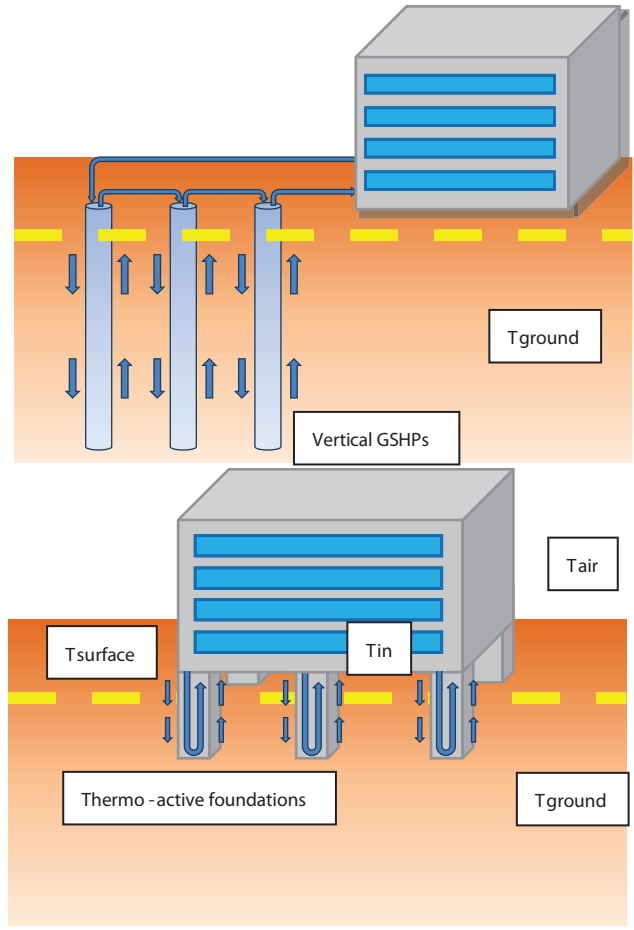

Figure 2-1 Schematic comparison of GSHP and TAF systems.

to evaluate soil-foundation interactions for a small-scale TAF. It was observed that heat can be transferred effectively to the ground medium through a fluid circulating within heat exchanger pipes embedded in a concrete pile. Rouissi et al. (2012), Kwag and Krarti (2013), and Kaltreider et al. (2015) used experimental data of Rosenberg (2010), while Kwag and Krarti (2014) utilized testing results obtained by Stewart and McCartney (2013) to validate their numerical thermal models of TAF systems. While Rouissi et al. (2012) and Kaltreider et al. (2015) developed two-dimensional numerical models, Kwag and Krarti (2014) developed a three dimensional numerical model to assess

Table 2-1 Comparison of basic features between GSHPs and TAFs.

Feature	GSHPs	TAFs
Range of depths	50 ft. to 600 ft. (15 m to 180 m) (ref. ASHRAE std. 32.10)	Various depths depending on building foundations (as shallow as 2–3 m)
Pile Configuration (Cross section)	Circular section	Various based on foundation types Circular section Square section Rectangular section
Effective Design Parameters	Ground temperature Borehole size	Ground temperature Ground surface temperature Foundation size

thermal performance of TAF systems. The reported analyses using numerical solutions indicated that several physical parameters, such as foundation pile depth, flow velocity, and shank space, can have a significant impact on the ground heat transfer rate between an energy pile and the ground medium. Abdelaziz et al. (2011) also found that the same design parameters can have significant effects on the thermal performance of TAF systems.

Moreover, Rouissi et al. (2012) and Kaltreider et al. (2015) found that significant thermal interactions can occur between indoor building environment and TAF system components. Specifically, when compared to the standard foundations (i.e., without embedded heat exchangers), TAF systems can significantly affect ground-coupled building foundation heat transfer and thus can affect both heating and cooling thermal loads for air conditioned buildings. This result indicates that thermal analysis of TAFs differs from that of GSHPs for which no thermal interactions occur between the building and the vertical boreholes.

Currently, several building energy simulation programs employ the thermal response function approach, also called as G-function, to model the thermal performance of GSHPs. The G-function methodology has been initially developed by Eskilson (1987) to evaluate long-term

thermal performance of GSHPs. Yavuzturk et al. (1999) have later extended the G-function approach to account for the short-time performance of GSHPs. Recently, Loveridge (2012) and Kwag and Krarti (2014) have applied the G-function methodology to evaluate the thermal performance of TAFs using whole-building simulation tools.

This chapter includes three sections. The first section provides an overview of existing thermal models for TAFs. The second section introduces the thermal response function or G-function methodology and its application to model the thermal performance of TAF systems. Finally, the third section outlines the integration of TAF models using G-function approach into whole-building simulation analysis tools. Two applications of TAF modeling and simulation analysis are presented and discussed including one case study for small office buildings and one case study for multi-family apartment buildings.

2.2 Thermal modeling of TAFs

2.2.1 Description of TAF thermal modeling

Recently, Kwag and Krarti (2014) have developed a three-dimensional numerical model for a TAF system considering a slab-on-grade floor building foundation as illustrated in Figure 2-2. To model the TAF system, heat exchanger pipes are considered to be embedded into the

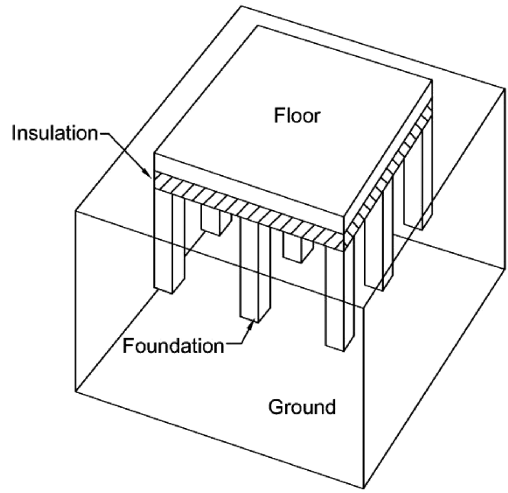

Figure 2-2 Three-dimensional numerical model for a building slab-on-grade foundation with thermal piles.

concrete foundation elements. The ground medium is assumed to be large enough to consider undisturbed ground temperature as a boundary condition. Tables 2-2 through 2-4 provide summaries of geometric and thermal properties of the numerical model. In the numerical model, it is assumed that the ground medium has uniform thermal properties. This assumption is typically common for evaluating thermal performance of GSHP systems and TAF systems as well as foundation heat transfer (Eskilson, 1987; Krarti, 1999; Yavuzturk and Spitler, 1999; Kavanaugh, 2010).

Table 2-2 Typical characteristics of the ground medium and foundation elements considered for TAF thermal modeling.

	Domain	Foundation	Floor
Material	Soil	Concrete	Concrete
Length × Width × Depth (m)	40 × 40 × 20	0.5 × 0.5 × 10	10 × 10 × 0.25
Thermal Conductivity (W/m-K)	1.00	1.73	1.73
Density (kg/m^3)	2240	2600	2600
Specific Heat (J/kg-K)	837	880	880

Table 2-3 Geometric and thermal properties of the U-tube pipes.

Pipe Diameter (m)	0.025
Pipe Depth (m)	9.95
Shank Space (m)	0.300
Space between Foundation to Pipe	0.050
Thermal Conductivity (W/m-K)	0.360

Table 2-4 Thermal properties of the heat exchanger fluid.

Thermal Conductivity (W/m-K)	0.58
Density (kg/m^3)	1000
Specific Heat (J/kg-K)	4181

The numerical solution of the transient three-dimensional heat transfer for the TAF model shown in Figure 2-2 is obtained by Kwag and Krarti (2014) using an implicit finite difference discretization method associated with the Cartesian coordinates using the non-uniform grid of Figure 2-3(a) and the control volume formulation of Figure 2-3(b).

Brandl (2006) noted that the general heat transfer mechanisms in the ground medium involve conduction, radiation, convection, vaporization and condensation processes, ion exchange, and freezing-thawing processes. It is difficult to take all these heat transfer mechanisms into account simultaneously when evaluating thermal performance of geothermal systems such TAFs. Instead, it is common to consider only conduction and convection heat transfer within the ground medium with uniform ground thermal properties as well as within the pipes of the embedded heat exchangers.

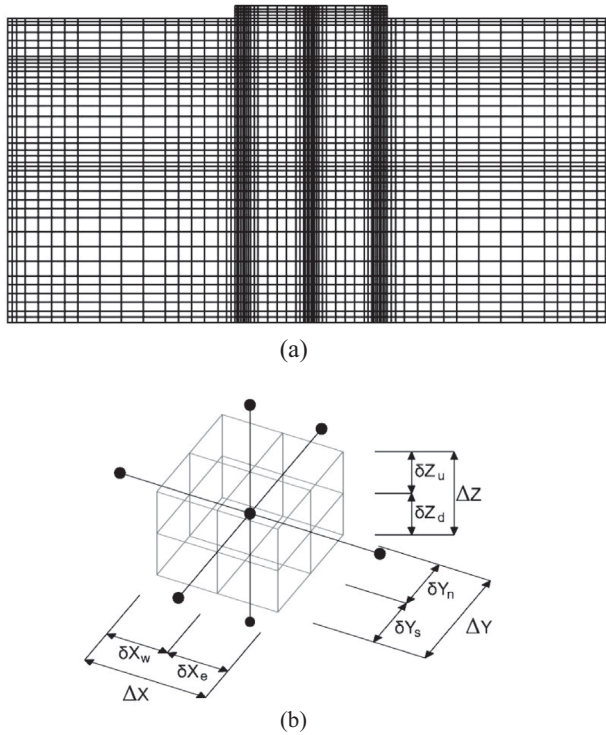

Figure 2-3 (a) Non-uniform grid for the thermo-active foundation medium and (b) the control volume used for one interior node.

Equations (1) and (2) provide a general transient conduction and diffusion heat transfer equations in the Cartesian coordinates, and Figure 2-3 shows a discretization grid scheme used for establishing a numerical solution for Equation (1). Specifically, the solutions of the transient heat conduction and diffusion equations are obtained using implicit finite difference technique as outlined implicitly by Equations (3) through (25).

Within the soil and concrete media:

$$\frac{1}{\alpha}\frac{\partial T}{\partial t}=\frac{\partial^2 T}{\partial x^2}+\frac{\partial^2 T}{\partial y^2}+\frac{\partial^2 T}{\partial z^2} \tag{1}$$

Inside the pipes embedded inside the foundation piles:

$$\rho C_p\frac{\partial T}{\partial t}+\rho C_p\frac{\partial V_x T}{\partial x}+\frac{\partial V_y T}{\partial y}+\frac{\partial V_z T}{\partial z} =k\frac{\partial^2 T}{\partial x^2}+\frac{\partial^2 T}{\partial y^2}+\frac{\partial^2 T}{\partial z^2} \tag{2}$$

The discretisation of both Equation (1) is outlined:

$$a_P=a_E+a_W+a_N+a_S+a_U+a_D+a_P^0$$

$$a_{E,W}=\frac{k_{e,w}\Delta y\Delta z}{\delta x_{e,w}} \tag{3}$$

$$a_{N,S}=\frac{k_{n,s}\Delta x\Delta z}{\delta x_{n,s}} \tag{4}$$

$$a_{U,D}=\frac{k_{u,d}\Delta x\Delta y}{(\delta z)_{u,d}} \tag{5}$$

$$a_P^0=\frac{(\rho c)_p\Delta V}{\Delta t} \tag{6}$$

$$b=S_c\Delta V+a_P^0T_P^0 \tag{7}$$

While heat transfer occurring within the ground medium is mainly through conduction as noted by Equation (1), the heat transfer mechanisms

dominating for the fluid circulating within the geothermal pipes are convection and diffusion as indicated by Equation (2). Equations (8) through (25) describe the discretization schemes for the diffusion equation of Equation (2).

$$a_P T_P = a_E T_E + a_W T_W + a_N T_N + a_S T_S + a_U T_U + a_D T_D + b \quad (8)$$

$$a_P = a_E + a_W + a_N + a_S + a_U + a_D + a_P^0 \quad (9)$$

where

$$a_{W.E.S.N.U.D} = D_{W.E.S.N.U.D} * (APe_{W.E.S.N.U.D}) + \max(F_{W.E.S.N.U.D,}\ 0) \quad (10)$$

$$a_P^0 = \frac{\rho_{fluid} * Cp_{fluid} * \Delta V}{dy} \quad (11)$$

$$\Delta V = \Delta x * \Delta y * \Delta z \quad (12)$$

$$b = a_P^0 * T_P^0 \quad (13)$$

With the conductance terms defined as follows:

$$(West, East) \cdots D_{W,E} = k_{fluid} * \frac{\Delta y * \Delta z}{\delta x_{w,e}} \quad (14)$$

$$(North, South) \cdot D_{N,S} = k_{fluid} * \frac{\Delta x * \Delta z}{\delta y_{n,s}} \quad (15)$$

$$(Up, Down) \cdots D_{U,D} = k_{fluid} * \frac{\Delta x * \Delta y}{\delta z_{u,d}} \quad (16)$$

While the flow rate terms are expressed as follows:

$$F_{W,E} = \rho_{fluid} * Cp_{fluid} * U_{W,E} * \Delta y * \Delta z \quad (17)$$

$$F_{N,S} = \rho_{fluid} * Cp_{fluid} * U_{N,S} * \Delta x * \Delta z \quad (18)$$

$$F_{U,D} = \rho_{fluid} * Cp_{fluid} * U_{U,D} * \Delta x * \Delta y \quad (19)$$

The Peclet Number terms are defined:

$$Pe_{W,E} = F_{W,E}/D_{W,E} \tag{20}$$

$$Pe_{N,S} = F_{N,S}/D_{N,S} \tag{21}$$

$$Pe_{U,D} = F_{U,D}/D_{U,D} \tag{22}$$

The A(|Pe|) function is defined using the Power Law Scheme:

$$APe_{W,E} = \max(0,(1 - 0.1 * |Pe_{W,E}|^5)) \tag{23}$$

$$APe_{N,S} = \max(0,(1 - 0.1 * |Pe_{N,S}|^5)) \tag{24}$$

$$APe_{U,D} = \max(0,(1 - 0.1 * |Pe_{U,D}|^5)) \tag{25}$$

As described in Figures 2-2 and 2-4, the numerical model of a TAF system includes several components: ground domain, foundation element (foundation piles and slab-on-grade floor), and heat exchangers made up of refrigerant flowing in pipes embedded in foundation piles. Thus, the boundary conditions of the numerical model are associated with the temperature and heat flux variations along surfaces of these

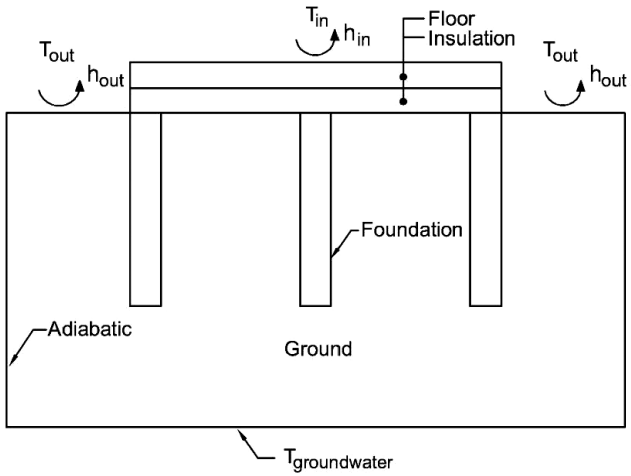

Figure 2-4 Boundary conditions considered for the TAF numerical model (Kwag and Krarti, 2014).

elements. Equation (26) provides the general expression for all three types of boundary conditions used in the TAF model. As illustrated in Figure 2-4, the bottom boundary condition of the TAF model is constant prescribed groundwater temperature (type 1). The top slab and ground surface boundary conditions are indoor and outdoor air temperatures (type 3). The outer edge boundary conditions are set to be adiabatic surfaces (type 2) which implies undisturbed ground temperatures along the ground medium surfaces.

$$\alpha T + \beta \frac{\Delta T}{\Delta r} = C \tag{26}$$

Type 1: $\alpha = 1, \beta = 0, C =$ Constant Temperature

Type 2: $\alpha = 1, \beta = 0, C =$ Constant Heat Flux

Type 3: $\alpha \neq 1, \beta \neq 0$

Figure 2-5 illustrates the discretization grid size on both the accuracy (expressed in terms of RMSE relative to a reference grid size of 500,000 nodes) and the computational efforts (expressed in CPU time) required to obtain the implicit finite difference solution. As expected, when the

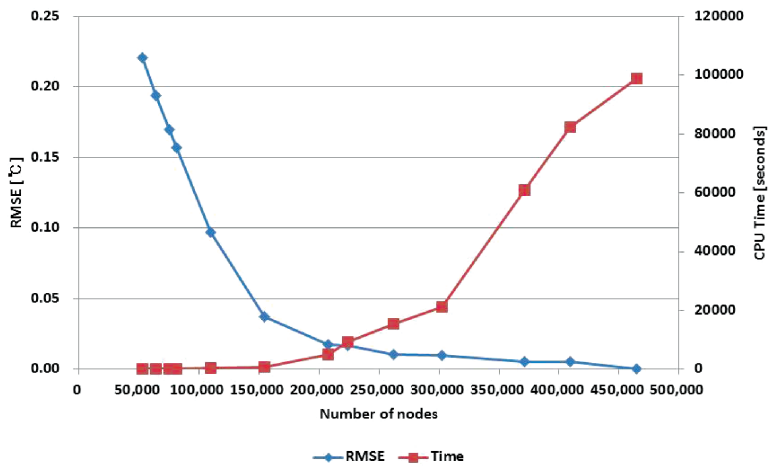

Figure 2-5 Variation of CPU time and RMSE value for the TAF numerical solution as function of the grid size.

grid size increases, the numerical solution accuracy improves but the computational CPU time increases. As a compromise and based on the results of Figure 2-5, an adequate number of nodes for the discretization grid can be selected.

2.2.2 Experimental validation

Most reported models for TAFs have been validated using controlled experimental analysis. In particular, a small-scale TAF system has been tested under laboratory conditions. In particular, Rosenburg (2010) carried out an experimental study of a small scale thermal pile to better understand the effects of temperature fluctuations on the structural capacity of thermo-active foundations under representative building loads. The tested thermal pile was a cylindrical concrete pier with aluminum tubing to represent the heat exchange tubes in a thermo-active foundation. Silicon fluid was pumped through the tubes in a closed loop while being heated or cooled by a heat pump. The pier was embedded in soil inside an insulated cylindrical container designed for use with a centrifuge. The distribution in temperature within the soil layer was measured using three temperature profile probes. These probes consist of a steel rod with 6 RTD thermocouples spaced evenly at 45 mm from the bottom. Three RTD thermocouple probes were embedded within the soil to a depth of 270 mm below the soil surface. Figure 2-6 gives the dimensions of the small-scale thermal pile and the schematics of the experiment set-up. Several tests were performed in which the foundation and surrounding soil were slowly heated and/or cooled while the pier was loaded with a simulated building load. At the start of each test, the entire apparatus began at ambient room temperature. Once the soil and foundation had fully settled from the force imposed by the centrifuge, the fluid began to be pumped through the tubing with the heat pump on in heating mode. Inlet fluid temperatures, along with the outlet temperatures and the soil depth temperatures, were measured and logged every 6 seconds for the duration of each test.

The measurements obtained from the small-scale experimental set-up of Figure 2-6 are utilized to validate recently developed numerical solutions to TAF thermal models predictions. Table 2-5 lists the input values for the baseline model of the experimental thermo-active foundation used for the calibration analysis of the 3-D numerical solution developed by Kwag and Krarti (2015). After calibration based on uncertainties in the

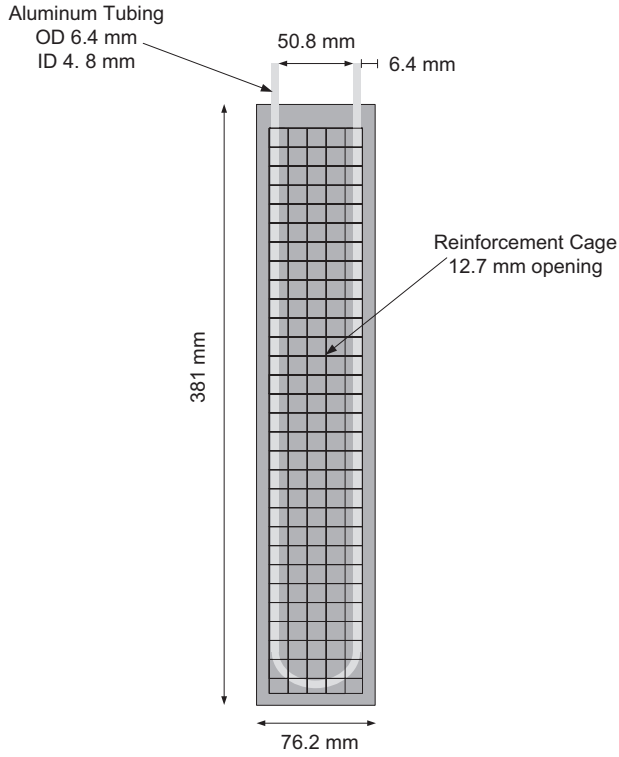

(a) Dimensions of the tested small scale thermal pile

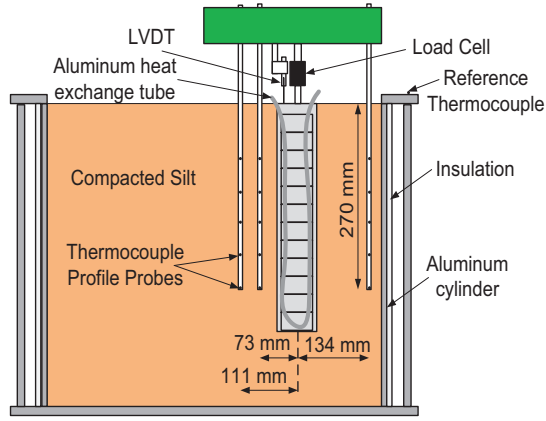

(b) Experimental Set-Up

Figure 2-6 Test set-up used for the Experimental Analysis of TAF System Thermal Performance.

Table 2-5 Model parameters used for simulation of physical experiment.

Parameter	Value	Units	Source/Reference
Thermal Conductivity of Soil	1.43	W/m-K	Experimental Measurement (Rosenberg, 2010; McCartney and Rosenberg, 2011)
Specific Heat of Soil	1480	J/kg-K	Assumed based on Soil Type
Density of Soil	1765	kg/m^3	Experimental Measurement (Rosenberg, 2010)
Thermal Conductivity of Concrete	1.00	W/m-K	Experimental Measurement (Rosenberg, 2010; McCartney and Rosenberg, 2011)
Specific Heat of Concrete	900	J/kg-K	ASHRAE Fundamentals (ASHRAE, 2013)
Density of Concrete	2080	kg/m^3	ASHRAE Fundamentals (ASHRAE, 2013)
Thermal Conductivity of Silicon Fluid	22	W/m-K	Manufacturer Specifications (Kaltreider, 2011)
Specific Heat of Silicon Fluid	1370	J/kg-K	Manufacturer Specifications (Kaltreider, 2011)
Density of Silicon Fluid	920	kg/m^3	Manufacturer Specifications (Kaltreider, 2011)
Kinematic Viscosity of Fluid	0.00002	m^2/s	Fluid Supplier (Kaltreider, 2011)

(Continued)

Table 2-5 Model parameters used for simulation of physical experiment.

Parameter	Value	Units	Source/Reference
Fluid Velocity	11.05	m/s	Experimental Average (Rosenberg, 2010; McCartney and Rosenberg, 2011)
Thermal Conductivity of Aluminum Tube	237	W/m-K	Cengel et al., 2008
Tube Wall Thickness	0.0016	m	Experimental Measurement (Rosenberg, 2010; McCartney and Rosenberg, 2011)
Tube Diameter	0.0048	m	Experimental Measurement (Rosenberg, 2010; McCartney and Rosenberg, 2011)
Exterior Air Convection Coefficient	71.03	W/m^2-K	Calculated based on Specifications of the Experiment (Kaltreider, 2011)

soil and concrete properties as well as the initial state of the soil domain, the 3-dimensional model produced results matching the experiment to within an RMSE of 0.5°C at each time stamp. Table 2-6 compares the values of the input parameters set for the baseline and calibrated models. Figure 2-7 directly compares the calibrated simulation results with the experimental data at each time stamp. Table 2-7 gives the RMSE values for each of time period used in the validation. As indicated in Figure 2-7 and Table 2-7, good agreement was obtained between the model predictions and the experimental results for various time periods and temperature probe locations.

Table 2-6 Calibration adjustments made to the numerical model.

Adjusted Parameter	Base Model Value	Calibrated Model Value
Thermal Soil Conductivity	1.43 W/m-K	1.80 W/m-K
Thermal Concrete Conductivity	1.00 W/m-K	1.50 W/m-K
Initial Soil Temperature	15°C	16°C

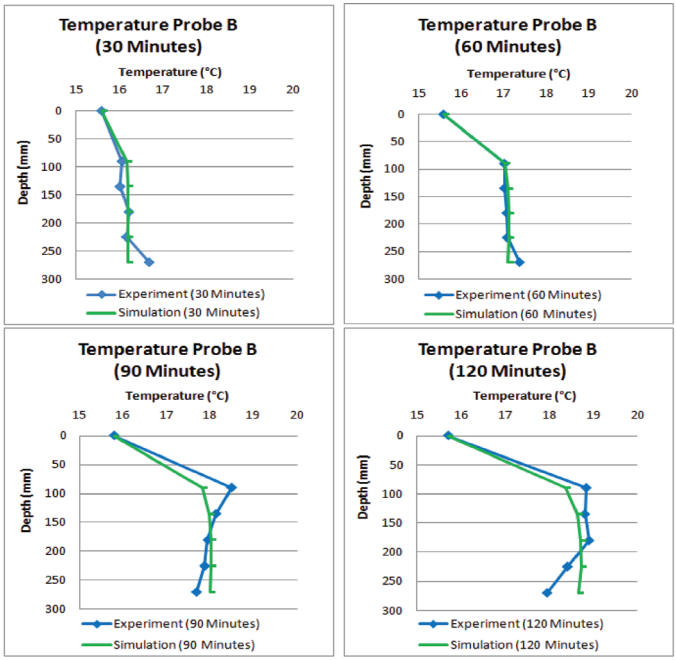

Figure 2-7 Comparison of Experimental Measurements and Simulated Predictions.

Table 2-7 Comparison of validation results for various time periods.

	RMSE (°C)			
Time	30 Min	60 Min	90 Min	120 Min
3D Base Model	1.16	1.38	1.55	1.54
3D Calibrated Model	0.24	0.12	0.35	0.42

2.2.3 Sensitivity analysis

Generally, there is a wide range of factors that affect the thermal performance of TAF systems, including soil type, pile depth, fluid rate, number of heat exchanger loops, soil surface cover, and groundwater level. Results from sensitivity analyses have been carried out and reported to evaluate the impacts of several selected design and operational parameters on the thermal performance of TAF systems (Rouissi et al., 2011; Kaltreider et al., 2015; Kwag and Krarti, 2015). In particular, Kwag and Krarti (2015) performed a sensitivity analysis to evaluate the impact of five design and operational parameters, including thermal properties of ground (k_{soil}) and foundation material (k_{conc}), foundation depth (H), fluid flow rate (V) within the heat exchanger pipes, concrete pile diameter (D = 2r), and the distance (S) between U-tube pipes -also referred to as shank space, on the thermal performance of TAF systems. Kwag and Krarti (2015) have evaluated the impact of these TAF design parameters on both (i) the heat flux transferred between fluid and the ground medium and (ii) the heat flux transferred from the soil to the building through the slab-on-grade floor.

The heat flux between U-tube and the ground is calculated using both inlet and outlet temperatures as indicated by Equations (27) and (28). In addition, to estimate the heat transfer rates through the slab-on-grade floor, the average floor top surface temperatures and the average floor bottom surface temperatures are used as defined by Figure 2-8. Then, Equation (29) is used to compute the floor heat transfer rates.

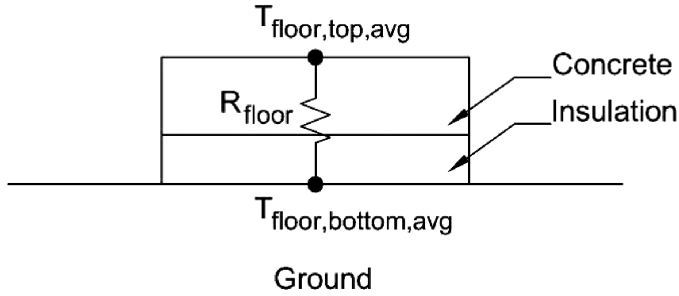

Figure 2-8 The scheme of the floor heat transfer (Kwag and Krarti, 2014).

$$Q = \rho_{fluid} * cp_{fluid} * V * (T_{outlet} - T_{inlet}) \quad (27)$$

$$\text{Percent increase in heart transfer} = \frac{(Q - Q_{base})}{Q_{base}} \times 100\% \quad (28)$$

$$q_{floor}\left[\frac{W}{m^2}\right] = \frac{\Delta T}{R_{floor}} = \frac{T_{floor,\,top,\,avg} - T_{floor,\,bottom,\,avg}}{R_{floor}} \quad (29)$$

Where, R_{floor} is the R value of the slab on grade floor including the concrete slab and any insulation layer.

From the reported sensitivity analyses (Kaltreider, 2011; Rouissi et al., 2011; Kwag and Krarti, 2014), the impact of five parameters (k_{soil}, k_{conc}, H, U, and S) can be summarized as shown in Figure 2-9:

- As the foundation pile length increase, more heat flux can be transferred between heat exchanger pipes and ground medium by the TAF system [Figure 2-9(a-1)].
- More heat is transferred as the fluid velocity with the embedded heat exchanger pipes increases. However, there is a sudden increase in heat transfer observed when the fluid flow shifted from laminar to turbulent regime [Figure 2-9(b-1)].
- Heat transfer through the heat exchanger pipes increases as the pile diameter and shank space increases. Higher pile diameter and shank space may imply less thermal interactions between the U-tube pipes [Figure 2-9(c-1)].
- Higher thermal conductivity for soil and/or concrete increases the heat transfer rate between the heat exchanger pipes and the ground medium [Figure 2-9(d-1)].
- Higher thermal conductivity of soil and concrete as well as deeper foundation piles increase heat transfer through slab-on-grade floor [Figures 2-9(c-2) and (d-2)]. It is noted, however, that the other parameters (i.e., fluid velocity, pile diameter, and shank space) do not have a significant impact on the floor heat transfer [Figures 2-9(a-2) and (b-2)].

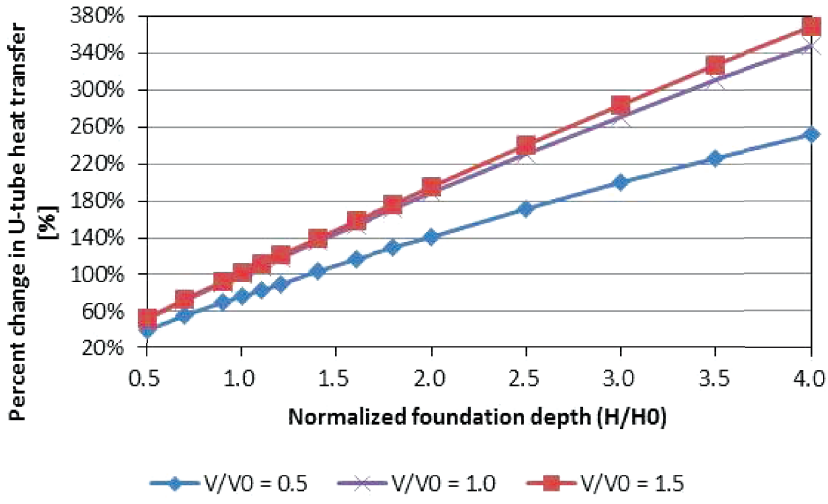

(H_0 = 10 m; V_0 = 6.892E-5 m^3/s)
(a-1) Pipe heat transfer

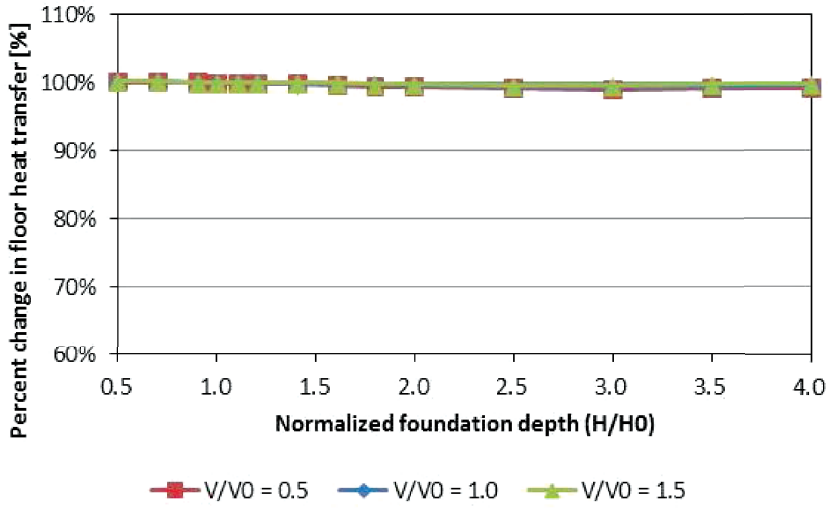

(H_0 = 10 m; V_0 = 6.892E-5 m^3/s)
(a-2) Floor heat transfer

Figure 2-9 Impact on thermal performance of TAF associated with variation in (a) foundation depth. *(Continued)*

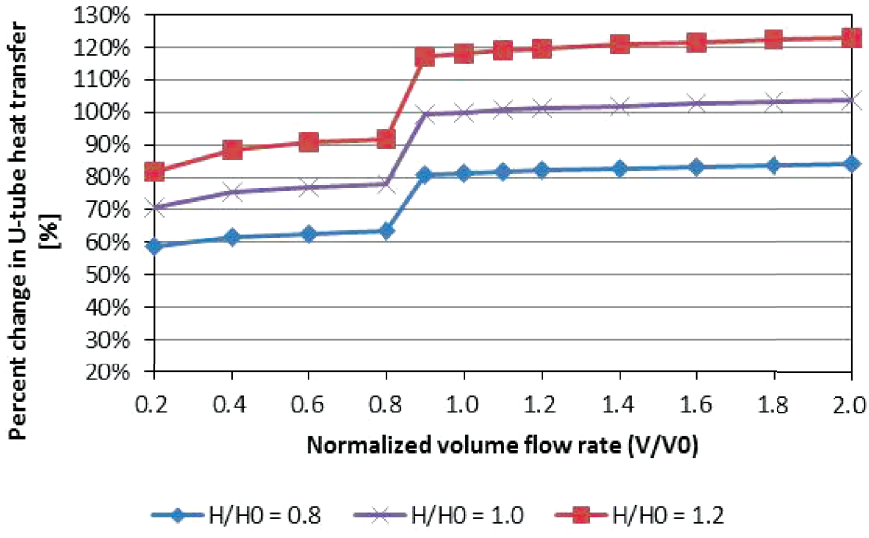

(H_0 = 10 m; V_0 = 6.892E-5 m^3/s)
(b-1) Pipe heat transfer

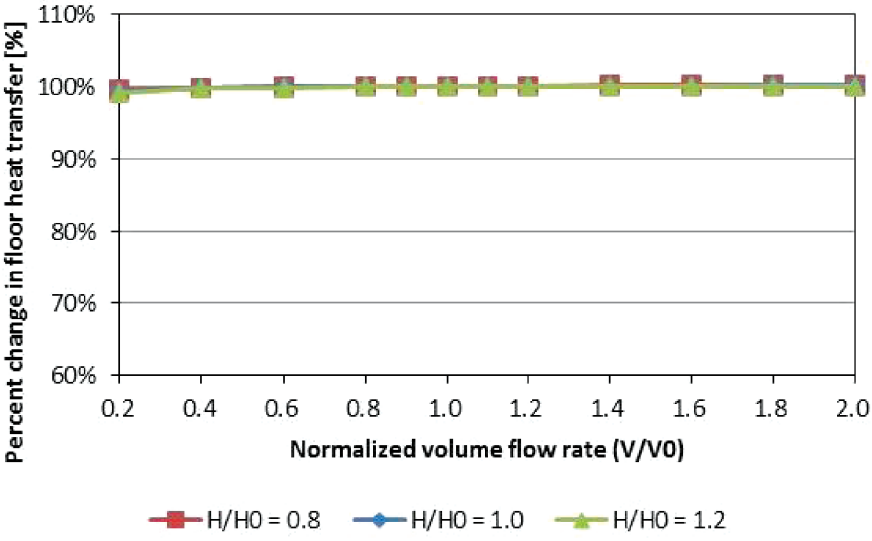

(H_0 = 10 m; V_0 = 6.892E-5 m^3/s)
(b-2) Floor heat transfer

Figure 2-9 Impact on thermal performance of TAF associated with variation in (b) fluid flow rate. *(Continued)*

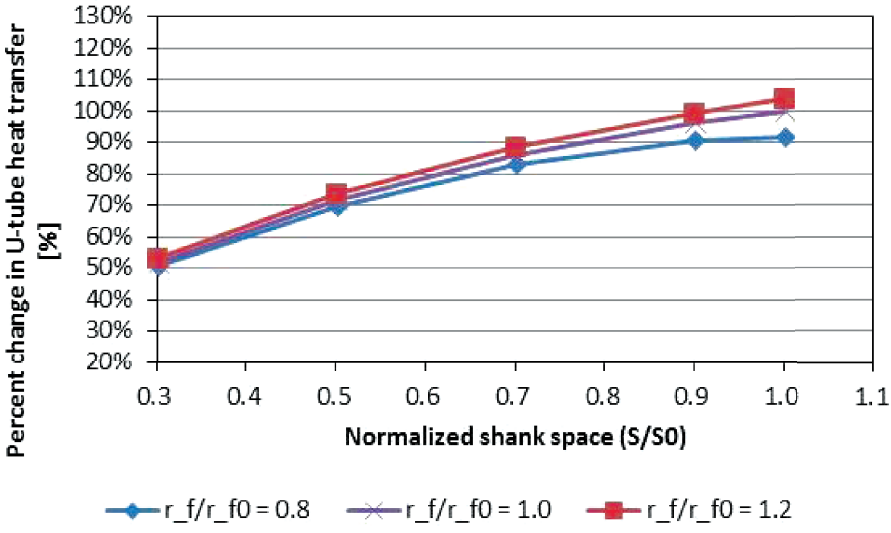

(S_0 = 0.117 m/s; r_f = 0.5 m)
(c-1) Pipe heat transfer

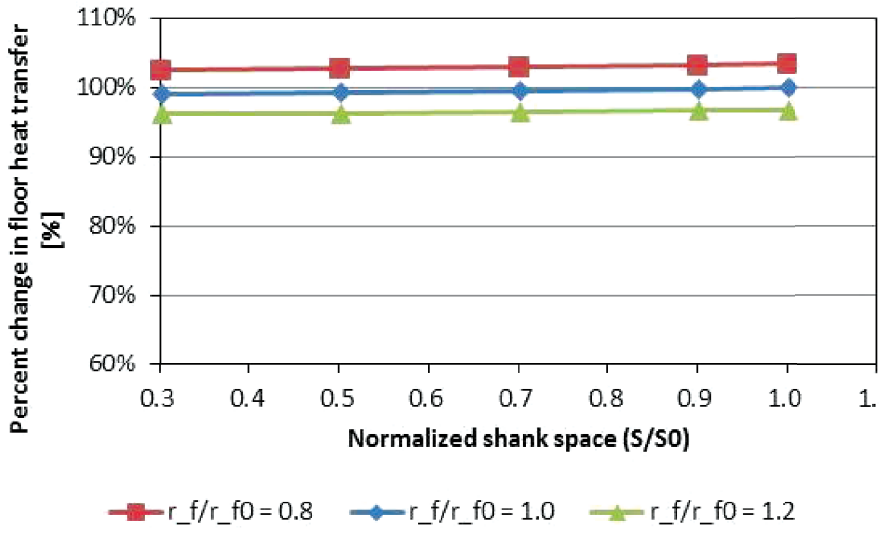

(S_0 = 0.117 m/s; r_f = 0.5 m)
(c-2) Floor heat transfer

Figure 2-9 Impact on thermal performance of TAF associated with variation in (c) shank space. *(Continued)*

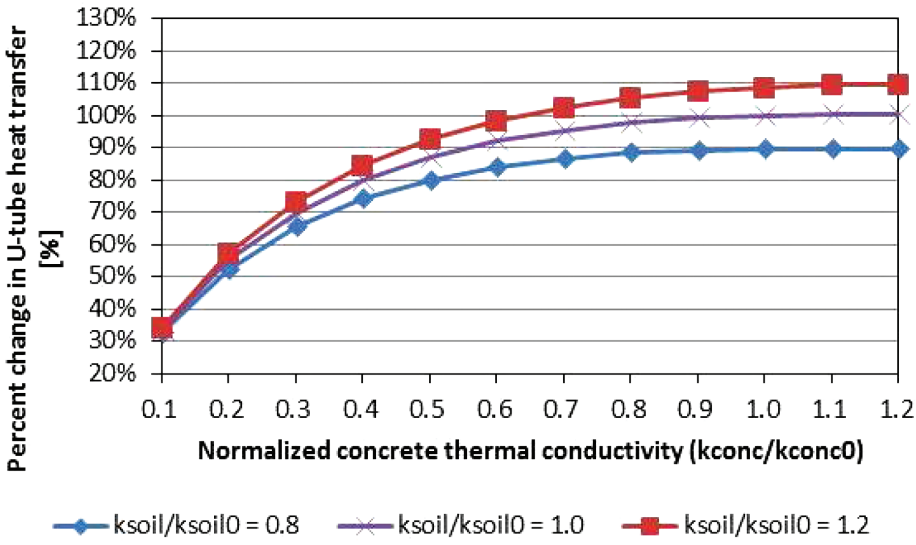

(k_{soil0} = 1.3 W/mK, k_{conc0} = 1.8 W/mK)
(d-1) Pipe heat transfer

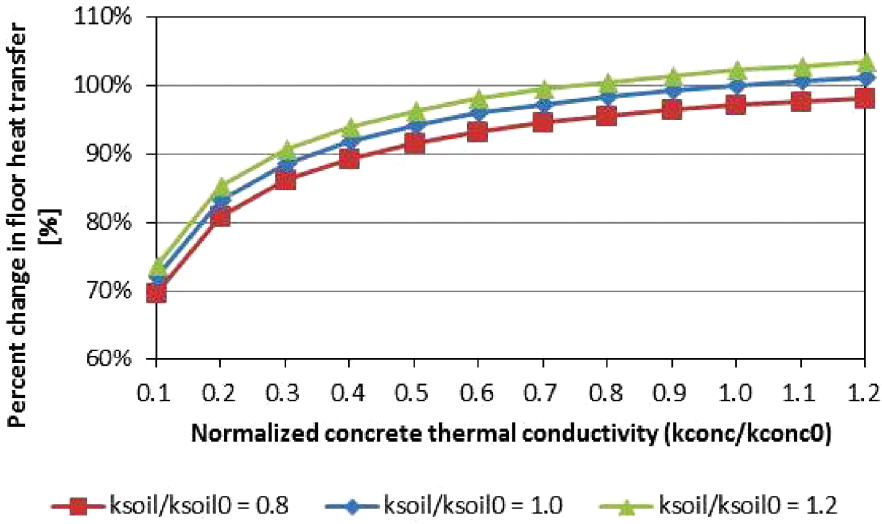

(k_{soil0} = 1.3 W/mK, k_{conc0} = 1.8 W/mK)
(d-2) Floor heat transfer

Figure 2-9 Impact on thermal performance of TAF associated with variation in (d) thermal conductivity.

2.2.4 Impact of thermal piles on soil temperature distribution

Figure 2-10 illustrates soil temperature distribution within the ground medium with and without embedded heat exchanger pipes when the slab-on grade floor is uninsulated and when the average outdoor air temperature is T_o = 21°C = 294K (Hernandez-Guerrero and Krarti, 2014). The heat exchanger inlet fluid temperature is 28°C (301K) while the

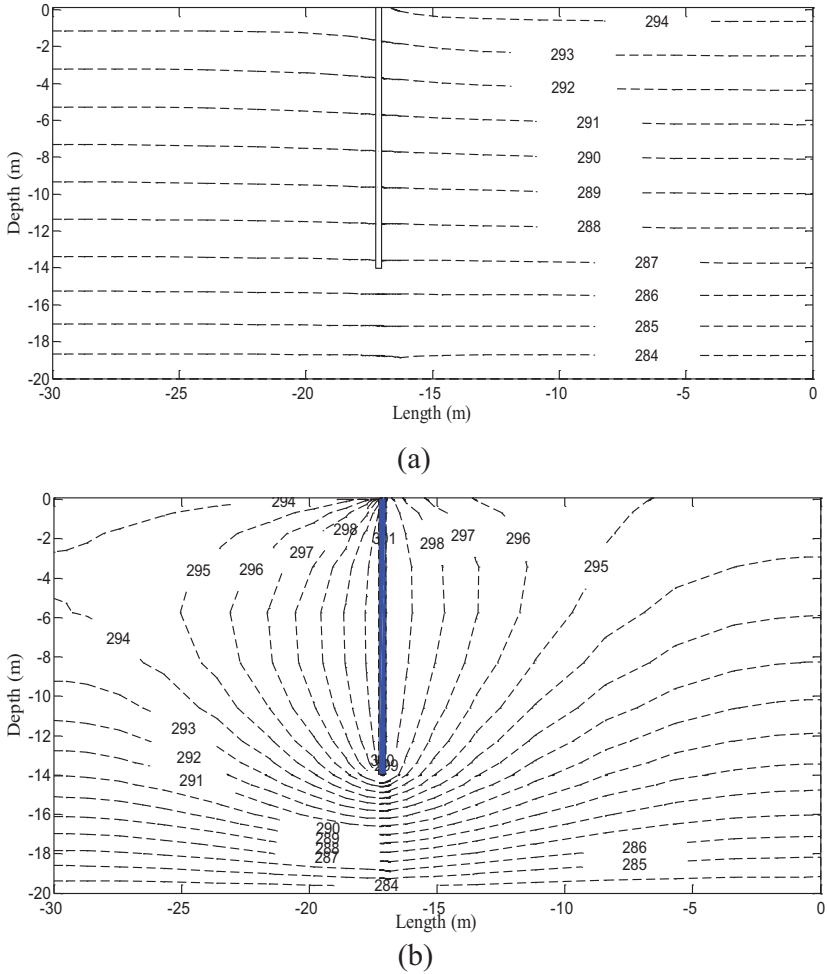

Figure 2-10 Soil temperature isotherms for (a) uninsulated conventional slab foundation—without any geothermal heat exchangers and (b) uninsulated thermo-active foundation (T_o = 21°C = 294K, V = 0.01 m/s).

fluid velocity is set to V = 0.01 m/s. As indicated by the temperature isotherms, the impact of the embedded heat exchanger tubes is significant on the soil temperature field and consequently on the slab foundation heat loss/gain. Indeed, the slab temperature is almost constant in the case of the standard foundation with no thermal piles with the heat is always being lost from the slab surface to mostly deep ground. In the other hand, the presence of thermal piles results in a significant temperature variation along the slab surface changing from 21.5°C (294.5K) from the middle part to about 27°C (300K) in the slab edges. As shown in Figure 2-10, the slab surface can be divided into sections: the middle section which looses heat to the deep ground and the edge section which gains heat from the thermal pile. The thermal interactions between the heat exchanger pile and the foundation slab surface are evaluated in more details in the following sections outlining the impact of three parameters: (i) R-value of a uniform thermal insulation placed along the slab surface, (ii) the length of partial insulation placed around the perimeter of the slab surface, and (iii) the velocity of the heat exchanger fluid circulating the thermal piles.

However, in building applications several foundation piles are typically used for structural reasons as illustrated in Figure 2-11. In particular, the dimensions of the piles, uniformly distributed along the half slab foundation, are shown.

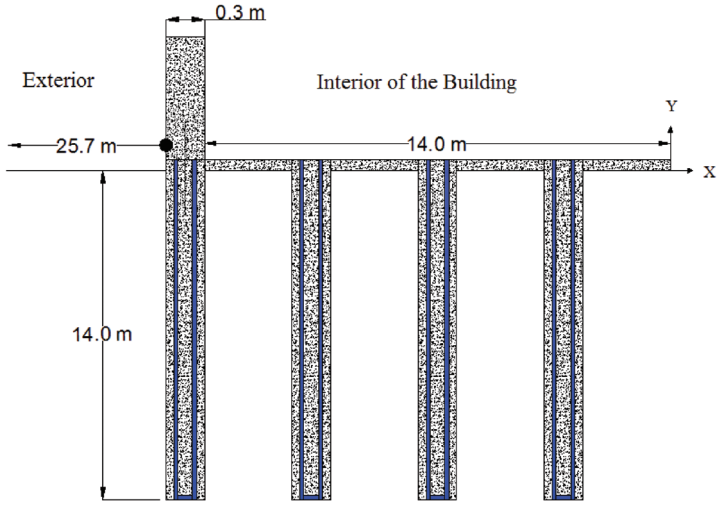

Figure 2-11 Features of thermo active foundation model with multiple piles.

Using steady state analysis of TAF thermal performance, average soil temperature field is determined when the indoor temperature is 22°C (295K), outdoor temperature of 21°C (294K), and inlet water temperature of 29°C (302K). Figure 2-12 compares soil temperature field for a building foundation with one, two, three, and four thermal piles.

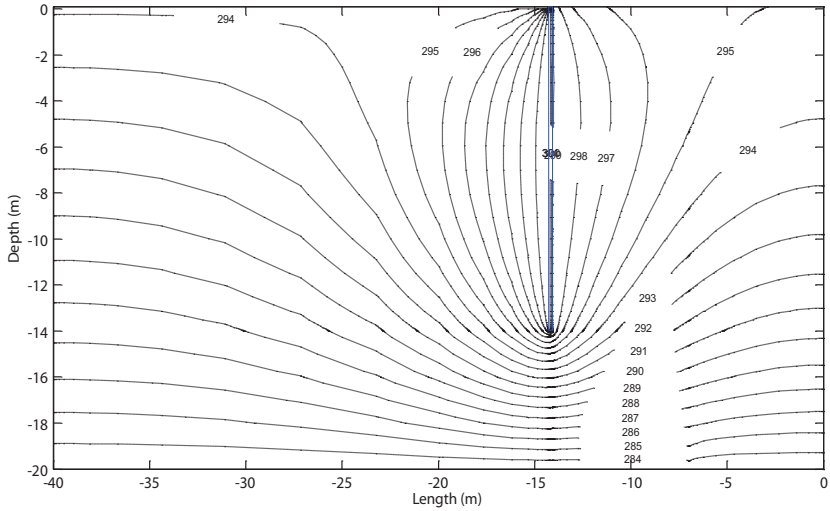

(a) One pile

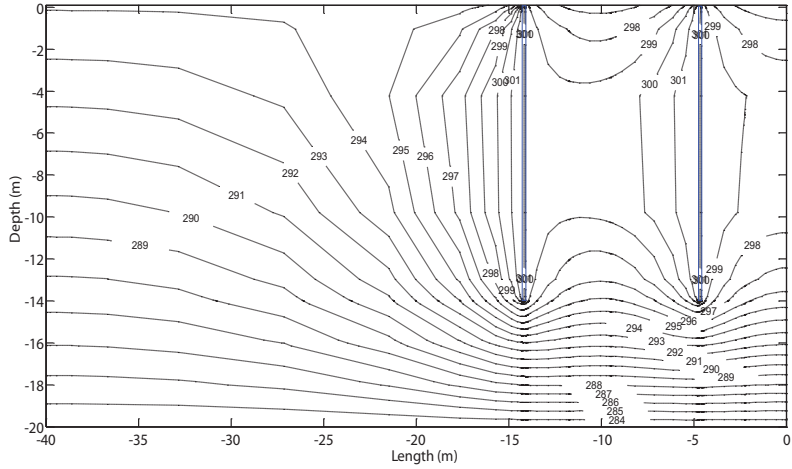

(b) Two piles

Figure 2-12 Soil steady-state temperature field beneath a TAF building foundation. (a) One pile and (b) two piles. *(Continued)*

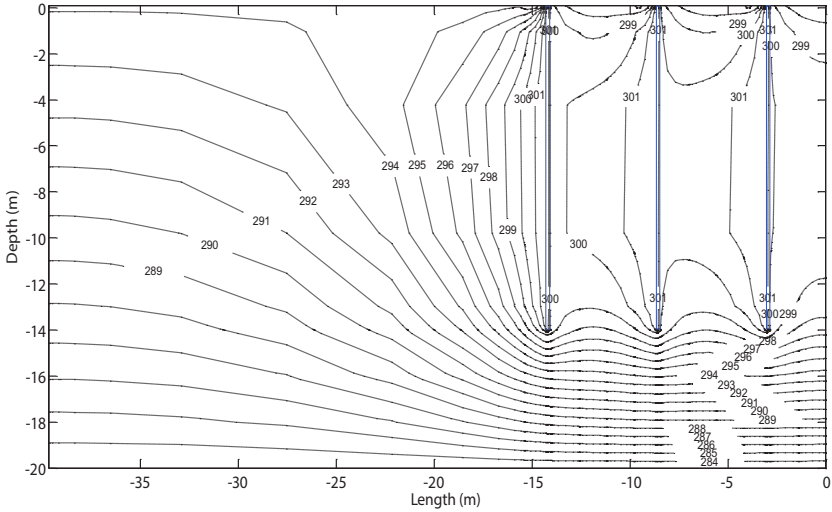

(c) Three piles

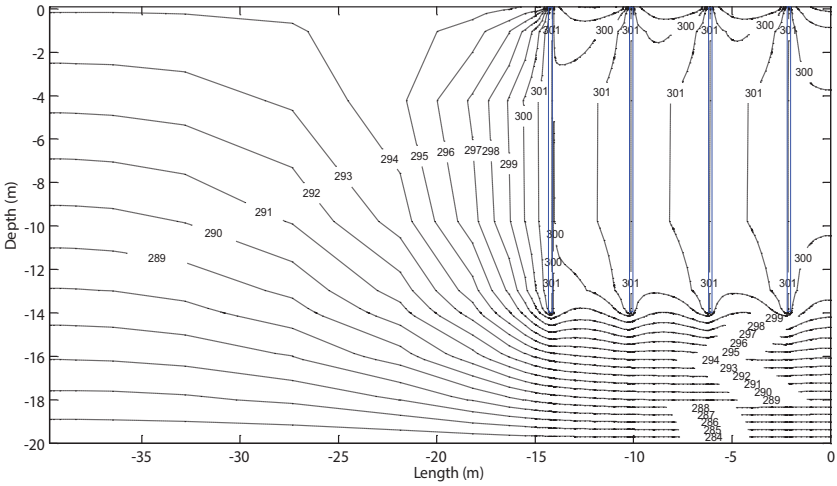

(d) Four piles

Figure 2-12 Soil steady-state temperature field beneath a TAF building foundation. (c) Three piles and (d) four piles.

2.3 Building foundation heat transfer

The addition of heat exchangers in the foundation piles (i.e., TAFs) can significantly affect building foundation heat transfer. In particular, foundation ground coupled heat transfer occurs mostly only at the joints between slab floor and foundation piles and thus can vary significantly

depending on the heat exchanger operating mode. Limited detailed analysis is reported in the literature on the magnitude of the thermal interactions between the building foundations and thermal piles especially under dynamic operation conditions. Recently, Hernandez-Guerrero and Krarti (2014) has developed an analysis method to help architects and engineers in the early design phase to assess the impact of the thermal piles on the thermal heating and cooling loads associated to the building foundations. The analysis method is based on a comprehensive parametric sensitivity analysis to assess the impact of various TAF design specifications of the building foundation heat transfer. The method introduces a new parameter, NTHB, defined to normalize the thermal effect of the thermo-active foundation relative to the baseline case with no thermal piles (i.e., no heat exchanger loops in the foundation piles):

$$\text{NTHB} = \frac{Q_{HE}}{Q_{NHE}} \tag{30}$$

where:

- NTHB: Normalized total heat relative to the baseline case
- Q_{HE}: Total heat flux through the slab when thermal pile is considered.
- Q_{NHE}: Total heat flux through the slab when thermal pile is not installed.

Thus, NTHB provides an adjustment factor that should be applied to a conventional building foundation heat transfer in order to account for the presence of thermal piles. Several parameters can affect the adjustment factor, NTHB. Figure 2-13 shows the variation of NTHB with R-value and length of partial horizontal slab-floor foundation thermal insulation. NTHB value is reduced as the insulation length and the R-value are increased. The results of Figure 2-13 indicate that the impact of thermal piles on foundation heat transfer is more significant when the slab is well insulated. Moreover and as noted in Figure 2-12, the installation of thermal piles can change the building foundation heat transfer by up to 20% relative to the conventional building foundations.

(V = 0.025 m/s, Slab Width =16.913 m).

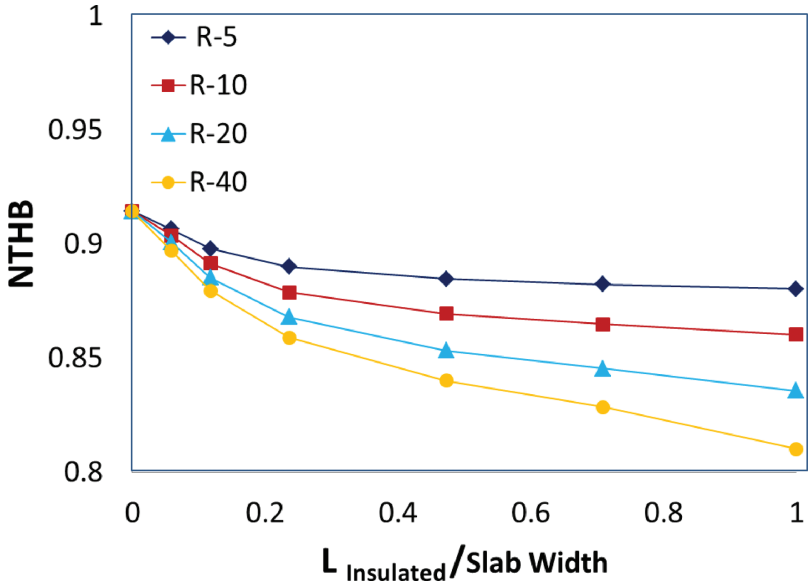

Figure 2-13 NTHB variation with length and R-value of partial horizontal slab insulation.

In order to estimate the annual average NTHB value, a simplified method was proposed by Hernandez-Guerrero and Krarti (2014) to estimate for the heat transfer from thermo-active foundation accounting for several design parameters that affect the thermal interactions between thermal piles and building foundations including:

1. Foundation pile depth, D
2. Slab width, W
3. Horizontal Insulation length, L_{ins}
4. Thermal Resistance R-value, R
5. Thermal conductivity of the concrete, k_{conc}

The ranges of values considered for each parameter are summarized in Table 2-8.

To normalize the various parameters, following dimensionless factors are defined:

$$P_1 = \frac{L_{ins}}{D} \tag{31}$$

Table 2-8 Range of parameters values used to develop a simplified analysis method.

Parameter	Magnitude
Foundation depth (m)	8, 14, 26, 44, 68, 98
Slab width (m)	4, 6, 8, 10, 12, 14, 16.913, 20, 22
Insulation length (m)	0, 1, 2, 4, 6, 8, 10, 12, 14, 16.913, 20, 22
Resistance value (m^2-K/W)	R-5, R-10, R-20, R-30, R-40
Thermal conductivity of the concrete (W/m-K)	1.56. 1.76. 1.96

$$P_2 = \frac{W}{D} \tag{32}$$

$$P_3 = \frac{kR}{D} \tag{33}$$

Using non-linear regression analysis, a closed form expression to estimate NTHB for the dimensionless factors was developed using the following expression (Hernandez-Guerrero and Krarti, 2014):

$$NTHB = \frac{\left[0.8 + P_2\right]^{A_1}}{A_2 \left(P_1\right)^{A_3} + \left[P_3^{A_4} P_2^{A_5} \right]^{P_1+1}} \tag{34}$$

Where A_1, A_2, A_3, A_4, and A_5 are defined in Table 2-9 and P_1, P_2, and P_3 are defined by Equations (31) through (33), respectively. Figure 2-14 shows the scatter diagram where the numerical data are compared with the predictions obtained from Equation (19). The correlation has a

Table 2-9 Simplified analysis correlation coefficients of Equation (34).

Parameter	Value
A_1	–.202
A_2	.181
A_3	.747
A_4	.031
A_5	–.161

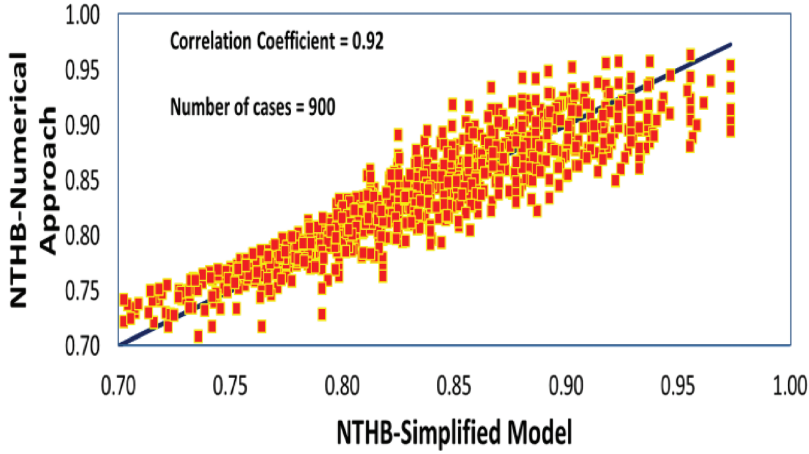

Figure 2-14 Scatter Diagram comparing NTHB values obtained by using the nonlinear correlation of Equation (34) and those obtained by using the numerical solution.

correlation of variance coefficient of $R^2 = 0.92$. The correlation equation of Equation (34) is easy to use to assess the impact on the building thermal loads due to the implementation of thermal piles relative to the conventional slab-on-grade foundations. An example is provided in the following section to illustrate the application of the simplified analysis method of Equation (34). It should be noted again that the simplified analysis is intended to be a preliminary analysis tool to assess the impact of thermal piles on building foundation heat transfer. Equation (34) is applicable when the specifications for the building, pile, and soil medium are within the values listed in Table 2-8.

Example of application of simplified analysis method: The impact of thermal piles is to be estimated on annual foundation total heat transfer for an office building located in Boulder, Colorado. The office building has a TAF system with a slab half width of W = 16 m and a pile depth of D = 16 m. The slab is insulated with 5-cm (2-in) of extruded polystyrene ($R = 1.7611\ m^2 \cdot K/W$) placed horizontally along the slab along a distance of $L_{ins} = 4$ m from the foundation pile. The concrete thermal conductivity is $k_{conc} = 1.8\ W/m \cdot K$ and the indoor temperature is $T = 22^oC$ (295K).

Figure 2-15 illustrates the thermo-active foundation and associated geometric dimensions as described by the problem statement.

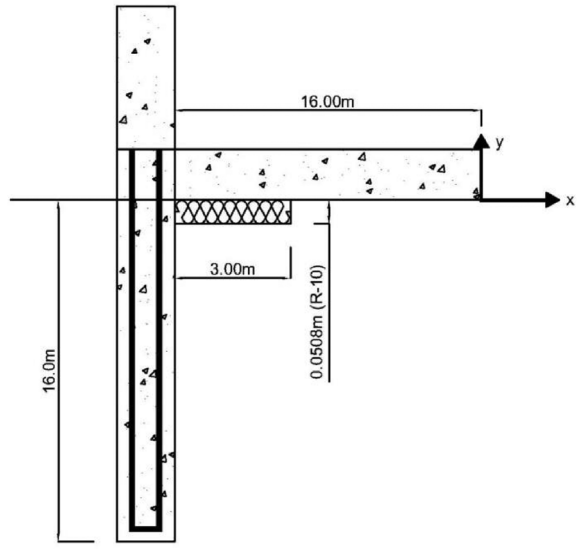

Figure 2-15 Geometric dimensions of the thermo-active foundation for the example case.

Using the simplified analysis method formulated by the correlation of Equation (34), the dimensionless factors, P_1, P_2, and P_3 are first determined using Equations (31)–(33):

$$P_1 = \frac{L_{ins}}{D} = \frac{3\,\text{m}}{16\,\text{m}} = \frac{3}{16}$$

$$P_2 = \frac{W}{D} = \frac{16\,\text{m}}{16\,\text{m}} = 1$$

$$P_3 = \frac{Rk}{D} = \frac{\left(\left(1.7611\frac{\text{m}^2\text{K}}{\text{W}}\right)\left(1.8\frac{\text{W}}{\text{m K}}\right)\right)}{(26\,\text{m})} = 0.198$$

Then, the annual average value NTHB is estimated:

$$\text{NTHB} = \frac{[0.8+P_2]^{A_1}}{A_2(P_1)^{A_3} + \left[P_3^{A_4} P_2^{A_5}\right]^{P_1+1}} = \frac{[0.8+1]^{-0.202}}{(0.181)\left(\frac{3}{16}\right)^{(0.747)} + \left[(0.198)^{(0.031)}(1)^{-0.161}\right]^{\left(\frac{3}{16}+1\right)}}$$

$$\text{NTHB} = 0.892$$

Thus, the thermal piles reduce by 11% the annual building foundation heat transfer. The thermal loads associated to the conventional building foundation (i.e., without geothermal heat exchangers) can be estimated using other analysis methods (Krarti, 1999, 2010). It should be noted that using directly a numerical solution, such as the solution outlined in this chapter, for the case of TAF of Figure 2-15, it is found that NTHB = 0.877. Thus, the calculation error, *e*, associated with utilizing the simplified analysis method is determined to be less than 2%:

$$e = \frac{\left| NTHB|_{\substack{\text{Numerical}\\ \text{approach}}} - NTHB|_{\substack{\text{Simplified}\\ \text{Method}}} \right|}{NTHB|_{\substack{\text{Numerical}\\ \text{approach}}}} * 100 = \frac{|0.877 - 0.892|}{0.877} * 100 = 1.71\%$$

2.4 Thermal response of TAFs

In order to model TAFs in whole-building energy simulation programs, thermal response factors, also called G-functions, have been proposed using a similar thermal analysis approach considered for conventional GSHPs. The G-function methodology for GSHPs was first developed by Eskilson (1987) for long-term performance. Then, Yavuzturk and Spitler (1999) developed short time step G-functions. Using G-functions, foundation wall temperatures and geothermal heat exchanger fluid temperatures can be estimated without the need for solving the coupled heat transfer between the ground and the fluid as shown in previous section.

Figure 2-16 illustrates G-functions for various design configurations for GSHPs with vertical boreholes. The mathematical expressions of G-functions are provided by Equations (31) and (32) for long-time steps and for short-time steps, respectively.

[Long-time step G-function]

$$g\left(\frac{t_n - t_{i-1}}{t_s}, \frac{r_b}{H}\right) = \frac{2 \times \pi \times k_{ground}(T_{borehole} - T_{ground})}{Q} \qquad (35)$$

[Short-time step G-function]

$$g\left(\frac{t_n - t_{i-1}}{t_s}, \frac{r_b}{H}\right) = \frac{2 \times \pi \times k_{ground}(T_{borehole} - T_{ground})}{Q} \qquad (36)$$

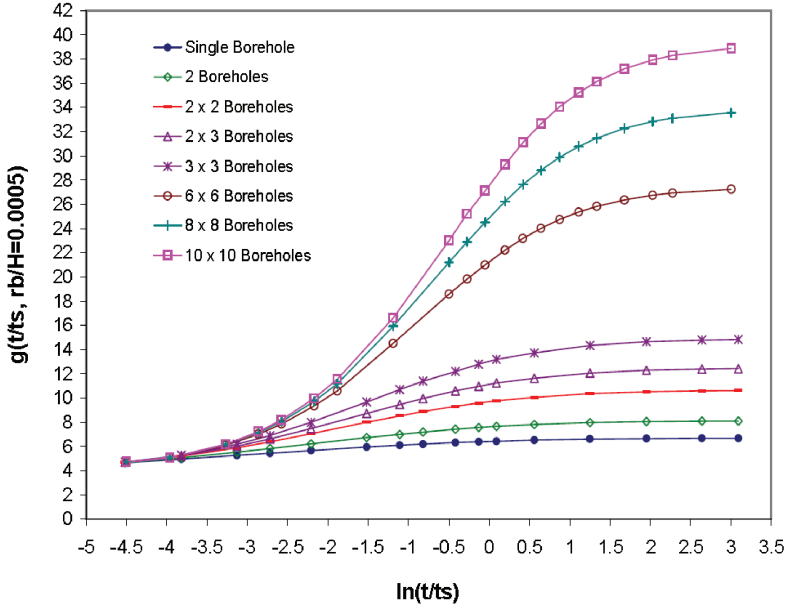

Figure 2-16 G-functions for various configurations associated with GSHPs.

Where, t_s is a time constant function of foundation depth and ground thermal diffusivity:

$$t_s = \frac{H^2}{9\alpha} \tag{37}$$

Recently, Loveridge (2012) and Kwag and Krarti (2013, 2014) have developed G-functions for TAFs. Using these G-functions, the performance of TAFs can be then modeled using whole-building energy simulation programs and can be compared to other heating and cooling systems for buildings. Figure 2-16 compares the G-functions associated to both TAF and GSHP systems. The thermal pile of TAF system and the borehole of GSHP system both have the same hydraulic diameter of 0.7 m and depth of 10 m. As illustrated in Figure 2-17 the G-function short-time step variation for the TAF system is similar to that for GSHP system. However, the long-time step G-function for the TAF system is significantly lower than that of the GSHP system due to the effect of indoor building air temperature. Unlike the case for

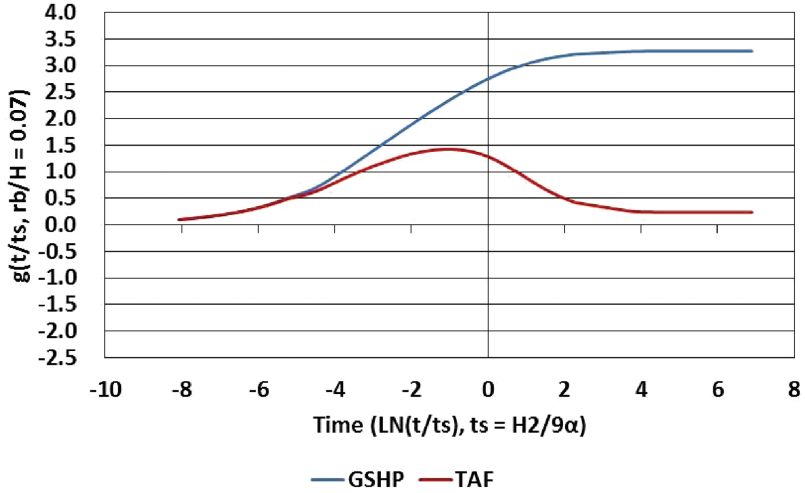

Figure 2-17 G-functions associated to TAF and GSHP systems.

GSHPs, there can be significant thermal interactions between building foundations and geothermal heat exchangers as discussed in the previous section.

Based on the analysis carried out by Kwag (2015) for different TAF pile shapes, G-functions for any shaped thermal piles can be obtained from the G-functions for the circular shaped piles. In particular, Table 2-10 summarizes the G-function equations derived for a circular section, a square section, a rectangular section, and an equilateral triangular section. For each shape, there is a characteristic parameter that can be utilized to estimate the G-function. This characteristic parameter is referred to as the fractional shape factor or F_s. A general expression for F_s can be defined using the hydraulic diameter (D_H) and the perimeter of the foundation pile section (P). The hydraulic diameter is commonly used to analyze fluid flows in noncircular tubes and channels and is defined as:

$$D_H = \frac{4A}{P} \tag{38}$$

Where,

- A = the cross sectional area of a foundation
- P = the perimeter of the foundation

Table 2-10 Modified G-function equations for select cross-sectional configurations of TAF system.

Circular section	Square section
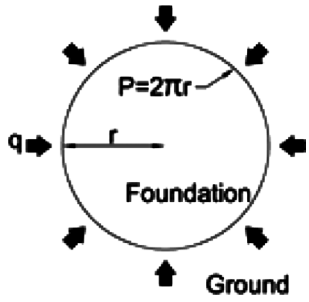	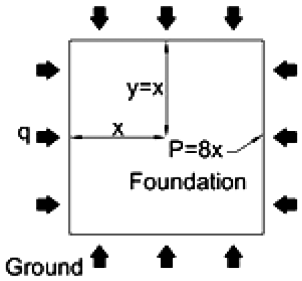
$g\left(\frac{t}{t_s},\frac{r_b}{H}\right)=\frac{2\pi k(T_b-T_g)}{q}$	$g\left(\frac{t}{t_s},\frac{x}{H}\right)=\frac{8k(T_b-T_g)}{q}$
Rectangular section	**Equilateral triangular section**
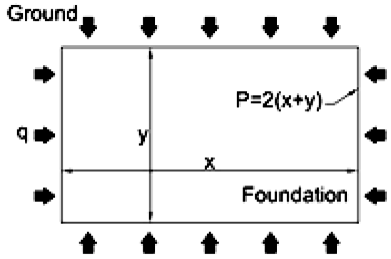	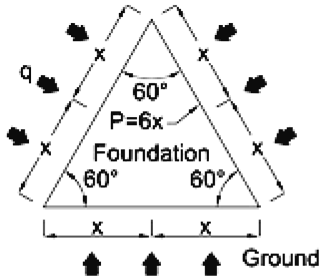
$g\left(\frac{t}{t_s},\frac{xy}{H^2}\right)=\frac{\frac{2(x+y)^2k}{xy}(T_b-T_g)}{q}$	$g\left(\frac{t}{t_s},\frac{x}{H}\right)=\frac{6\sqrt{3}k(T_b-T_g)}{q}$

For any shape including the four shapes considered in Table 2-10, the fractional shape factor can be estimated from both the hydraulic diameter and the perimeter of a foundation pile as noted by Equation (39):

$$F_s=\left(\frac{2P}{D_H}\right) \tag{39}$$

The modified G-function can then found using the fractional shape factor as indicated by Equation (40)

$$g\left(\frac{t}{t_s},\frac{P}{D_H}\right)=F_s\cdot\frac{k(T_b-T_g)}{q}=\left(\frac{2P}{D_H}\right)\cdot\frac{k(T_b-T_g)}{q} \qquad (40)$$

2.5 Energy analysis of buildings with TAF systems

The main purpose of G-function approach is to allow TAF systems to be modeled and evaluated using whole-building energy simulation programs, including EnergyPlus (DOE, 2009) and eQuest (Winkelmann et al., 1993). In this section, the G-function approach developed by Kwag and Krarti (2014) is utilized to assess the effectiveness of TAF systems in meeting heating and cooling loads for prototypical office buildings and residential buildings.

2.5.1 Application of TAFs for office buildings

A prototypical floor of an office building with five thermal zones and a total floor area of 463.6 m^2 (4990 ft^2) as shown in Figure 2-18 was modeled using EnregyPlus to assess the performance of both TAF and variable air volume (VAV) systems. The VAV system is coupled with a temperature based outside air economizer, hot water reheat coils connected to a hot water boiler, and chilled water cooling coils connected to an electric compression chiller with air cooled condenser. The TAF system has a water-to-water heat pump connected to a ground source heat

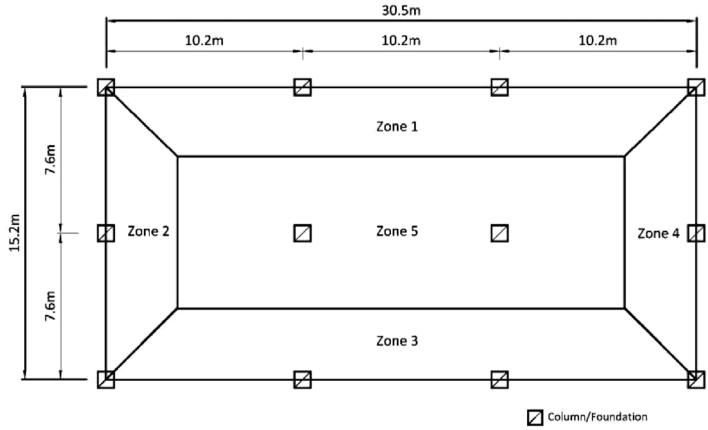

Figure 2-18 Location of foundation piles along the office building slab floor.

exchanger in addition to a boiler and a chiller as illustrated in Figure 2-19. Table 2-11 outlines the input data to model both VAV and TAF systems.

For the energy modeling analysis, Kwag and Krarti (2014) had several assumptions for the integrated simulation including:

- Each thermal foundation has one U-tube heat exchanger loop
- No thermal interactions between TAF piles
- No thermal interactions between building indoor air temperature and TAF piles
- The total number of foundations is 12 for the prototypical office building.
- The distances between foundation piles are 10.2 m and 7.6 m in x-axis and y-axis, respectively as illustrated in Figure 2-18.

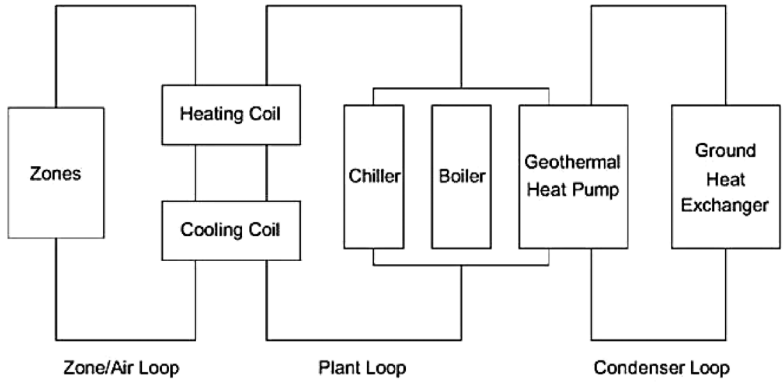

Figure 2-19 Schematic heating and cooling TAF system as modeled in EnergyPlus.

Table 2-11 Model input data for TAF system used in the simulation analysis.

Ground thermal diffusivity [m^2/sec]	$9.41 * 10^{-7}$
Ground thermal conductivity [W/m·K]	1.60
Concrete thermal conductivity [W/m·K]	1.30
Pipe thermal conductivity [W/m·K]	0.36
Foundation depth [m]	20.0
Foundation radius [m]	0.20
Number of thermo-active foundation	12.0

A comprehensive sensitivity analysis was carried out to evaluate the effect of several design parameters on TAF system energy performance to maintain indoor thermal comfort within the office building (Kwag and Krarti, 2014). TAF design parameters, considered in the sensitivity analysis, include thermal foundation depth, H, foundation pile diameter, D, shank space, *S*, soil thermal conductivity, k_{soil}, and thermal concrete thermal conductivity, k_{conc}. The sensitivity analysis was carried out for the climate of Chicago, IL. Figure 2-20 summarizes the results of Kwag et al.'s analysis

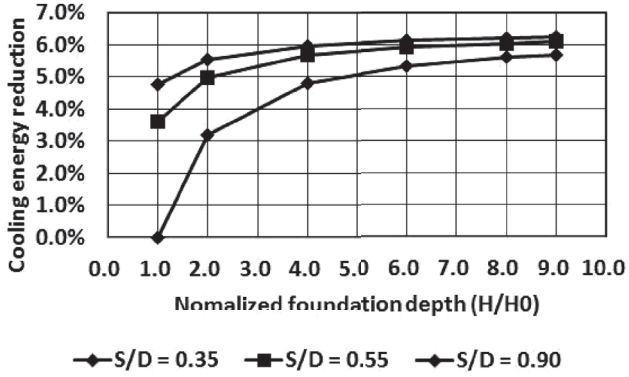

(a)-1. Combination of shank space and foundation depth (D_o = 0.4 m, H_o = 5 m) Cooling

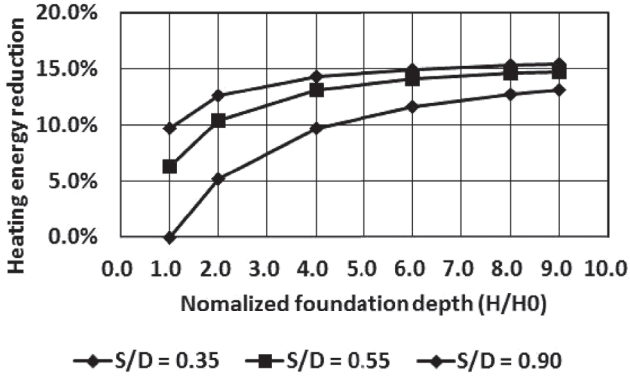

(a)-2. Combination of shank space and foundation depth (D_o= 0.4 m, H_o = 5 m) Heating

Figure 2-20 Impact of TAF design parameters on building heating and cooling energy end-uses for an office building in Chicago, IL. *(Continued)*

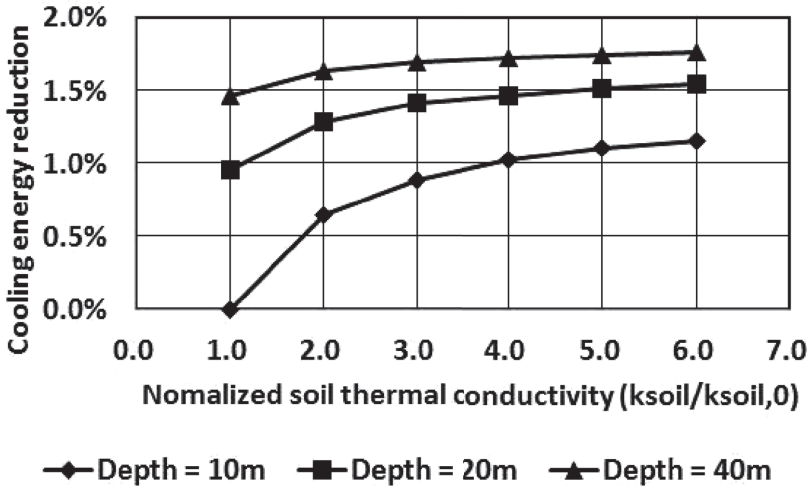

(b)-1. Combination of soil thermal conductivity and foundation depth (H_o = 10 m and $k_{soil,o}$ = 0.4 W/m·K) Cooling

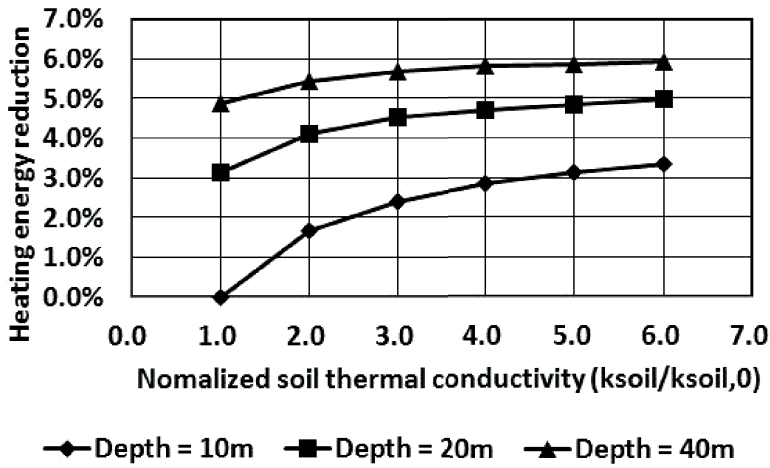

(b)-2. Combination of soil thermal conductivity and foundation depth (H_o = 10 m and $k_{soil,o}$ = 0.4 W/m·K) Heating

Figure 2-20 Impact of TAF design parameters on building heating and cooling energy end-uses for an office building in Chicago, IL. *(Continued)*

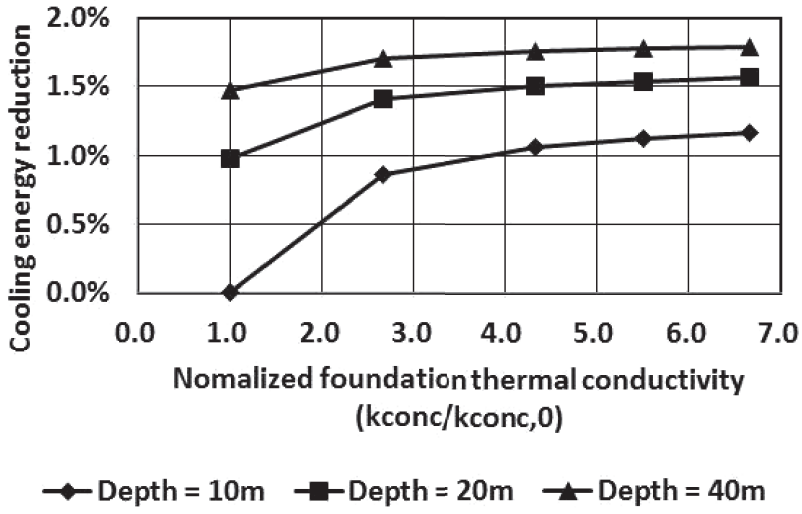

(c)-1. Combination of foundation thermal conductivity and foundation depth (H_o = 10 m and $k_{conc,o}$ = 0.3 W/m·K) Cooling

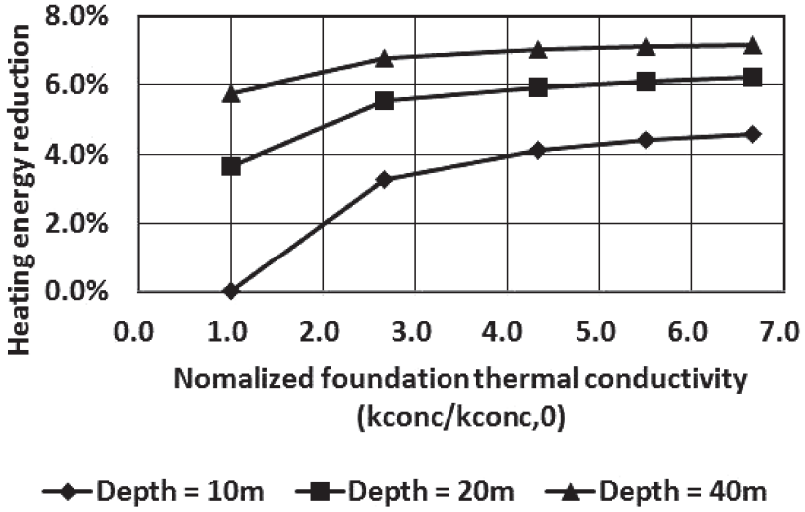

(c)-2. Combination of foundation thermal conductivity and foundation depth (H_o = 10 m and $k_{conc,o}$ = 0.3 W/m·K) Heating

Figure 2-20 Impact of TAF design parameters on building heating and cooling energy end-uses for an office building in Chicago, IL.

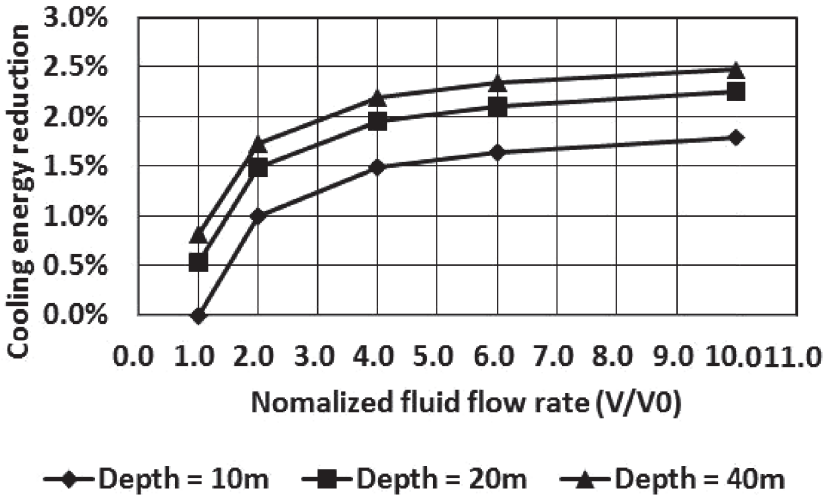

(d)-1. Combination of volumetric flow rate and foundation depth (H_o = 10 m and V_o = 1.75E-5 m^3/s) Cooling

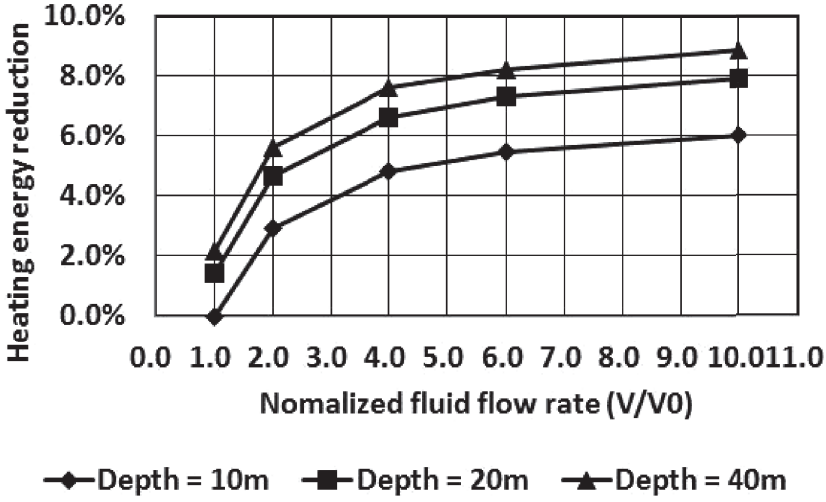

(d)-2. Combination of volumetric flow rate and foundation depth (H_o = 10 m and V_o = 1.75E-5 m^3/s) Heating

Figure 2-20 Impact of TAF design parameters on building heating and cooling energy end-uses for an office building in Chicago, IL.

evaluating the impacts of selected design parameters on the annual energy end-uses for heating and cooling for the office building in Chicago. Reference values for the sensitivity analysis are utilized for all TAF design parameters as noted in the captions of Figure 2-20. The main highlights from the sensitivity analysis results are provided as follow:

- As the pile diameter and shank space increase, heating and cooling energy end-uses decrease due to lowered thermal interactions between heat exchanger pipes [Figure 2-20(a)].
- As the foundation depth increases, heating and cooling energy end-uses are reduced [Figure 2-20(b)].
- As the soil thermal conductivity increases, heating and cooling energy uses are reduced due to higher heat transfer between the foundation loops and the ground [Figure 2-20(c)].
- As the concrete thermal conductivity increases, heating and cooling energy uses are reduced due to lower thermal resistance to heat transfer between the foundation loops and ground [Figure 2-20(d)].
- As the fluid flow rate increases, heating and cooling energy uses are reduced due to higher convective heat transfer coefficients within the foundation heat exchanger loops [Figure 2-20(e)].

Kwag and Krarti (2014) also evaluated the impact of climate conditions on energy performance of TAF systems to heat and cooling the prototypical office building of Figure 2-18. Five representative U.S. climate conditions were considered including Chicago, IL, New York, NY, Phoenix, AZ, Denver, CO, and Cheyenne, WY. Table 2-12 outlines the

Table 2-12 Annual average thermal energy consumptions of a base case in different climate conditions.

	Chicago, IL	New York, NY	Phoenix, AZ	Denver, CO	Cheyenne, WY
Cooling Energy [GJ]	77.483	77.271	83.983	75.510	73.317
Heating Energy [GJ]	66.543	49.549	12.044	49.182	64.374

annual average energy consumption to cool and heat the prototypical office building using a standard VAV system. The standard VAV system is served by a boiler and a chiller as summarized in Table 2-13.

A TAF system is then considered to maintain thermal comfort in the prototypical office building using 12 thermal foundations pile with a depth of H = 20 m. The energy consumption for both heating and cooling associated with TAF systems is summarized in Figure 2-21 for all five US climates. As shown in Figure 2-20, TAF systems reduced the annual heating and cooling energy end-uses of the office building. Because of the relatively small thermal loads of the prototypical small office building, the simulation results show high reduction in cooling energy end-use from 18% (Cheyenne, WY) to 52% (Phoenix, AZ) and heating energy end-use from 40% (Phoenix, AZ) to 52% (Denver, CO). These results indicate that TAF systems can significantly reduce cooling and heating energy consumption for office buildings.

Table 2-13 Chiller and boiler capacities for a base case.

	Chiller: Electric	Boiler: Gas
Capacity [kW]	200.0	90.0
Nominal Efficiency	COP = 3.2	80%

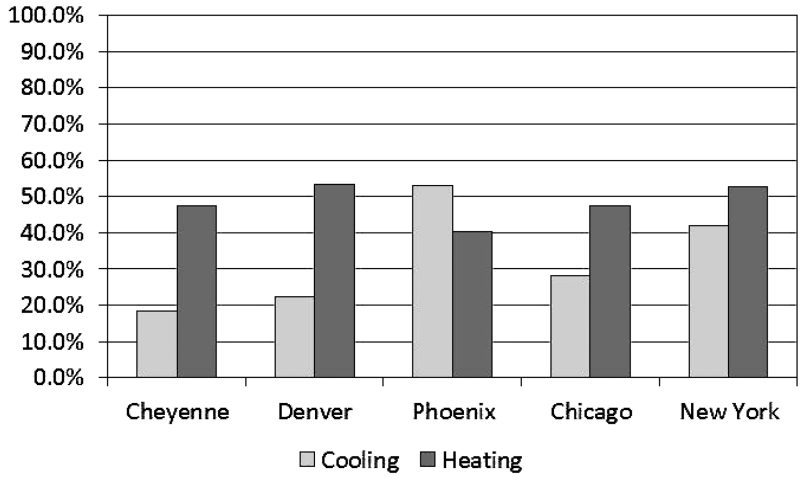

Figure 2-21 Percent reduction of cooling and heating energy end-uses associated with a TAF system relative to a VAV system for a prototypical office building in five US climates.

2.5.2 Application of TAFs to residential buildings

The performance of TAF systems to air condition residential buildings has also been evaluated using an apartment building located in Boulder, Colorado (Kwag, 2015). The climate of Boulder, CO. is typically dry year round, cold in winter and warm in summer as shown in Figure 2-22. The apartment building has three stories with 6 units per floor. Figure 2-23 illustrates the prototypical building modeled using EnergyPlus, a whole-building energy simulation program. The net conditioned floor area for the apartment building is 111.5 m^2 (1200 ft^2). The total building floor area including all unconditioned areas is 2899 m^2 (31,210 ft^2). Table 2-14 provides the basic data used to develop the energy model for the residential building.

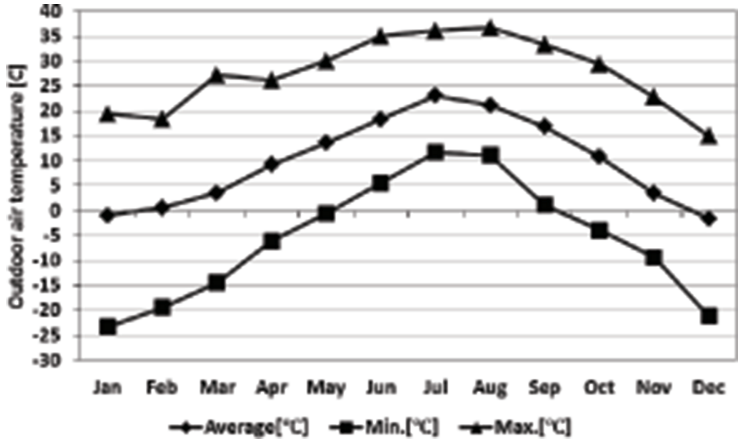

Figure 2-22 Monthly average outdoor air dry-bulb temperature of Boulder, CO.

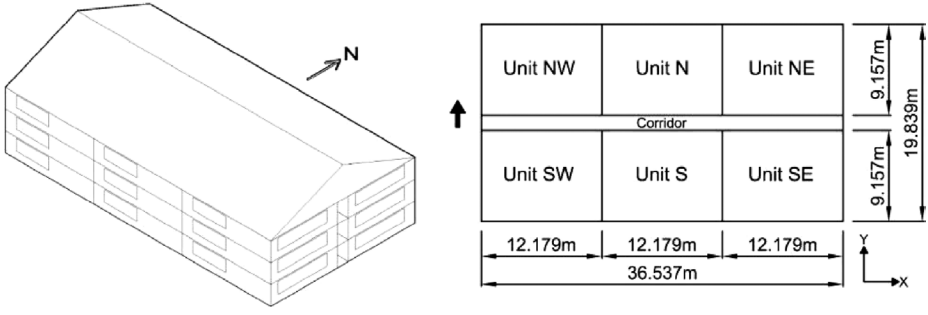

Figure 2-23 Apartment building model.

Table 2-14 Basic features of the prototypical multi-family residential building.

Building Sizes Summary	
Unit Size	(x) 12.179 m, (y) 09.157 m, (z) 2.59 m
Corridor Size	(x) 36.537 m, (y) 01.525 m, (z) 2.59 m
Building Size	(x) 36.537 m, (y) 19.839 m, (z) 7.77 m (11.9 with attic)
Number of Floor	3 stories
Number of Units per Floor	6 units per floor
Building Envelope Summary	
External Roof	0.943 Btu/h·ft^2
External Wall	0.065 Btu/h·ft^2
External Floor	0.032 Btu/h·ft^2

In the analysis, it was assumed that the baseline heating, air conditioning, and ventilating (HVAC) system includes a central system with an electric chiller for cooling, and a hot water gas boiler to provide heating as well as domestic hot water for each apartment unit. Figure 2-24 shows the monthly electricity and gas consumptions of the multi-family residential building served by the baseline HVAC system.

The performance of a TAF system is modeled using EnergyPlus in order to estimate the energy end-uses to heat and cool the apartment building using the G-function approach. Figures 2-25 and 2-26 present the cooling and heating end-uses for several heat pump sizes when TAF system is used to air condition the residential building. The simulation

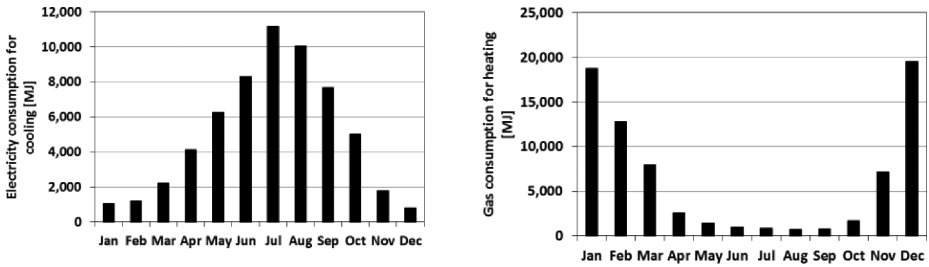

Figure 2-24 Monthly energy consumptions for cooling (electricity), and for heating (gas) using the baseline HVAC system.

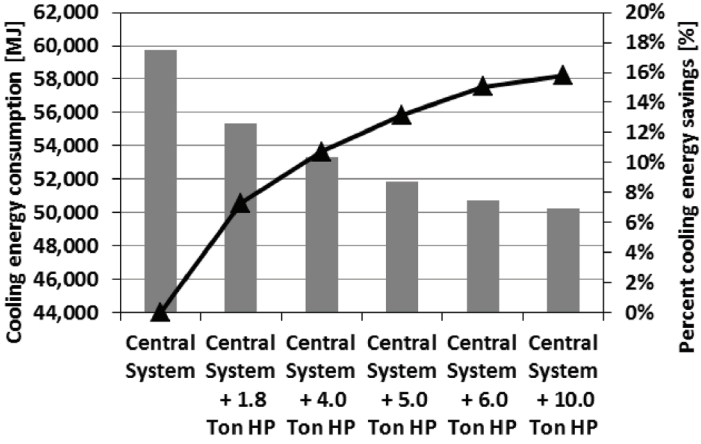

Figure 2-25 Annual cooling energy consumption as a function of heat pump size.

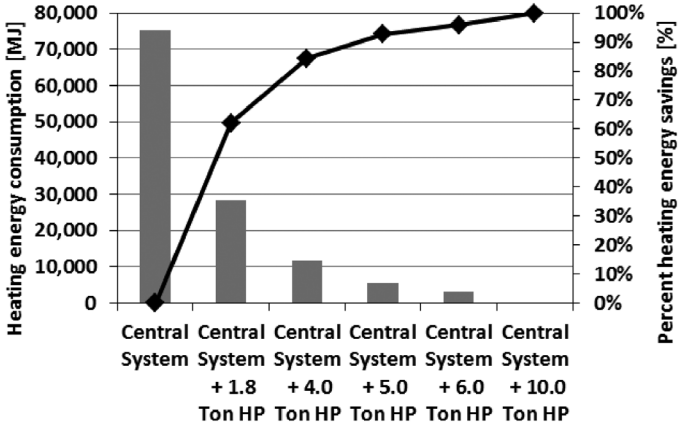

Figure 2-26 Annual heating energy consumption as a function of heat pump size.

results indicate that TAF systems can reduce significantly the building energy consumption required for heating when the apartment is located in Boulder, CO, a heating dominated climate. As the heat pump size is increased, a high reduction in both heating and cooling energy end-uses is achieved. Thus, proper design of the heat pump is crucial to optimize the performance of TAF systems.

2.6 Summary and conclusions

As alternatives to ground-source heat pump (GSHP) systems, thermoactives foundations (TAFs) have been considered to provide air conditioning to both residential and commercial buildings. The main advantage of TAFs is reduced installation costs compared to GSHP systems with similar benefits. Unfortunately, TAFs have not been by architects and engineers to heat and cool buildings especially in the US market due to limited research studies and design guidelines.

In this chapter, an overview of the state-art of thermal modeling of thermo-active foundations (TAFs) is presented. In particular, three-dimensional TAF models have been outlined and selected results have been discussed. Moreover, thermal response functions associated with TAF systems, also called as G-functions, are defined using for both long time and short time steps. The G-functions for TAFs have been compared to those obtained for ground-source heat pumps (GSHPs) and are estimated for a wide range of foundation pile shapes.

By integrating G-functions into EnergyPlus, the energy consumption of TAF system to heat and cooling buildings has been estimated for a wide range of design and operating conditions. In particular, the thermal performance and design specifications were found to depend on a wide range of parameters in addition to the heating and cooling of buildings. The impact on energy performance of TAF systems of select parameters were discussed in this chapter including foundation pile depth, diameter, shank space, and shape, as well as soil thermal conductivities for soil and concrete.

Detailed energy simulation of two building types has been carried out using TAFs as heating and cooling systems for representative US climates. Through the simulation analysis, it was found that TAFs can reduce annual cooling and heating energy use of residential and commercial buildings by 20–55% for a wide range of US climates.

In order to insure that TAFs can be widely applied as heating and cooling systems for buildings, design guidelines have to be developed to account for the main design parameters and climatic conditions. Moreover, long term monitoring of TAF systems in real buildings has to be carried out for a wide range of building types and climates.

2.7 References

Abdelaziz, S.L., Olgun, C.G., and Martin, J.R., II., 2011, "Design and Operation Considerations of Geothermal Energy Foundations." *GeoFrontiers 2011*. Dallas, TX. ASCE, pp. 450–459.

ASHRAE, 2013, "ASHRAE Handbook of Fundamentals," *American Society for Heating, Refrigerating, and Air Conditioning Engineers Inc*., Atlanta, GA.

Brandl, H., 2006, "Energy foundations and other thermo-active ground structures," *Geotechnique*, 56(2), 81–122.

Cengel, Y., Turner, H., and Cimbala, J., 2008, *Fundamentals of Thermal-Fluid Sciences*. McGraw-Hill, New York, NY.

DOE, 2009, "EnergyPlus Engineering Reference, Department of Energy, Energy Efficiency and Renewable Energy," Building Technologies Program, Washington DC. http:// apps1.eere.energy.gov/buildings/energyplus/.

Eskilson, P., 1987, "Thermal Analysis of Heat Extraction Boreholes." Doctoral Thesis, University of Lund, Department of Mathematical Physics. Lund, Sweden.

Hamada, Y., Nakamura, M., Kubota, H., and Ochifuji, K., 2007, "Field performance of an energy pile system for space heating". *Energy and Buildings*, 39(5), 517–524.

Hernandez Guerrero, A.H., and M. Krarti, M., 2014, "Foundation heat transfer analysis for buildings with thermal piles," *Energy Conversion and Management*, 89, 449–457.

Jalaluddin, Miyara A., Tsubaki K., Inoue S., and Yoshida K., 2011, "Experimental study of several types of ground heat exchanger using a steel pile foundation," *Renewable Energy*, 36, 764–771.

Kaltreider, C., 2011, Numerical Modeling of Heat Transfer in Thermo-Active Foundations, MS Thesis Report, University of Colorado, Boulder, CO.

Kaltreider C., Krarti, M., McCartney, J., 2015, "Heat Transfer Analysis of Thermo-active Foundations," *Energy and Building*, 86(1), 492–501.

Kavanaugh, S., 2010, "An Instruction Guide for Using a Design Tool for Vertical Ground-Coupled, Groundwater and Surface Water Heat Pumps Systems-Ground Source Heat Pump System Designer, GshpCalc Version 5.0. Energy Information Services," Northport, AL. http://www.geokiss.com.

Krarti, M., 1999, "Ground-Coupled Heat Transfer," a chapter in Advances in Solar Energy, edited by Goswami, ASES publication, 90 pages, Boulder, CO.

Krarti, M. Energy Audit of Building Systems: An Engineering Approach, Second Edition, *CRC Press*, Boca Raton, FL, 2010.

Kwag, B.C., and Krarti, M., 2013, "Performance of Thermoactive Foundations for Commercial Buildings," *ASME Solar Energy Engineering Journal*, 135(4), 040907-040907-10.

Kwag, B.C., and Krarti, M., 2014, "Development of a response factor model for thermo-active building foundation," *Proceedings for ASME 2014 International Mechanical Engineering Congress and Exposition*, November 10–14, Montreal, Canada.

Kwag, B.C., 2015, "Thermal Performance and Design Guidelines of Thermo-active Foundations," PhD Dissertation, University of Colorado, Boulder, CO.

Laloui, L., Nuth, M., and Vulliet, L., 2006, "Experimental, numerical investigations of the behaviour of a heat exchanger pile." *Int. J. for Num. and Analytical Meth. in Geomech.*, 30(8), 763–781.

Lee, J.U., Kim, T., and Leigh, S.B., 2013, "Thermal performance analysis of a ground-coupled heat pump integrated with building foundation in summer," *Energy and Buildings*, 59, 37–43.

Loveridge, F., 2012, "The thermal performances of foundation piles used as heat exchangers in ground energy systems," University of Southampton, Faculty of Engineering and the Environment, Doctoral Thesis, 2012.

Loveridge, F., and Powrie, W., 2013, "Temperature response functions (G-functions) for single pile heat exchangers," *Energy*, 57, 554–564.

McCartney, J.S., Rosenberg, J.E., and Sultanova, A., 2010, "Engineering performance of thermo-active foundation systems." GeoTrends: The Progress of Geological and Geotechnical Engineering in Colorado at the Cusp of a New Decade (GPP 6). C.M. Goss, J.B. Kerrigan, J. Malamo, M.O. McCarron, and R.L. Wiltshire, eds. *ASCE*. pp. 27–42.

McCartney, J.S., and Rosenberg, J.E., 2011, "Impact of heat exchange on the axial capacity of thermo-active foundations." *Proceedings of Geo-Frontiers 2011 (GSP 211)*. J. Han and D.E. Alzamora, eds. *ASCE*, Reston VA. pp. 488–498.

Ooka, R., Sekine, K., Mutsumi, Y., Yoshiro, S., and SuckHo, H., 2007, "Development of a Ground Source Heat Pump System with Ground Heat Exchanger Utilizing the Cast in Place Concrete Pile Foundations of a Building." *EcoStock 2007*. Stockton, NJ.

Rosenberg, J., 2010, Centrifuge Modeling of Soil Structure Interaction in Thermo-Active Foundations. MS Thesis report, University of Colorado, Boulder, CO.

Rouissi, K., Krarti, M., and McCartney, J.S., 2011, "Analysis of Thermo-Active Foundation using U-Tube Heat Exchangers," *ASME Solar Energy Engineering Journal*, 134(2), 154–161.

Sekine, K., Ooka R., Yokoi M., Shiba Y., and Hwang S., 2007, "Development of a Ground-Source Heat Pump System with Ground Heat Exchanger Utilizing the Cast-in-Place Concrete Pile Foundations of Buildings," *ASHRAE Transactions*, DA-07-061: 558–566.

Stewart, M.A., and McCartney, J.S., 2013, "Centrifuge modeling of energy foundations under cyclic heating and cooling," *ASCE Journal of Geotechnical and Geoenvironmental Engineering*, 1–11. doi: 10.1061/(ASCE)GT.1943-5606.0001061.

Winkelmann, F.C., Birsdall, B.E., Bull, W.F., Ellington, K.L., Erdem, A.E., and Hirsh J.J., 1993, "DOE-2 supplement, version 2.1E," Technical Report LBL-34947, Lawrence Berkeley National Laboratory, Berkeley, CA.

Wood, J.C., Liu H., and Riffat S.B., 2010, "An investigation of the heat pump performance and ground temperature of a piled foundation heat exchanger system for a residential building", *Energy*, 25, 4932–4940.

Yavuzturk, C., and Spitler, J.D., 1999, "A short time step response factor model for vertical ground loop heat exchangers." *ASHRAE Transactions*, 105(2), 465–474.

Yavuzturk, C., and Spitler, J.D., Rees, S.J., 1999, "A Transient Two-Dimensional Finite Volume Model for the Simulation of Vertical U-Tube Ground Heat Exchangers." *ASHRAE Transactions*, 105(2), 475–485.

3. Full scale geothermal energy pile studies at Monash University, Melbourne, Australia

Abdelmalek Bouazza, Ph.D., FIEAust, Monash University, Australia, Rao Martand Singh, Ph.D., University of Surrey, U.K., and Mohammed Faizal, M.S., Monash University, Australia

Abstract: Geothermal energy piles are dual-purpose structural elements that provide structural support to built structures and act as heat exchange units to supply space heating and/or cooling. This chapter presents results from two studies conducted on full scale geothermal energy piles installed at Monash University, Melbourne, Australia. Study 1 focused on the thermal and thermo-mechanical behavior of a single pile, installed in December 2010. It showed that the pile and the ground required at least more than twice the heating time to return to initial thermal conditions. Furthermore, it has been found that the pile shaft capacity increased after the pile was heated and returned to the initial capacity (i.e., initial conditions) when the pile was allowed to cool naturally. This indicated that no losses in pile shaft capacity were observed after heating and cooling cycles. A variance in average vertical thermal strains was observed at the end of the heating periods. These were almost fully recovered at the end of the cooling periods indicating that they were of an elastic nature. Study 2 involved a group of energy piles (two piles) installed in October 2014 as part of the pile foundations system of a multi-story residential building. They will become operational at end of year 2015 when the superstructure is completed. Initial observations related to concrete curing indicate that concrete was initially in tension due to the cement hydration process but reversed to compressive strains once it cooled down and its temperature was in equilibrium with the surrounding soil.

3.1 Introduction

Geothermal energy piles, also known as thermo-active piles, are defined as dual-purpose structural elements. They utilize the required ground-concrete contact element to transfer the construction loads to the ground as well as acting as heat exchanger units (Brandl 2006; Adam and

Markiewicz 2009). They are similar to vertical borehole heat exchangers coupled with ground source heat pump (GSHP) systems. The difference is the pile foundations serve as an integral support to the built structure in addition to heating and cooling it. Energy pile foundations have great potential of improving the energy efficiency of built structures by using the ground as heat source/sink to provide space heating and/or cooling. This chapter presents two field experimental cases where geothermal energy piles were installed in relatively dense sandy sites located at Monash University, Melbourne, Australia. The first case was aimed at investigating the thermo-mechanical behavior of an energy pile with particular focus on post-heating behavior of the pile shaft resistance. This study was performed on a single pile equipped with two Osterberg cells (O-Cells) to allow for multidirectional movements of the pile shaft. The second case involved a group of energy piles (two piles) installed as part of the pile foundations system of a multi-storey residential building. These piles were recently installed and will be operational at end of year 2015 when the superstructure is completed. The focus of this latter case is on the piles' long term thermo-mechanical performance under operational conditions.

3.2 Site ground conditions

Tertiary aged Brighton Group sediments were encountered on both pile sites. This is an important geological unit of Melbourne because of its extensive surface coverage of the south-eastern suburbs of the city (Chandler 1992). The Brighton Group comprises two major formations, the Red Bluff Sands and the underlying Black Rock Sandstone. The Red Bluff Sands are commonly encountered from the subsurface where they consist of clays, sandy clays, clayey sands, sands and occasionally silts. The stratigraphy of the Red Bluff Sands commonly shows a surface layer of clay or clayey sand with a decrease in clay content with depth leading into silty sands and sands. It is generally mottled with red-brown-grey in colour and often fissured in clays and iron cemented in sands. There was no groundwater present at the pile locations. Laboratory thermal conductivity of the soils collected during the drilling process ranged from 1.6 W/mK at 8 m depth to 2.2 W/mK at 12 to 14 m.

In-situ temperature profiling was conducted over a period of 12 months (from December 2012 to November 2013). Only one day of every month of monitoring is reported in this chapter. Temperatures profiling are presented for the 8th of every month at 12 pm. Monitoring of temperature

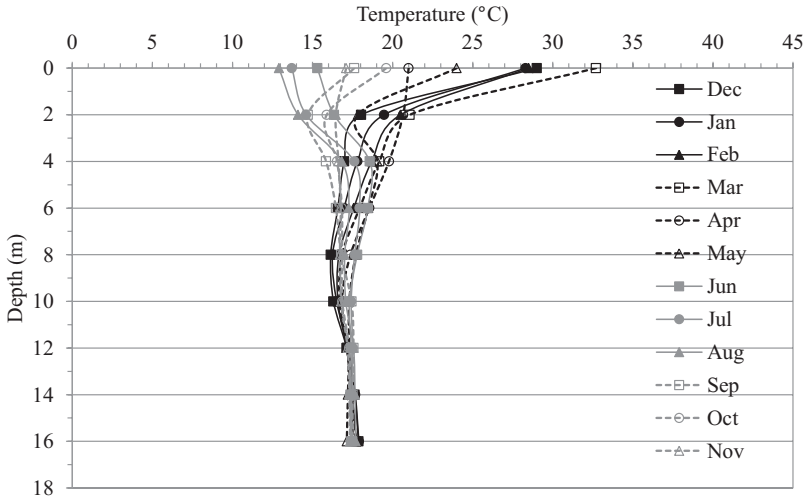

Figure 3-1 Undisturbed ground temperature from Dec. 2012 to Nov. 2013.

variation with depth, shown in Figure 3-1, indicates that the temperature of the surface zone (approximately 2 m below ground surface) and, to a lesser extent, that of the shallow zone (2 to 4 m) are influenced by short term ambient temperature changes. The sudden damping of temperature at 2 m is caused by the insulating effect of the fill material covered by grass. Temperature deviation from the average temperature (i.e. 18 °C) at 2 m depth varies by ±3.5 °C, at 4 m by ± 2 °C and at 6 m by ±1 °C. These variations begin to diminish upon reaching a depth greater than that of the shallow zone. Beyond 8 m (deep zone) temperatures are relatively constant (17.5–18.5 °C) and are unaffected by seasonal temperature changes making them suitable for geothermal energy pile systems. It should be noted that the soil below a built structure will be shielded from solar thermal and atmospheric effects, and thus is expected to show a constant temperature variation from the ground surface.

3.3 Instrumentation of full-scale geothermal energy piles

3.3.1 Single geothermal energy pile instrumentation

A 0.6 m diameter bored pile was installed to a depth of 16.1 m along with a two-level Osterberg-cell (O-cell) testing system (see Figure 3-2). The O-cell is a static form of testing although its application is inherently different to other existing pile load tests (i.e. Statnamic, anchored

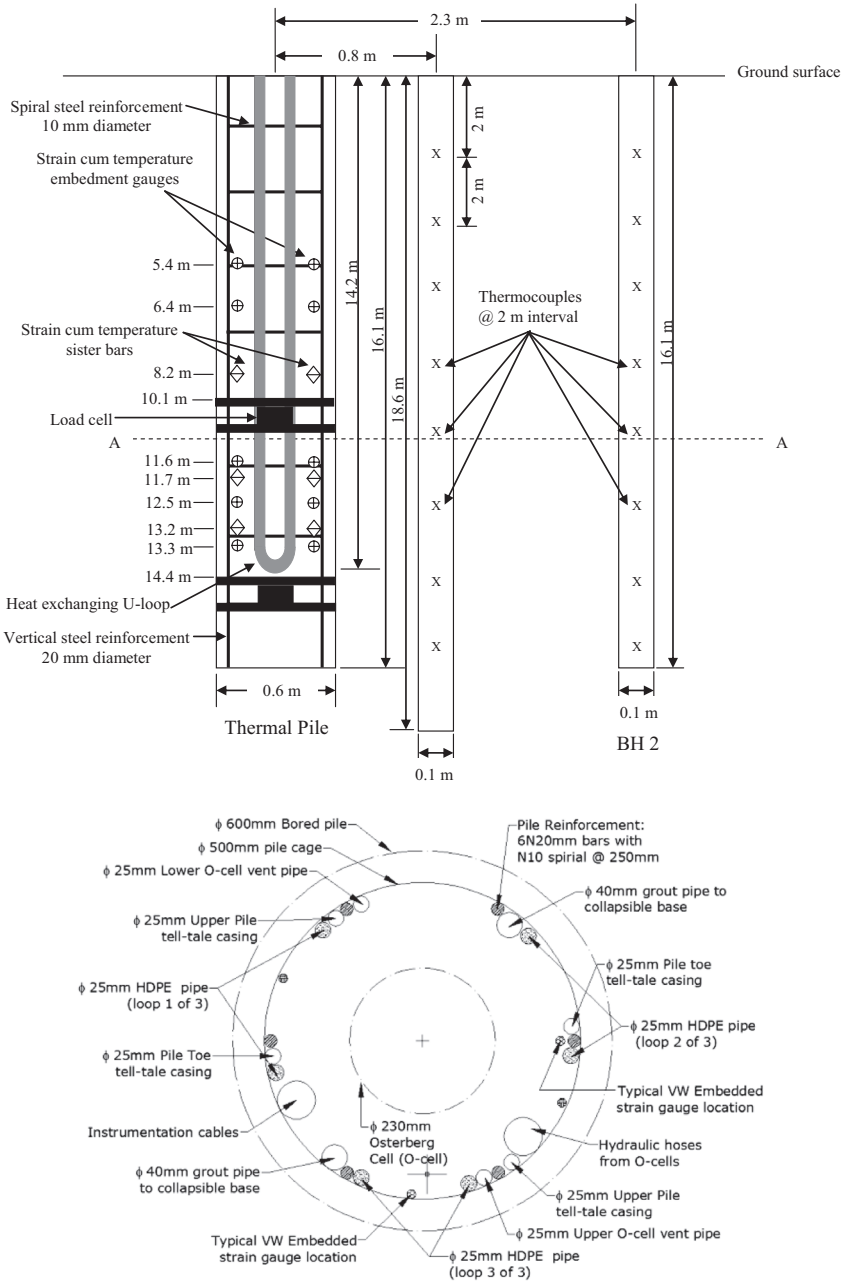

Figure 3-2 Schematic of single energy pile, boreholes, and cross section showing the location of sensors (from Wang et al. (2015)).

loading system, etc.). The O-cell is a hydraulic driven, sacrificial loading jack installed within the test pile, allowing the pile to undergo bi-directional motion axially The O-cell creates axial stresses (or loads) that are resisted by pile shaft and base resistances. The cell is capable of opening or expanding to 150 mm and is usually attached to the reinforcing cage that is cast within the pile.

The O-cells presented two breaks at their installed locations along the pile shaft, at approximate depths of 10 m and 14 m. Consequently, the pile shaft was divided into three sections, the 10.1 m upper section, the 4 m middle section and the lower 1 m section at the pile base. The steel reinforcement cage consisted of six vertical steel bars of 20 mm diameter held by spiral bars of 10 mm diameter and 250 mm spacing. The installation was undertaken by solid auger bored pile drilling technique without the use of drilling fluid (also known as open hole method). Approximately ten litres of grout was poured into the drilled shaft to provide a level pile base prior to lowering of the pile reinforcement cage. The pile was fitted with ten vibrating wire strain cum temperature gauges installed in the space between the O-cells, and six vibrating wire strain gauges above the upper O-Cell to measure concrete strain and temperature during thermal and mechanical loading. Twelve vibrating wire displacement transducers were used to measure displacement of the pile shaft, and two vibrating wire pressure transducers measured the O-Cell loads. Figure 3-2 shows the location of the sensors installed within the energy pile.

Three high density polyethylene (HDPE) pipe loops, 25 mm outside diameter, were attached to the reinforcement pile cage to carry the heat transfer medium needed for the thermal loading. The pipes were attached to the inner side of the steel reinforcement cage and were installed to the top of the lower O-Cell to a depth of 14.2 m and 50 mm from the edge of the pile. Due to limited space within the reinforcement cage, 'U' shaped electro-fusion fittings were utilised to form 'U' bends at the end of each of the three loops. Spacing between the loops was about 175 mm. Water was used as the medium to transfer heat to the ground during thermal loading of the test pile. Heating of the pile was carried out using a heating unit commonly utilised to measure thermal properties within vertical borehole heat exchangers.

Two boreholes (BH1 and BH2) of 100 mm diameter located at 0.5 m and 2 m, respectively, from the edge of the pile were drilled to depths of 18.6 m and 16.1 m, respectively. The boreholes were filled with cement slurry

and then thermocouples attached to a hollow plastic pipe were placed at the center of each borehole. The first thermocouple was installed at 2 m from the ground surface and subsequent thermocouples were placed at every 2 m distance from each other as shown in Figure 3-2. Further details on pile installation and instrumentation can be found in Wang et al. (2015).

3.3.2 Instrumentation of group of geothermal energy piles

Two 0.6 m diameter bored piles, 10 m deep, from a set of foundation piles for a new residential building currently being built at Monash University were converted to geothermal energy piles for full scale experimental studies. The pile reinforcement cage contained ten vertical reinforcement bars of 30 mm diameter, outer ring diameter of 445 mm made with 16 mm diameter rod which were spread spirally across the length of the pile cage at a spacing of 150 mm. Four U-loops of standard HDPE pipes were installed in each pile. The average concrete cover to the edge of pipes was 95 mm. The spacing between the pipes in a given U-loop was close to 200 mm. Pile one (see Figure 3-3) was instrumented with 30 vibrating wire strain cum thermal gauges installed at five levels along the pile, 14 type T thermocouples installed at three levels on the external wall of the pipes, and three thermocouples at the soil/concrete interface. At each of the five levels, there are four vertical strain gauges, one central vertical strain gauge and one radial strain gauge placed close to the center. The average concrete cover to the four outer vertical strain gauges is 160 mm. The vertical strain cum temperature gauges were installed at depths of 1 m (Level E), 3.05 m (Level D), 5 m (Level C), 7.28 m (Level B), and 9.5 m (Level A). The radial gauges are installed at depths of 1.36 m (Level E), 3.3 m (Level D), 5.3 m (Level C), 7.46 m (Level B), and 9.25 m (Level A). The vertical gauges at each level are referenced as V1, V2, V3, V4, and V5, whereas the radial gauges are referenced as R (e.g., AV1 = vertical gauge at 160 mm concrete cover at a depth of 9.5 m, AR = radial gauge at 9.25 m depth). The plan view of the sensor locations is shown in Figure 3-3.

The radial gauges were placed vertically off set from the central vertical gauges due to space limitations in the pile cage. The thermocouples installed at the concrete/soil interface were tied to a steel cable with a dead weight at its end and dropped along the side of the borehole wall after the pile cage was lowered. These thermocouples were placed at depths of 1.1 m, 3.6 m, and 6.6 m. The thermocouples on the HDPE pipe walls are at depths of 1.30 m, 5.00 m, and 9.80 m. Pile two had only three thermocouples installed

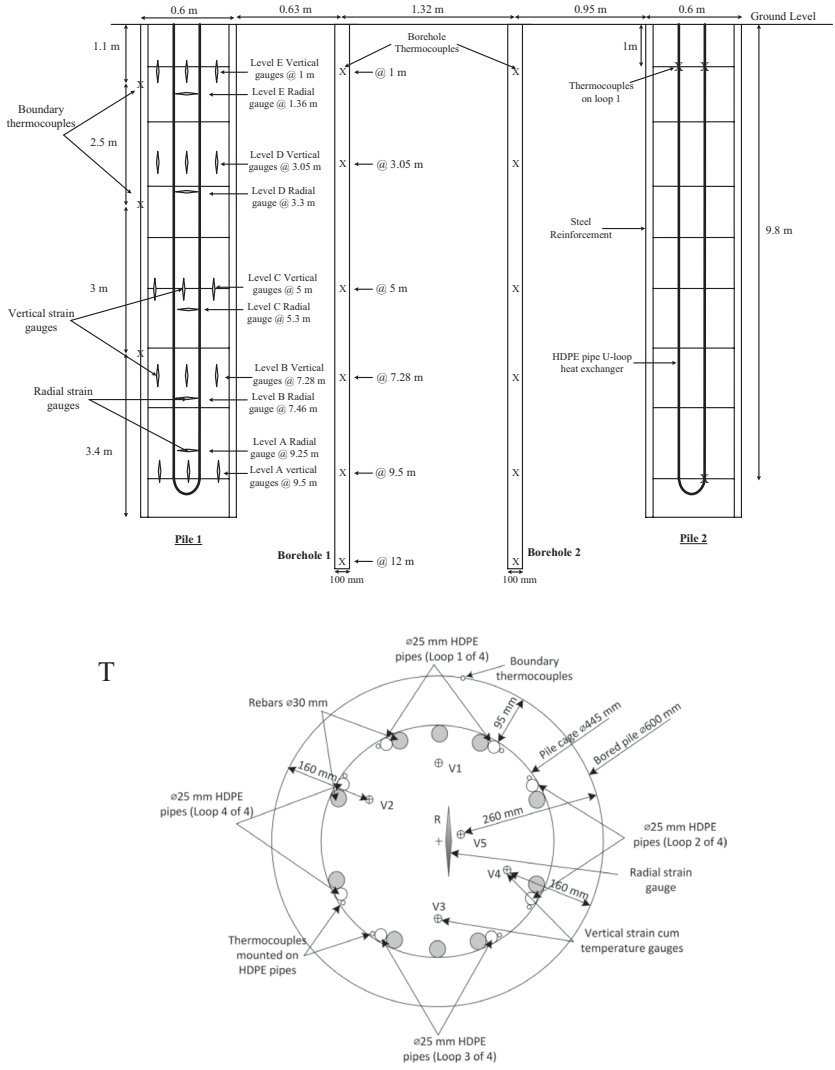

Figure 3-3 Schematic of dual piles, boreholes, and cross section showing the location of sensors.

across loop one, they are at depths of 1 m and 9.8 m. Figure 3-3 shows the location of all the sensors in the two piles. Two boreholes of 100 mm diameter were installed between the two piles to monitor the ground thermal response during thermal loading. Each borehole was equipped with a set of six thermocouples installed on the outer surface of a hollow PVC pipe, inserted in each borehole, at depths of 2 m intervals.

3.4 Heating test for single pile case

A heating test was carried out on the single geothermal pile using a thermal response unit. The unit consisted of a water reservoir and a pump, four heating elements (three 1500 W and one 2500 W), a data logger, a control box, one inlet and one outlet for the heating fluid. The data logger monitored and recorded inflow and outflow temperatures of the heating fluid, the power applied to the heating fluid and interval times of the recorded data. The water pump was equipped with a variable flow valve to control speed of flow. The flow rate of the heating fluid was manually measured and recorded at the end of the thermal test. The heating test was carried out by transporting the heat transfer fluid through all three loops in a continuous series within the pile and lasted for nine days. Inflow and outflow temperatures of the heat transfer fluid and the pile concrete temperatures were recorded continuously during the heating periods. The test pile and the ground were cooled naturally by stopping the fluid circulation and letting the induced heat dissipate into the surrounding environment following each heating test. The heating test was subjected to a thermal load of approximately 2500 W throughout the heating periods. A constant flow rate of approximately 10 litre/minute of the heat transfer fluid was also maintained during the heating period.

Transient temperature of circulating water in the heat exchanging loops and heat exchange rate of the energy pile are shown in Figure 3-4.

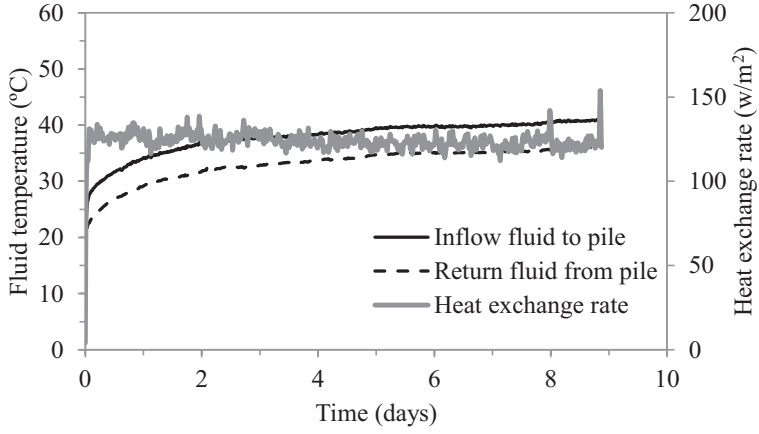

Figure 3-4 Heat transfer fluid temperature during heating test.

The maximum temperature of water entering and leaving the loops reached 41 °C and 36 °C, respectively, at the end of the heating test. The temperature difference between water entering and leaving the loops is 5 °C and remained the same throughout the test. The average heat exchange rate of the energy pile was 122 W/m^2.

Figure 3-5a presents the pile transient temperature. The temperature was found to increase at all locations within the pile during the heating test and decreased steadily after the test was stopped. No time lag was observed, as the temperatures reached their peak values exactly

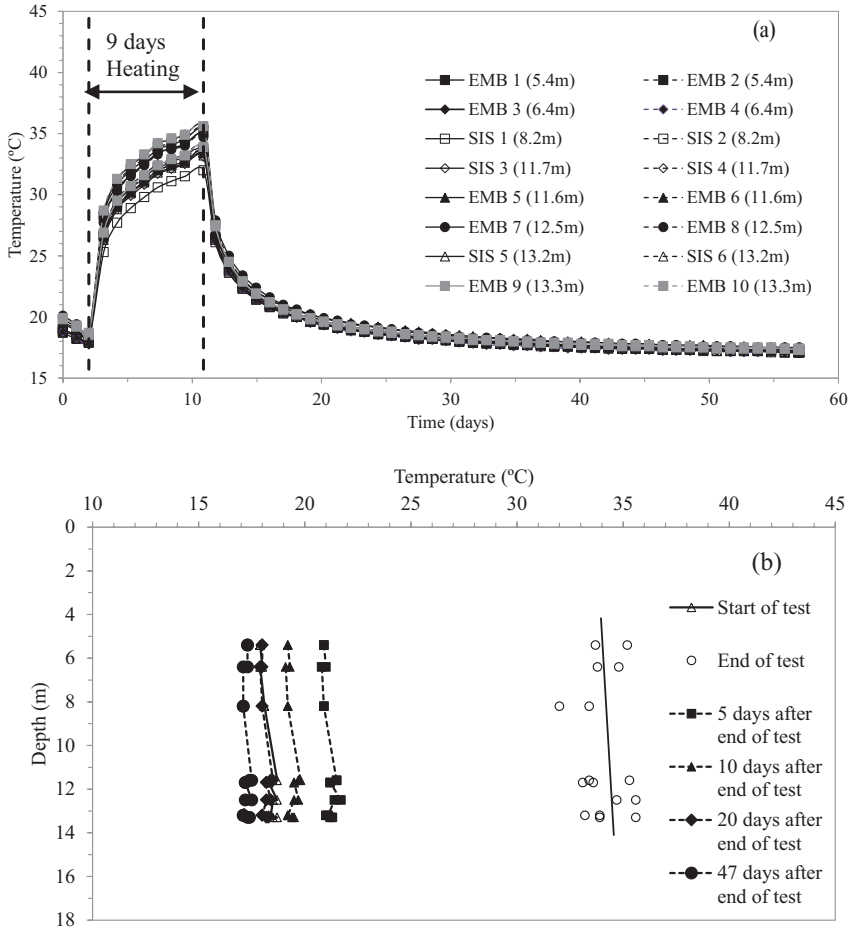

Figure 3-5 Pile temperature response to heating test (a) transient temperature (b) temperature profile.

at the same time when the test was completed. This is because the heat had already overcome the pipe resistance during a preliminary heating test.

Figure 3-5b shows the pile thermal profile at different times. The highest temperature (35°C) was recorded at locations where the temperature gauges were closest to the loops while the lowest temperatures (31°C) were observed away from the loops. The sister bar gauges show lower temperature compared to the embedment gauges because they are longer and capture the temperature range for a larger portion of the pile. The temperature decreased rapidly and uniformly five days after the heating test was completed. There is a lesser temperature fall after ten and 20 days from the test stoppage compared to five days cooling period. There is a full thermal recovery after 20 days as the temperature reached the initial values observed before the heating test. The pile took twice the amount of time used for the heating test to have full natural thermal recovery. After 47 days cooling the pile returned fully to the temperature levels recorded before any heating test took place on the site (i.e., temperature profile similar to ground temperature profile).

Transient ground temperature variation of BH1 is presented in Figure 3-6a. The maximum temperature of 26 °C was observed at 12 m depth at the end of the heating test. Furthermore, temperature reached maximum values at all locations at the end of heating test and therefore no time lag was observed. The temperatures started to decrease as soon as the heating test was stopped. This shows the immediate ground thermal response during and after the heating test.

Figure 3-6b shows the thermal profile of BH1 at selected time periods. The shape of thermal profiles remains the same at all the selected time periods. This indicates uniform ground thermal response to the heat test at all depths. The test has raised the ground temperature in BH1 by 5 °C to 7 °C at every location except at 14 m and 16 m. As noted in section 3.1, the loop was extended to 14.2 m and the ground temperature has increased up to 14 m depth. The lack of temperature change at 14 m and 16 m depths is interesting. It indicates that there is little downward flow of heat from the bottom of the loop. One can conclude from this observation that the heat moved predominantly in a radial direction. The highest temperature increase at the end of the heating test occurred at 12 m depth where the quartz content was the highest in the soil profile (Barry-Macaulay (2013)). Lower temperature increase

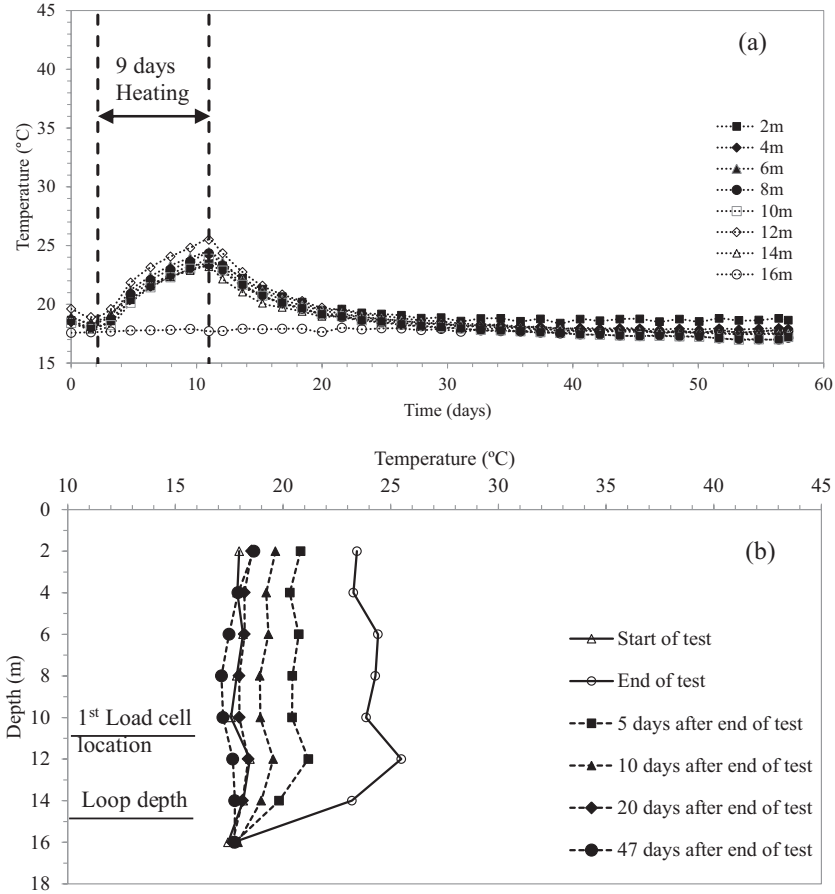

Figure 3-6 Ground temperature response of BH1 to heating test (a) transient temperature (b) temperature profile.

at 2 m and 4 m depths are due to lower air temperature during the test duration. As indicated earlier ground temperature is affected to a large extent by ambient air temperature to the depth of 4 m. The temperature drop is higher five days after cooling compared to ten days cooling. Heat dissipated faster in the beginning after the heating is stopped. The ground temperature returned to its initial value after 20 days cooling. Therefore the ground recovery took twice the time of the heating test duration as observed earlier within the pile. Full thermal recovery based on natural heat dissipation (i.e. return to original ground temperatures prior to any heating tests) took 47 days to complete. It is to be noted

that the ground temperature decreases after 47 days at every location apart from 2 to 4 m depth. This is due to the effect of solar radiation as discussed earlier.

The ground temperature response in BH2 is shown in Figure 3-7a. The temperature does not increase immediately following the start of the heating test. Changes in temperatures started to be observed five days after the heating tests was completed as the heat wave reached BH2. The peak temperature of 19 °C was recorded at 12 m depth.

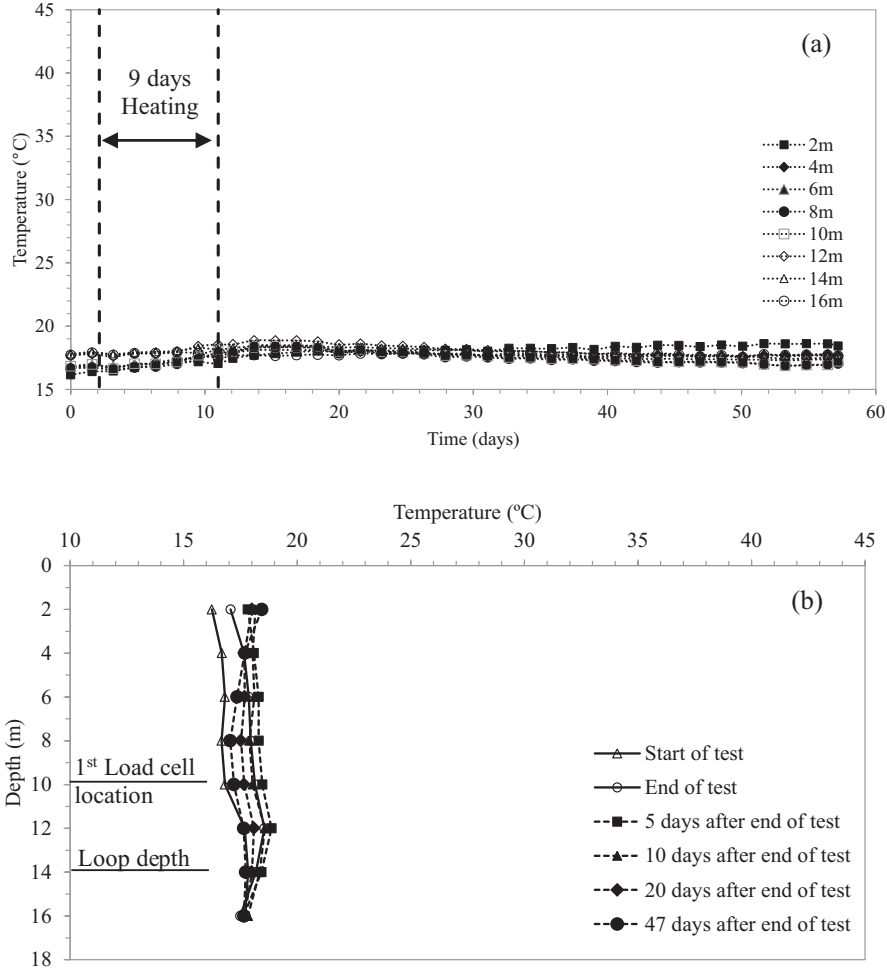

Figure 3-7 Ground temperature response of BH2 to heating test (a) transient temperature (b) temperature profile.

Thermal profile shown in Figure 3-7b presents additional information on the ground thermal response to the heating test and ground thermal recovery. There is little increase in ground temperature during the heating test but as discussed earlier the maximum increase in temperature occurred five days after the completion of the heating test. The ground temperature increased by 1 °C to 2 °C at every depth apart from 16 m. As explained earlier heat moves in radial direction predominantly and the loop length was 14.2 m, which resulted in no temperature change at 16 m depth. The ground temperature started to decrease ten days after the heating test was stopped. The ground thermal recovery in BH2 is slow as temperatures returned to their original values at deeper locations only after 47 days of cooling. The ground temperature near the surface at 2 m and 4 m is affected by solar radiation as the test was performed in summer.

3.5 Mechanical tests

The energy pile was subjected to three separate mechanical load tests on its pile shaft, the first was performed prior to any thermal loading was introduced to the ground, the second was performed immediately following the completion of thermal loading (at the end of the nine day heating period), the third and final test was carried out six weeks after thermal loading was completed, thus following "cooling" of the ground.

Peak Upper O-Cell (UOC) load before and after thermal loading was carried out on the energy pile, the upper section of the pile shaft (10.1 m) was displaced in an upwards direction with the average displacement of the upper pile shaft for the three mechanical pile tests reported in Wang et al. (2015). During loading (pressurising) of the upper O-cell (UOC) the Lower O-Cell (LOC) was "closed" where the middle and lower section of the pile act as one whole section. This allowed the UOC to use the base resistance and the lower 6 m of the pile shaft resistance to react against the upper 10.1 m of the pile shaft resistance.

The field pile test indicated that a peak shaft load of approximately 1750 kN was achieved in normal ground conditions with no application of thermal loading. The peak shaft load for the same upper section of pile was approximately 1900 kN after a thermal load (T approximately 40 °C) was applied to the energy pile for a period of nine days. The peak shaft load of the upper section of pile reduced approximately 1850 kN (see Figure 3-8) after a natural cooling period of six weeks.

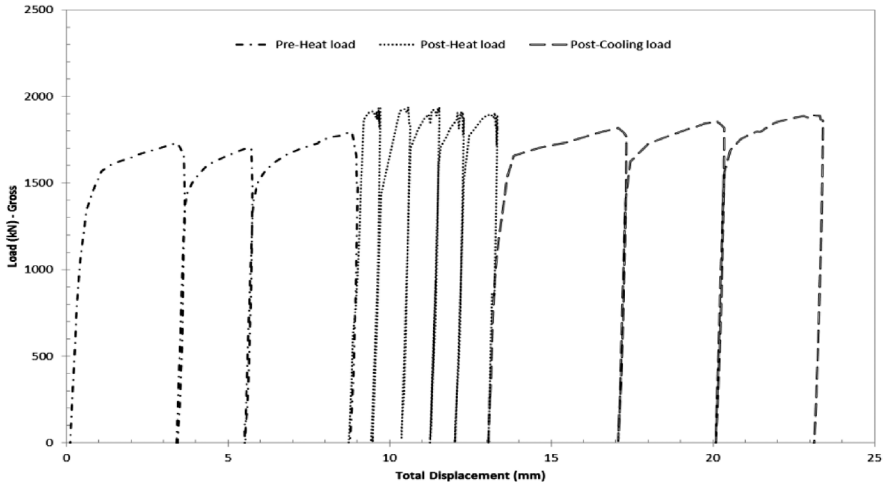

Figure 3-8 Ultimate pile shaft load before and after thermal loading.

The field results indicate that thermal loading did not reduce the peak ultimate shaft resistance of an energy pile founded within a very dense, fine to coarse sand, with no presence of groundwater.

The vertical strains measured at the end of the thermal heating and cooling periods are presented in Figure 3-9. The results show a small variance in vertical strains along the pile depth in the upper-section at

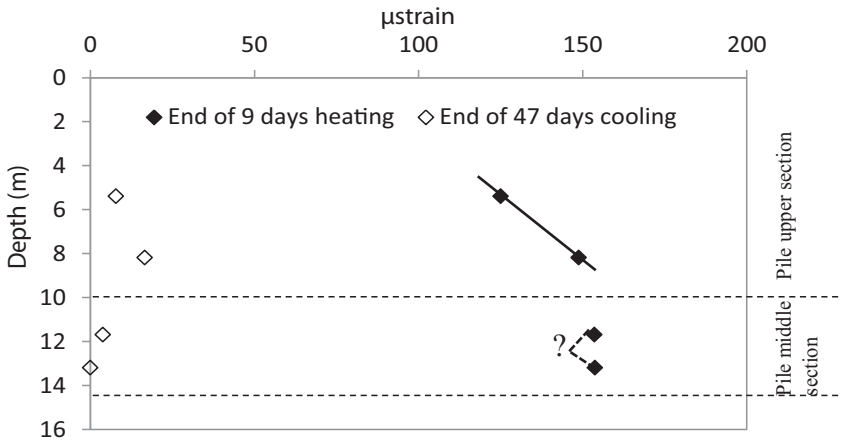

Figure 3-9 Pile vertical thermal strains at end of heating and cooling periods versus pile depth.

the end of the heating periods. However in the pile middle section strains remain constant with depth. Higher vertical strains were observed at pile ends close to the O-cells and lower vertical strain at the mid-depth of the pile upper section, at 5.4 m depth. These observations indicate that pile upper section and middle section act as two separate piles with free ends. Previous studies by Bourne-Webb et al. (2009); Amatya et al. (2012); and McCartney and Murphy (2012) also showed that during the heating period of energy piles with unrestrained ends (or free ends), expansive strains at the mid-depth level would be suppressed to a greater extent than at the ends of the pile shaft. Figure 3-10 presents the change in temperature variation with depth at the end of the heating and cooling tests. The change in temperature remains constant with depth at the end of each heating test. Free expansion strains of 160 micron would have occurred at the end of the nine days heating test if the coefficient of thermal expansion of concrete assumed to be 10 microstrain/°C. Difference between measured and free expansion strains will cause thermal stress in the pile. The thermal stress can be evaluated if modulus of elasticity of pile concrete is known. It is evident that the pile upper section has zero thermal stress at the free end near the O-cell and highest thermal stress at mid height. The pile middle section has zero thermal stress at both free ends near each O-cell but there was no strain gauge installed at the mid height of the middle section, therefore the thermal stresses could not be determined at the mid height.

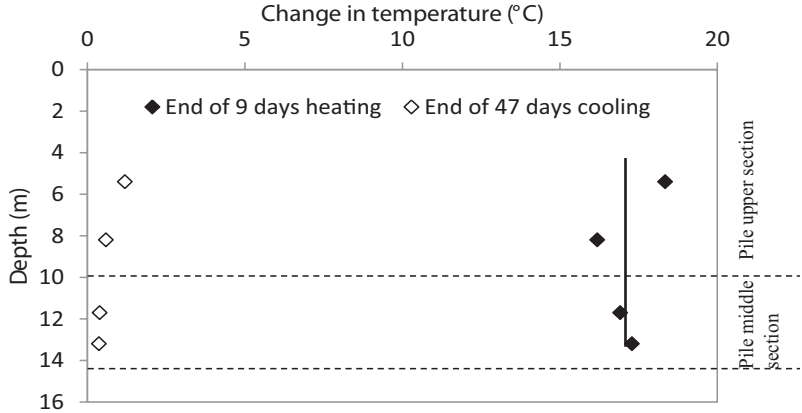

Figure 3-10 Change in pile temperature at end of heating and cooling periods versus pile depth.

At the end of the cooling periods, Figure 3-9 shows that the vertical strains at shallow depths (5.4 m and 8.2 m below ground surface) are slightly higher than strains at deeper depths (11.7 m and 13.2 m below ground surface). This is also due to the ambient temperature influence at shallow depths, where temperatures within the pile at the end of the cooling periods are slightly higher at depth closer to the ground surface than at deeper depths. However, strains are almost fully recovered following the cooling period, which indicates the strains are of elastic nature.

3.6 Dual pile system

The dual pile system was installed in October 2014. The results presented herein refer only for the curing period of the concrete in the piles. Temperature and strain changes were monitored as concrete cured. The average compressive strength of concrete achieved after 33 days of curing was 62.7 MPa.

3.6.1 Concrete curing temperature

The results presented here show depths measured from the top of the pile reinforcement bars. However, after trenching, about 900 mm of the rebars were exposed to the atmosphere. The readings from all the sensors started from day two of concreting. Figure 3-11 shows the concrete temperatures

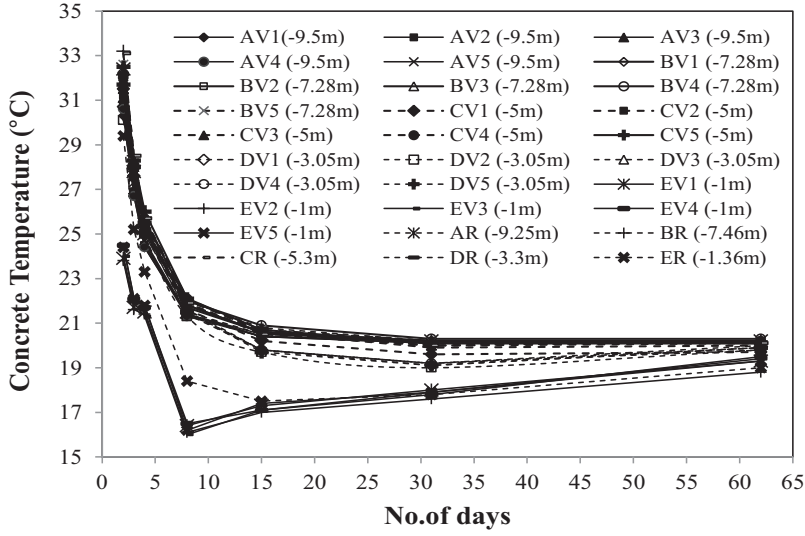

Figure 3-11 Concrete temperatures from all strain gauges against curing time.

with curing time for all vibrating wire strain cum temperature gauges. As the constituents of concrete are mixed, an exothermic reaction occurs, which releases heat, and thus the concrete temperature initially is high (maximum was 33.2 °C on day two). There is a steep reduction in temperature up to day 11, after which the decrease is at a slower rate. The concrete cooled down to approximately 20 °C after 62 days below the depth of 5 m, reaching thermal equilibrium with the ground. Near surface atmospheric effects are felt up to a depth of 3 m, in which case the concrete is much cooler than other locations along the length of the pile.

Figure 3-12 shows temperatures recorded from vertical strain gauges. For any given depth, it can be seen that the concrete temperature reduces with curing time and approaches the undisturbed soil temperature. The temperatures at the centre of pile (V5) are larger compared to the outer gauges for the first few days of concreting. The reason for this is that the outer gauges have lower concrete cover and are closer to the soil compared to the central gauges, thus they lose heat to the soil earlier. It can also be observed that temperatures at all locations approach the

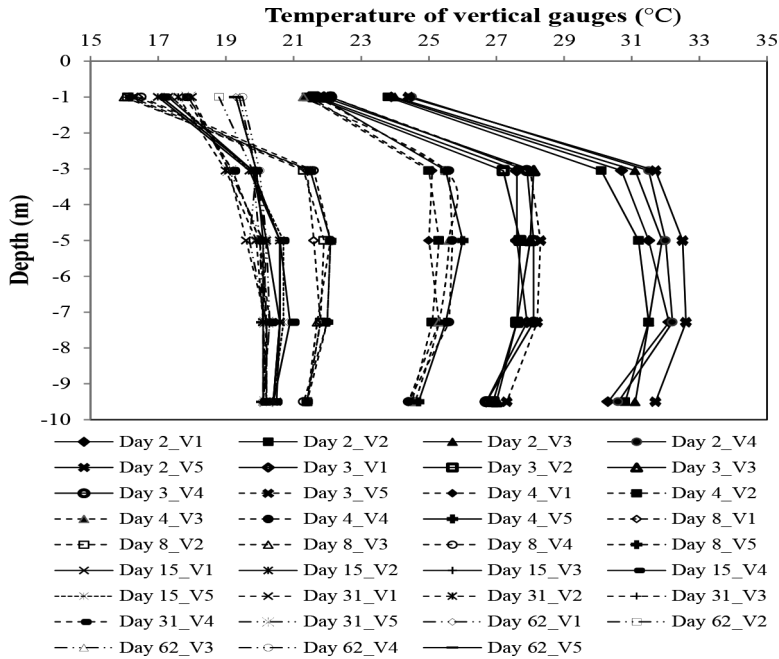

Figure 3-12 Temperatures from vertical strain gauges against pile depth.

same value and slowly move toward thermal equilibrium with the soil. For any given depth, the concrete at the centre of the piles loses heat much slowly to the ground compared to locations closer to the ground. It is observed that temperatures decrease below the 3 m depth and lower temperatures are recorded near the base of the pile. This means that concrete cooled much faster by dissipating more heat to the surrounding soil closer to the bottom of the pile. The pile top, which is exposed to the atmosphere, undergoes rapid cooling for the first few days due to high temperature gradient between concrete hydration temperature and atmospheric temperature, compared to deeper locations.

3.6.2 Strains during concrete curing

Changes in strains were recorded from the vibrating wire strain cum thermal gauges. The changes in strains were corrected with strain and temperature values recorded from all gauges before installation. Negative

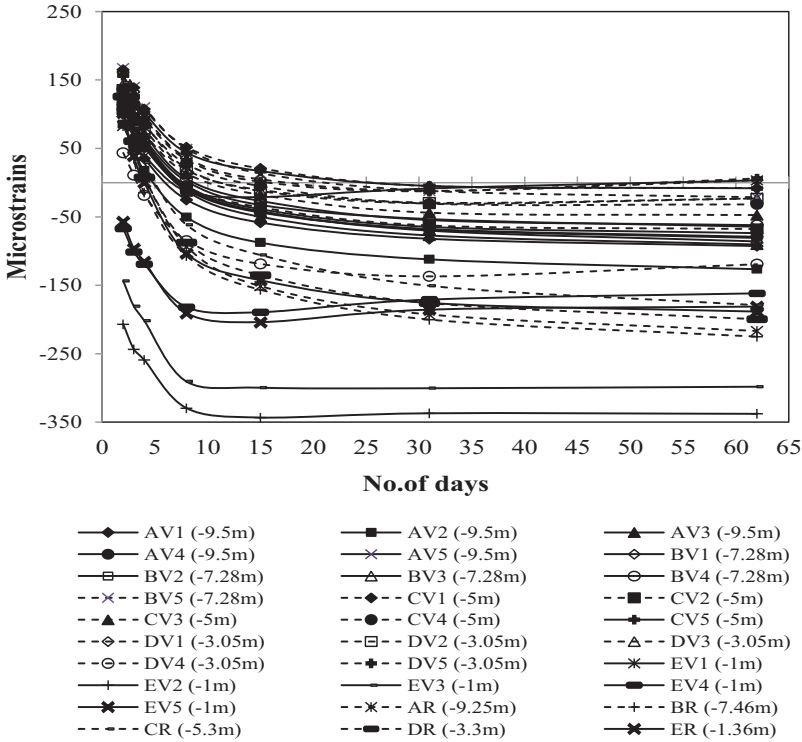

Figure 3-13 Microstrains from all strain gauges with curing time.

strains indicate compression, while positive strains indicate tension. Figure 3-13 shows the change in strains (microstrains) recorded at all the strain gauges versus curing time. It can be seen that the strain trends closely follow the cooling trend of the concrete. The strains were highest in the first few days and then began to stabilize as concrete cured and cooled down. Due to the heat buildup in concrete as a result of hydration, the concrete expands initially and the microstrains are positive indicating tension. As the hydration heat began to dissipate in the ground, the strains began to recover towards compression. The concrete temperature near the ground surface was affected by atmospheric changes, which gave rise to negative strain up to a depth of 3 m for all days.

Figure 3-14 shows vertical strains at two locations, 160 mm concrete cover (V2) and 260 mm (V5) concrete cover. The 260 mm concrete cover strains are the central vertical gauges. These gauges are installed

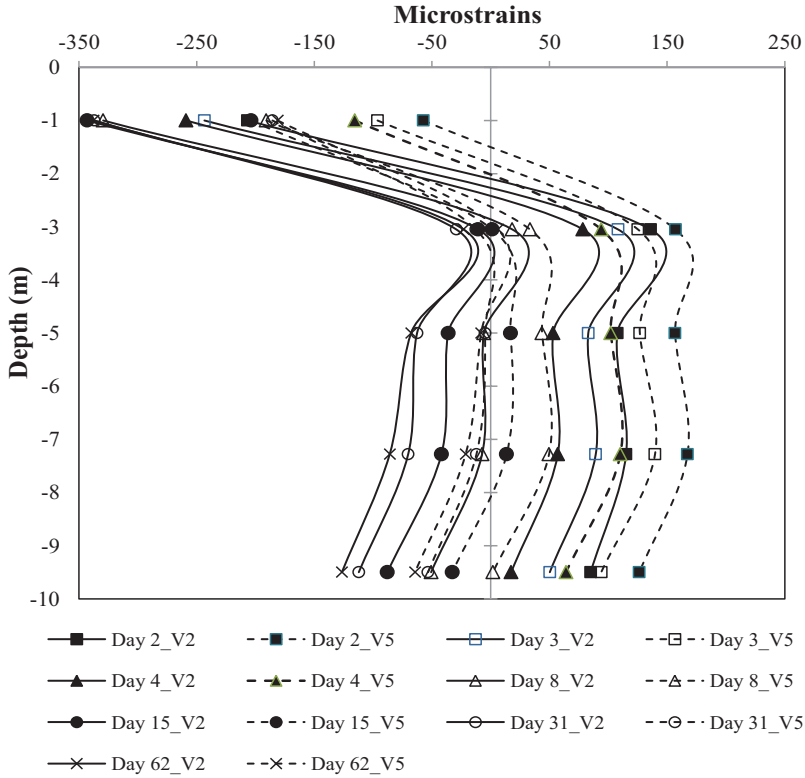

Figure 3-14 Vertical strains at 160 mm (V2) and 260 mm (V5) concrete cover along the depth of the pile.

approximately 40 mm off-center of the pile. It is seen that the strains at higher concrete cover, i.e. at 260 mm, are larger compared to the vertical strains at 160 mm concrete cover. There is a higher heat buildup closer to the center of the pile compared to locations that are closer to the ground, thus giving larger strain values. The gauges at lower concrete cover have lower strains since they cool much earlier than the central gauges. These trends follow the temperature profile of Figure 3-12, showing that higher temperature at larger concrete covers give more strains. The near surface strains have higher compression values due to atmospheric effects (cooling) since the pile top is exposed to the atmosphere. Near surface compression strains are expected to reduce when the ground is covered with concrete as construction of the superstructure continues.

Figures 3-15 and 3-16 shows the microstrains obtained from the radial and vertical gauges placed near the center. There are more compressive

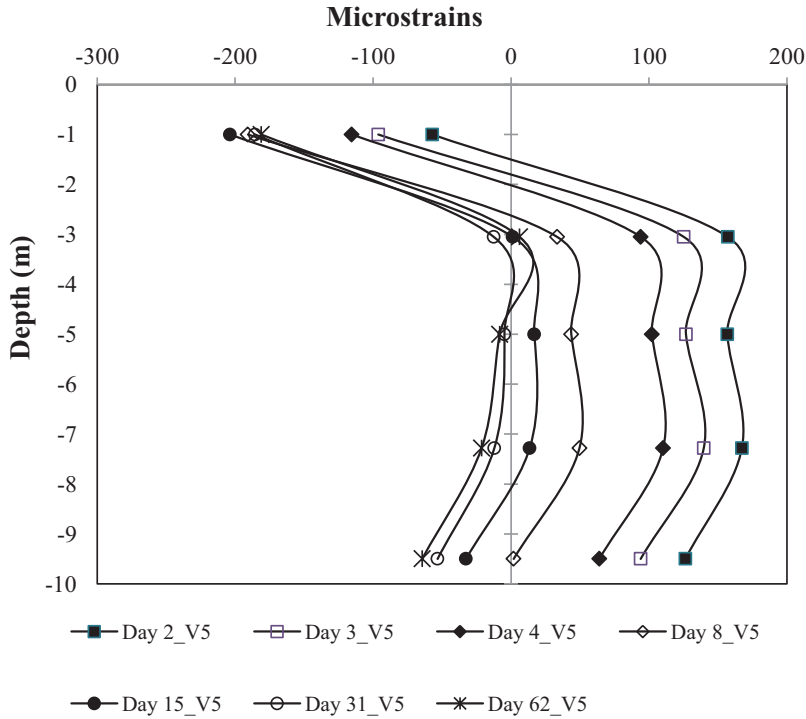

Figure 3-15 Vertical strains at the center of the pile against depth.

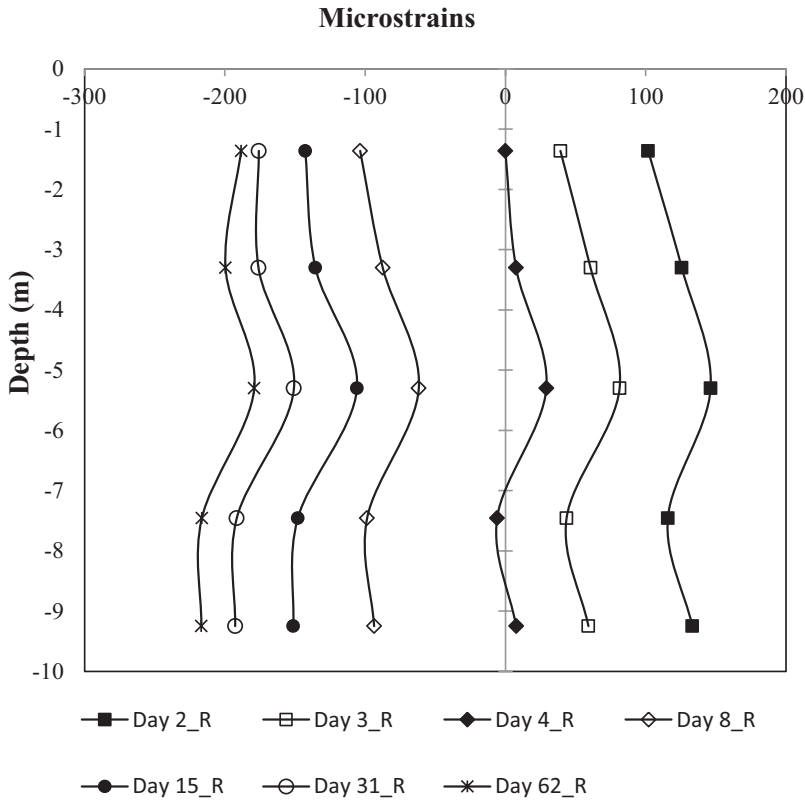

Figure 3-16 Radial strains of concrete against pile depth.

strains (negative strains) in the radial direction compared to vertical strains after 62 days of concrete curing. Compression in radial direction is more since there is more shrinkage in the radial direction as water content reduces with curing, compared to the axial (vertical) length of the pile. Concrete is poured vertically and hence there is more compaction in the axial direction compared to radial direction, thus less shrinkage in vertical direction. The pile top is not restrained vertically and is exposed to the atmosphere. Thus the strains recorded by the vertical gauges are higher in compression due to atmospheric effects compared to the radial strains.

3.7 Conclusions

The field heating test conducted on a single geothermal energy pile embedded in an unsaturated, very dense sand profile indicated that the pile

and the ground required at least more than twice the heating time to thermally recover fully from the heating process without using a cooling process and return to the original temperatures recorded prior to the start of the heating tests. Furthermore the mechanical tests showed that the pile shaft resistance gained strength during thermal heating loads and returned to its initial capacity (i.e. initial conditions) when cooled. This indicated that no losses in pile shaft capacity (i.e. no side friction degradation) were observed after heating and cooling cycles. A variance in average vertical thermal strains was observed along the upper section of the pile shaft at the end of the heating periods. Higher vertical thermal strains were observed at the pile upper section end close to the upper O-cell and lower vertical thermal strain at the mid-depth of the pile upper section. These observations indicate that the pile upper section behaved as a separate pile with free ends. However, the vertical thermal strains remained constant in the pile middle section (also with free ends) at the two depths where the strain gauges were installed (i.e., 11.6 m and 13.2 m, close to the two O-cells).

The recently installed (Oct. 2014) dual pile energy pile system indicates that the concrete is initially in tension due to the cement hydration process but reversed to compressive strains once the concrete cooled down. The concrete temperatures at various depths were also observed to reduce with curing time and slowly moved toward reaching equilibrium with the undisturbed soil temperatures.

3.8 Acknowledgements

The research program on geothermal energy piles was funded by the Victorian Government Sustainability Fund (2009-2012), Vibropile Pty. Ltd., Golder Associates Pty. Ltd., GenesisNow, GeoExchange Australia Pty. Ltd. and supported under the Australian Research Council's Linkage Projects funding scheme (project number LP120200613). Their support is gratefully acknowledged.

3.9 References

Brandl, H., 2006, "Energy Foundations and other Thermo-active Ground Structures," *Géotechnique*, **56(2)**, pp. 81–122.

Adam, D., and Markiewicz, R., 2009, "Energy from Earth-coupled Structures, Foundations, Tunnels and Sewers," *Géotechnique*, **59(3)**, pp. 229–236.

Chandler, K. R., 1992, "Brighton Group - Engineering Properties,

Engineering Geology of Melbourne, W.A. Peck et al., eds., A.A. Balkema Publishers, Netherlands, pp. 197–203.

Wang, B., Bouazza, A., Singh, R.M., Haberfield, C., Barry-Macaulay, D., and Baycan, S., 2015, "Posttemperature Effects on Shaft Capacity of a Full-Scale Geothermal Energy Pile," *Journal of Geotechnical and Geoenvironmental Engineering*, 10.1061/(ASCE)GT.1943-5606.0001266, 04014125.

Barry-Macaulay, D., 2013, "An Investigation on the Thermal and Thermo-mechanical Behaviour of Soils," ME thesis, Monash University, Melbourne, Australia.

Bourne-Webb, P. J., Amatya, B., Soga, K., Amis, T., Davidson, C. and Payne, P., 2009, "Energy Pile Test at Lambeth College, London: Geotechnical and Thermodynamic Aspects of Pile Response to Heat Cycles," *Géotechnique*, **59**(**3**), pp. 237–248.

Amatya, B.L., Soga, K., Bourne-Webb, P.J., Amis, T. and Laloui, L., 2012, "Thermo-mechanical Behaviour of Energy Piles," *Géotechnique*, **62**(**6**), pp. 503–519.

McCartney, J.S. and Murphy, K.D., 2012, "Strain Distributions in Full Scale Energy Foundations', *DFI Journal*, **6**(**2**), pp. 26–38.

About the authors

Author for Chapter 1

Dr. John Scott McCartney is an Associate Professor of Geotechnical Engineering in the Department of Structural Engineering at the University of California San Diego, La Jolla, CA, USA. He obtained a dual B.S.-M.S. degree from the University of Colorado Boulder in 2003 and a Ph.D. degree in Civil Engineering from the University of Texas at Austin in 2007. Dr. McCartney has a broad range of expertise and has published over 150 technical papers on his research. His areas of expertise include unsaturated soil mechanics, geosynthetics engineering, and thermally active geotechnical systems. Dr. McCartney has won awards for teaching and research, including the NSF CAREER award, the Arthur Casagrande Professional Development Award from the American Society of Civil Engineers (ASCE), the James J.R. Croes medal from ASCE, the Young IGS Award from the International Geosynthetics Society, and several best paper awards. He is currently an Editor of the ASCE Journal of Geotechnical and Geoenvironmental Engineering, Editorial Board Member for Geosynthetics International, Geotechnical Testing Journal, Computers and Geotechnics, and Soils and Foundations. He is active on the ASCE GeoInstitute committees on Unsaturated Soil Mechanics and Geoenvironmental Engineering, ASTM International, the North American Geosynthetics Society, and the International Society for Soil Mechanics and Geotechnical Engineering (ISSMGE) Committee TC308 on Energy Geotechnics. Dr. McCartney is a licensed professional engineer in Colorado.

Authors for Chapter 2

Dr. Moncef Krarti, ASME Fellow, Professor and Coordinator, Building Systems Program, Civil, Environmental, and Architectural Engineering Department at the University of Colorado, has been very active in ASME from the last 25 years, especially in the ASME Solar Energy Division (SED). He has served both as Technical and Conference Chairs, and is a past president of SED. Prof. Krarti main research contributions are in areas related to energy efficiency in buildings and renewable energy systems modeling and analysis. He is the co-founder and the co-chair of the ASME Emergency Technologies Committee

on Integrated Sustainable Building Equipment and Systems (ISBES) which initiated several activities including workshops, monographs, and handbooks. Prof. Krarti is considered a world expert in building energy management and has helped establish energy efficiency programs in several countries. Prof. Krarti has published over 250 technical journals in wide of fields related to sustainable energy technologies. He authored three textbooks on building energy management and has been an invited keynote speaker in several national and international forums and conferences.

Byung Chang Kwag is currently a Ph.D. candidate in the Building Systems Program of the Civil, Environmental, and Architectural Engineering Department at the University of Colorado at Boulder. As part of his Ph.D. research work, he has developed three-dimensional numerical models and transfer functions for assessing the thermal performance of thermo-active foundations. He has published several peer-reviewed technical papers on these topics in archival journal and conference proceedings.

Authors for Chapter 3

Dr. Abdelmalek Bouazza is a Professor in Civil Engineering at Monash University, Melbourne, Australia and Adjunct Research Professor at Cardiff University, UK. He is a Fellow of the Institution of Engineers (FIEAust). His research has been recognised by a number of awards including, recently the E.H. Davis Memorial Award from the Australian Geomechanics Society, the 2014 Zeng Guoxi Lecture from Zhejiang University, China and the 2013 International Geosynthetics Society (IGS) Plaque for significant contributions to the International Geosynthetics Society and outstanding technical contributions to the geosynthetics discipline. He is the Chair of the International Soil Mechanics and Geotechnical Engineering (ISSMGE) Technical Committee TC215 on Environmental Geotechnics and Secretary of ISSMGE TC308 on Energy Geotechnics.

Dr. Rao Martand Singh is currently a Lecturer in Geotechncial Engineering at the University of Surrey, UK. Previously, he was a Research Fellow at Monash University, Melbourne, Australia. He obtained his Ph.D. in Geotechnical/Geo-environmental Engineering

from Cardiff University, UK. His research interests are on physical and numerical study of heat, mass and gas flow through deformable unsaturated porous media.

Mr. Mohammed Faizal is a Ph.D. student in Civil Engineering at Monash University, Melbourne, Australia, where he is conducting research on thermal performance of geothermal energy piles. He completed his bachelors and masters degrees in Mechanical Engineering from the University of the South Pacific, Suva, Fiji. His research interests are generally in the areas of geothermal and ocean energy conversion.